Intracranial Hemodynamic Compensation Mechanisms in Patients with Cerebrovascular Disease

By

Jennifer Morgan Watchmaker

Dissertation
Submitted to the Faculty of the
Graduate School of Vanderbilt University
in partial fulfillment of the requirements
for the degree of

DOCTOR OF PHILOSOPHY
in

Chemical and Physical Biology
September 30, 2017
Nashville, Tennessee

Approved:

Manus J. Donahue, Ph.D
Howard S. Kirshner, M.D.
BethAnn M. McLaughlin, Ph.D.
Seth A. Smith, Ph.D.
Edward B. Welch, Ph.D

To my parents, who nurtured my curiosity and are steadfast in their support.

ACKNOWLEDGEMENTS

I would first like to thank Dr. Manus Donahue. I will forever be grateful for your mentorship. Your enthusiasm for new knowledge is inspiring, and I feel so fortunate to have been part of your team. I additionally would like to thank all past and present Donahue lab members and collaborators: Petrice Cogswell, Shelly Crescenzi, Taylor Davis, Carlos Faraco, Matthew Fusco, Melissa Gindville, Lori Jordan, Meher Juttukonda, Howard Kirshner, Katie Lants, Helen Mahany, Kalen Petersen, Swati Rane, Allison Scott, and Spencer Waddle. It has been a privilege to work with each of you. You have been integral to the success of this work, and I can only hope to come across colleagues half as amazing in the future. A special thank you to Dr. Seth Smith. You have been a continuous advocate for me, and your thoughtful consideration of my goals was seminal to my success as a student. I would next like to thank the Vanderbilt Medical Scientist Training Program leadership team. I am additionally grateful to the faculty, staff, and trainees at the Vanderbilt University Institute of Imaging Science. I am privileged to be a part of such a vibrant and well-equipped environment. I would specifically like to thank Zhaoyue Shi, Samantha By, Kristin O'Grady, Vandiver Chaplain, and Zachary Stark; you have all, in your own way, made my time here cheerful. You have all also graciously fielded my questions over the past years (usually programming related, sometimes not). I would additionally like to thank the National Institutes of Health for continuing to provide mechanisms to support biomedical research. My penultimate acknowledgement is to Nancy Hagans. This place could not go on without you, and I will miss our (almost daily) chatter. Finally, I would like to thank my family. Thank you Mom, Dad, Jacqueline, Brittany, Lauren, and Max. I am so lucky to have your unwavering support (and such loving options of people to call when walking to the parking garage late at night).

TABLE OF CONTENTS

Page

LIST OF TABLES

Table Page

LIST OF FIGURES

LIST OF ABBREVIATIONS

a.u.	arbitrary units
ACT	arterial circulation time
ASL	arterial spin labeling
BOLD	blood oxygenation level-dependent
C_a	carrying capacity of oxygen in blood
CBF	cerebral blood flow
CBV	cerebral blood volume
CCA	common caroid artery
$CMRO_2$	cerebral metabolic rate of oxygen consumption
COSS	Carotid Occlusion Surgery Study
CPMG	Carr-Purcell-Meiboom-Gill
CSF	cerebrospinal fluid
CTA	computed tomography angiography
CVD	cerebrovascular disease
CVR	cerebrovascular reactivity/reserve
DSA	digital subtraction angiography
EC/IC	Extracranial to Intracranial
ECA	external carotid artery
EDAMS	encephalo-duro-arterio-myo-synangiosis
EDAS	encephalo-duro-arterio-synangiosis
EMS	encephalo-myo-synangiosis
$EtCO_2$	end tidal carbon dioxide
eTE	effective echo time
FLAIR	FLuid-Attenuated Inversion Recovery
FMD	fibromuscular dysplasia
GM	gray matter
HbO_2	oxyhemoglobin
HZO	herpes zoster ophthalmicus
i.v	intravenous
ICA	internal carotid artery
ISMRM	International Society for Magnetic Resonance in Medicine
MCA	middle cerebral artery
MNI	Montreal Neurological Institute
MRA	magnetic resonance angiography
MRI	magnetic resonance imaging
mSS	modified Suzuki Score
OEF	oxygen extraction fraction

pCASL	psuedocontinuous arterial spin labeling
PET	positron emission tomography
PLD	post-labeling delay
PROM	Phase-based Regional Oxygen Metabolism
qBOLD	quantitative BOLD
QSM	Quantitative Susceptibility Mapping
QUIXOTIC	QUantitative Imaging of eXtraction of Oxygen and Tissue Consumption
RF	radiofrequency
ROI	region-of-interest
s.d	standard deviation
SAMMPRIS	Stenting versus Aggressive Medical Therapy for Intracranial Arterial Stenosis
SCA	sickle cell anemia
SMC	smooth muscle cell
SPECT	single photon emission computed tomography
SSS	superior sagittal sinus
STA	superficial temporal artery
STAR	Signal TArgeting with multiple Radiofrequency
STLCOS	St. Louis Carotid Occlusion Study
TIA	transient ischemic attack
TILT	Transfer Insensitive Labeling Technique
TR	repetition time
TRU-PC	T_2-Relaxation-Under-Phase-Contrast
TRUST	T_2-Relaxation-Under-Spin-Tagging
VISSIT	Vitesse Intracranial Stent Study on Ischemic Therapy
VSEAN	Velocity-Selective Excitation and Arterial Nulling
VWI	vessel wall imaging
VZV	varicella zoster virus
WET	Water Suppression Enhanced through T_1 effects
WM	white matter
Y_a	arterial oxygenation
Y_v	venous oxygenation

CHAPTER 1

INTRODUCTION AND BACKGROUND

Cerebrovascular disease (CVD) encompasses conditions that affect the blood supply to the brain. CVD results in hemodynamic impairment, and when the brain can no longer compensate for decreased oxygen delivery to tissue, stroke results. The development and validation of tools to evaluate parenchymal impairment is important not only for determination of patient-specific disease severity and outcomes following intervention, but also for utilization in clinical trials to stratify patients and determine treatment success. Positron emission tomography (PET) laid the foundation for understanding the hemodynamic and metabolic changes that result from vascular pathology, and which confer significantly elevated stroke risk. In recent years, significant progress has been made toward the evaluation of hemodynamic and metabolic processes in the brain using non-invasive magnetic resonance imaging (MRI) without the use of exogenous contrast agents. Thus, MRI, which is commonly part of standard protocol when evaluating patients with CVD, affords the ability to obtain not only structural information, but also functional information regarding underlying tissue health and operative compensation mechanisms.

Important questions remain regarding the sensitivity of non-invasive methods to detect impairment or improvement, and predict subsequent stroke. The results contained aim to address gaps related to sensitivity of functional MR methods to disease and intervention outcome, as well as extend upon currently available tools for parenchymal assessment by:

1. Evaluating a potential marker of global hemodynamic impairment (oxygen extraction fraction, OEF: ratio of oxygen consumed to oxygen delivered) in CVD compared to healthy controls.
2. Evaluating improvement in cerebrovascular compliance measures following surgical intervention in moyamoya, and comparing these findings to gold-standard digital subtraction angiography.
3. Extending the functionality of an existing MR method for global OEF determination toward hemispheric and regional measurements.

1.1 Stroke and intracranial stenosis

Stroke and public health impact

Stroke affects approximately 795,000 individuals in the United States annually and is the leading cause of serious long-term disability[1-3]. Approximately 185,000 of these strokes (~1 in 4) occur in individuals who have had a prior stroke, and among the survivors more than half over the age of 65 suffer from mobility deficits[3]. Nationally, stroke accounts for an estimated $33 billion dollars of spending, which includes health care services (procedural costs, medication costs, follow-up rehabilitation and care) and missed days of work[3]. Overall mortality following stroke is over 15%, and is highest in the southeastern United States[4]. Looking ahead, a major area of stroke research will likely focus on stratification of patients at highest-risk for stroke event, such that interventions can be titrated and optimized outcomes achieved.

Mechanisms of cerebral ischemia

The three main types of strokes as outlined by the Centers for Disease Control are (i) ischemic stroke, (ii) hemorrhagic stroke, and (iii) transient ischemic attacks (TIA). Ischemic stroke, which is due to insufficient delivery of oxygenated blood to brain parenchyma, accounts for 87% of strokes[4], and hemorrhagic and TIA types account for the remainder of strokes. While TIAs (often referred to as "mini-strokes"), which result from a temporary blockage of blood flow to brain tissue, do not directly result in permanent brain injury, up to 15% of individuals with a TIA have an ischemic stroke within three months[5]. Ischemic strokes can be caused by flow-limiting atherosclerotic plaques in extracranial or intracranial arteries, thrombotic occlusion of a small penetrating artery (lacunar stroke), or be of embolic origin either from a proximal artery (artery-to-artery embolus) or the heart (cardioembolic embolus). More rare etiologies of ischemic stroke include dissection, moyamoya, vasculitis, venous thrombosis, and hypercoagulable states. Notably, 10-40% of ischemic strokes are cryptogenic, with lower rates of cryptogenic strokes reported in specialized centers where extensive diagnostic testing is performed[6-9].

Arteries of the head and neck

Arterial branches from the aorta supply oxygenated blood to the brain via the carotid and vertebral arteries (Figure 1). Cerebrovascular disease can cause stenosis (narrowing) of only cervical arteries, only intracranial arteries, or both. Additionally, emboli from the heart or proximal arteries can travel through the arterial system and result in embolic stroke.

Intracranial stenosis and stroke

Atherosclerotic disease of the intracranial vessels is a significant cause of stroke, accounting for 7-24% of new strokes in America[10, 11]. Worldwide it is estimated that 20 to 40 per 100,000 people suffer an event related to intracranial atherosclerosis, which is the most common form of intracranial stenotic disease[12]. Recurrent stroke in symptomatic patients with intracranial atherosclerosis, despite standard-of-care treatment, is unacceptably high. In recent studies of symptomatic patients treated with gold-standard therapy, between 12.2-15.1% of patients had a stroke at 1-year[13, 14]. Strokes due to non-atherosclerotic intracranial stenosis (i.e. moyamoya, vasculitis, fibromuscular dysplasia) are also an important category of stroke to consider, as stroke prevalence in these populations can be exceedingly high, and treatment plans for these patient groups are less-defined due to lack of clinical trial data[15-18].

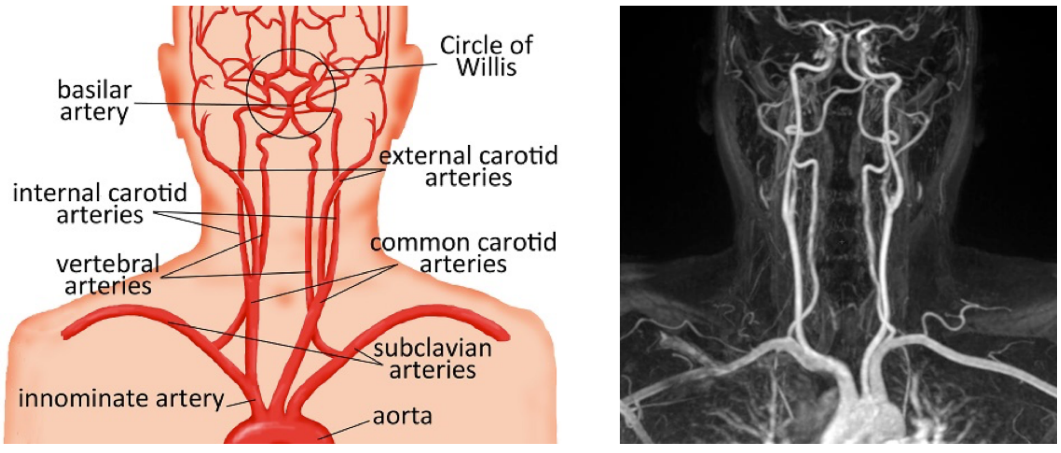

Figure 1. Head and neck arteries. A simplified drawing of arterial anatomy (left) and magnetic resonance angiography (MRA; right) of the head and neck.

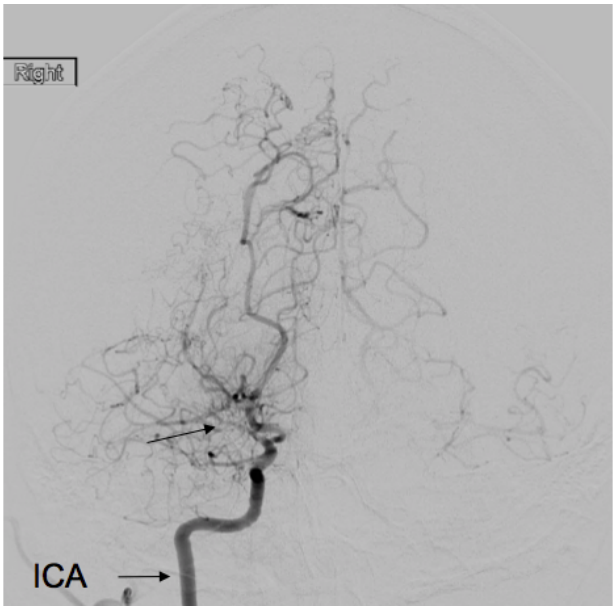

Figure 2. Digital subtraction angiography (DSA) of moyamoya. Injection of intra-arterial contrast into right internal carotid artery (ICA) reveals stenosis of middle cerebral artery, and lenticulostriate collaterals (arrow).

Moyamoya disease (idiopathic) and syndrome (secondary) results in intracranial stenosis due to intimal thickening occurring in the terminal portions of the internal carotid arteries (ICAs)[18,19]. To compensate for arterial stenosis, collaterals form that have a characteristic "puff of smoke" appearance on digital subtraction angiography (DSA; Figure 2); however, the presence of collaterals is not sufficient to protect against stroke. 50-75% of patients with moyamoya disease or syndrome have suffered ischemic stroke or TIA at presentation, while presentation of moyamoya with seizures and headache is less common[20]. One gene (RNF213) has been found to be highly associated with the development of moyamoya disease in Asian populations, although the mechanism is still unknown, and only 9-15% of patients with moyamoya disease report a family history[21]. Moyamoya syndrome occurs secondary to more common conditions including intracranial atherosclerosis, radiation-induced vasculopathy, sickle cell anemia, Down's Syndrome, and neurofibromatosis. Overall, moyamoya disease is the most common cerebrovascular disease of children in Asia (prevalence of ~3/100,000). In Caucasians, the incidence of moyamoya is $1/10^{th}$ as high as Asian populations; however, as secondary causes of moyamoya are

increasing, mainly due to increasing atherosclerosis, and patients with these conditions are living longer, the incidence of moyamoya among Caucasians is anticipated to increase[22].

Distinct from moyamoya, which is not thought to involve an inflammatory component, intracranial stenosis due to vasculitis is characterized by inflammation and sometimes necrosis of the arterial wall[23]. Systemic vasculitis can affect cerebral arteries, in which case a patient typically presents with severe headache, stroke, or encephalopathy. The incidence of cranial vasculitis in Europe is approximately 18/100,000, and is the most common presentation of vasculitis in patients over 50 years old[23]. Vasculitis is often treated with high-dose steroids, and in the case of suspected vasculitis due to viral infection, high-dose anti-viral therapy is administered if the diagnosis is made within the treatment window.

Management and treatment of intracranial stenosis

Management of intracranial stenosis varies depending on etiology. Current standard-of-care for symptomatic intracranial atherosclerosis includes aggressive medical management with dual anti-platelet therapy, in addition to statins and lifestyle modifications. In the recently-halted SAMMPRIS and VISSIT trials[13,14], which concluded that aggressive medical management is superior to endovascular stenting, patients receiving aggressive medical management still had a 12.2-15.1% one-year stroke risk, respectively. In the stenting groups, (Wing-span stent in SAMMPRIS and balloon-expandable stent in VISSIT) the one-year stroke rates were 20-36.2%, respectively. While all patients in both trials had greater than 50% stenosis of one or more intracranial vessels, the differing pathophysiology between patients who suffered a recurrent stroke and those who did not has not been elucidated, yet is fundamental to stratifying these patients for personalized therapies. Surgical revascularization involving direct anastomosis of the superficial temporal artery (STA) with the middle cerebral artery (MCA) has been evaluated in patients with intracranial atherosclerosis. In the Extracranial/Intracranial (EC/IC) Bypass Study, which completed analysis in 1985, it was found that fatal and non-fatal strokes were more common in patients with EC/IC bypass surgery as compared to patients who only received medical management consisting of aspirin therapy and hypertension control[24]. As such, surgical revascularization

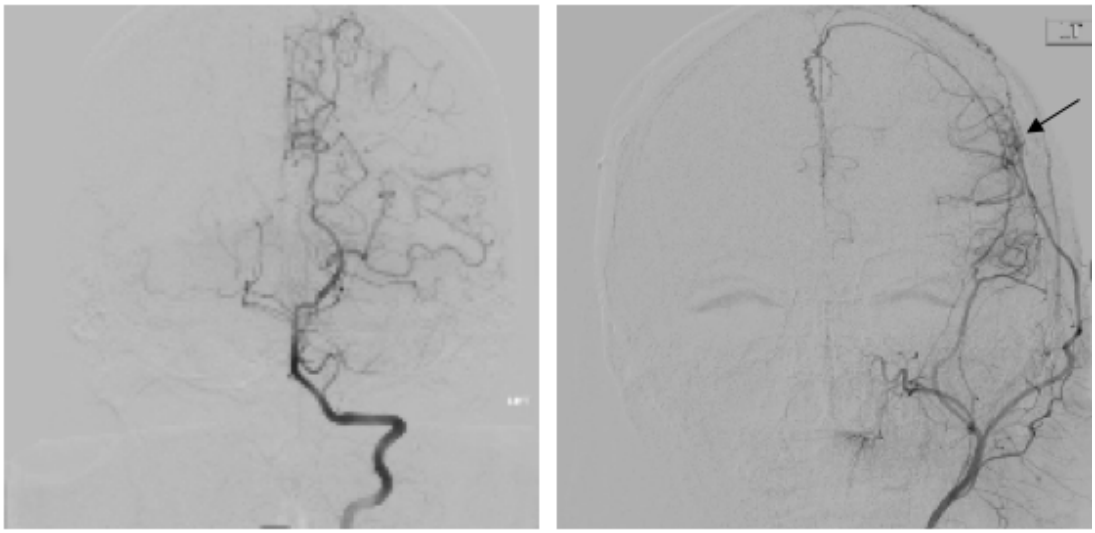

Figure 3. Revascularization in moyamoya. Injection of intra-arterial contrast into the right internal carotid artery reveals stenosis of middle cerebral artery, and lenticulostriate collaterals (left panel). One-year following indirect revascularization, an abundance of collaterals are visualized (right panel; arrow) following contrast injection of the external carotid artery.

is not commonly performed in patients with intracranial atherosclerosis. However, in recent years as surgical approaches have been refined and anti-platelet therapy is now standard-of-care, there is emerging interest in evaluating the performance of improved stents, angioplasty, and revascularization procedures in patients with intracranial atherosclerosis[25, 26].

The mainstay for treatment of symptomatic moyamoya disease and syndrome is surgical revascularization (Figure 3). There is currently no treatment that is known to halt or reverse moyamoya, and therefore treatment focuses on improving cerebral blood flow (CBF; ml blood/100g tissue/minute) using revascularization. While no randomized clinical trials have been performed, there is increasing evidence that revascularization improves outcomes in patients with moyamoya configuration[27-29]. In symptomatic moyamoya patients, either direct revascularization involving the anastomosis of the STA with MCA is performed, or indirect revascularization is performed, which involves the placement of the STA on the brain surface. Depending on vessel caliber, operator experience, and symptomology, combined direct/indirect revascularizations are sometimes performed[30-32].

Overall, better understanding of the pathophysiology of intracranial stenosis will afford better management of these patients. Non-invasive imaging approaches that evaluate parenchymal health, brain compensation mechanisms, and stroke risk in this patient population will aid in the identification of candidate patients for intervention, and help determine response to intervention. Non-invasive tools coupled with innovative treatment options validated in the clinical trial setting will lead to optimized outcomes for patients with different levels of disease severity and stroke risk.

1.2 Brain physiology and compensation mechanisms

Oxygenation and the brain

The brain has a uniquely high demand for oxygen. While only comprising approximately 2-5% of total body mass, the brain consumes over 20% of the oxygen delivered to the body[34]. In order to maintain normal brain function, a constant supply of oxygen and nutrients delivered via the arterial system is necessary, as energy reserves in the brain are limited and do not provide sufficient energy to sustain living cells in the absence of blood flow. Additionally, the brain relies mostly on oxidative metabolism of glucose, with less than 10% of glucose being metabolized non-oxidatively into lactate[35]. Therefore, the brain requires constant oxygen-rich blood delivery in order to maintain metabolic processes. As such, CBF and brain metabolism of oxygen are tightly regulated processes. An increase of blood flow to a region of tissue results from changes in the local environment surrounding the microvasculature. This can occur in response to neuronal stimuli, termed "functional hyperemia", or in disease states, such as anemia, where the delivery of oxygen to tissue per unit blood is decreased[36]. In both healthy and diseased brain tissue, blood flow and volume are regulated in order to maintain a constant supply of oxygen to the tissue, and without this tight regulation, neuronal death occurs. For example, in the setting of hypoxia, CBF is upregulated in order to maintain a constant cerebral metabolic rate of oxygen consumption ($CMRO_2$; ml O_2/100g tissue/minute). Manipulations of the arterial tension of carbon dioxide

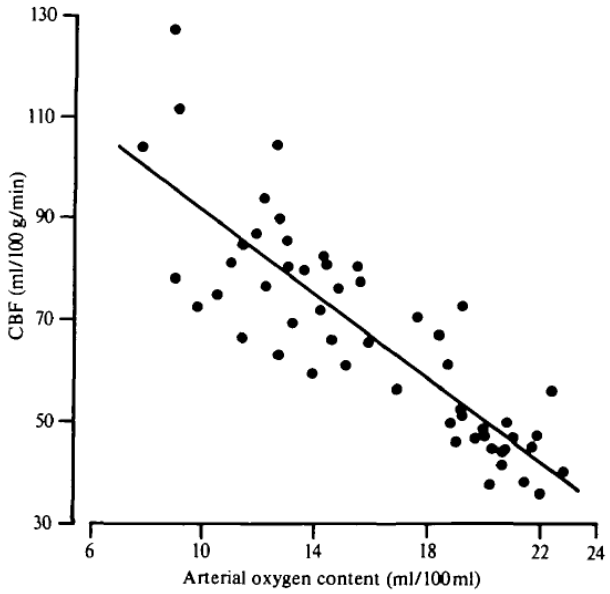

Figure 4. Inverse relationship between CBF and C_a. Participants (n=54) with anemia and polycythemia were included to encompass a large range of carrying capacities of oxygen in the blood. Whole brain CBF was measured using ^{133}Xe-SPECT. Figure from Brown et al., 1985[33].

and oxygen demonstrate that despite large changes in CBF, $CMRO_2$ stays constant, with the exception of anesthesia conditions in which both CBF and $CMRO_2$ decrease[37]. Initially, this relationship was demonstrated by performing experiments in which subjects inhaled low concentrations of nitrous oxide (an inert gas that is able to reach steady state concentration in the blood and diffuse across the blood brain barrier) and measuring concentrations of nitrous oxide in a peripheral artery and jugular vein[38,39]. Subsequently, single-photon emission computed tomography (SPECT), oxygen-15 (^{15}O) PET, and MRI studies, which provide spatial information regarding CBF and $CMRO_2$, have confirmed these findings and will be discussed in subsequent sections. Figure 4 demonstrates the tight coupling of arterial oxygen content and CBF; participants included in this study had a large range of carrying capacity of oxygen in the blood (C_a) due to hematocrit differences attributed to anemia (decreased hematocrit) and polycythemia (increased hematocrit).

Autoregulation in the brain

Cerebral arterioles are lined with smooth muscle cells and contribute significantly to vascular tone by tight regulation of their contraction and relaxation in response to environmental stimuli. The dilation of smooth-muscle lined arterioles in response to changes in cerebral perfusion pressure is termed autoregulation[40-43]. Vasodilation results in an increase in cerebral blood volume (CBV; ml blood/100g tissue), which usually accompanies an increase in CBF. This occurs in order to maintain perfusion pressure in the downstream capillary bed and afford sufficient delivery of oxygen and nutrients to the tissue (Figure 5)[40]. In healthy tissue, the relationship between CBF and CBV is commonly described by a power-law relationship of $CBV \sim CBF^{\alpha}$, where α represents the Grubb coefficient, reported in literature to range from 0.38-0.50[44,45]. In the setting of disease that results in vessel collapse, vessel rigidity, or other microvascular pathology, this relationship may not be accurate.

Autoregulation occurs across a large range of cerebral perfusion pressures in order to upregulate blood flow and volume to regions in need of oxygen and nutrient supply[46]. Outside of this range of cerebral perfusion pressures, perfusion to tissue is linearly dependent on mean arterial pressure[47]. When arterioles are maximally dilated, the autoregulatory capacity is termed "exhausted".

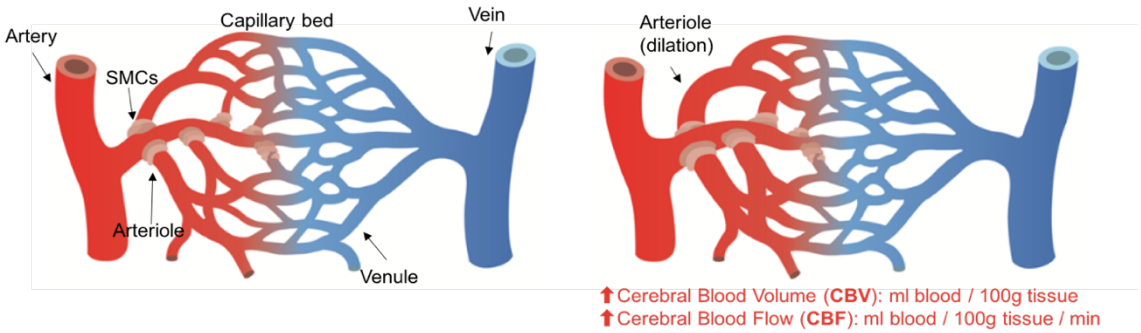

Figure 5. Cerebrovascular reserve. Oxygenated blood flows from the heart to arteries in the periphery. Oxygen, nutrients and waste products are exchanged at the capillary bed, and deoxygenated blood flows out through the venous system. When the cerebral perfusion pressure decreases due to proximal stenosis, smooth muscle cell (SMC) lined arterioles undergo vasodilation, and this is termed autoregulation. This dilation allows for increased cerebral blood volume and cerebral blood flow such that sufficient oxygen and nutrients are delivered to the tissue. Figure adapted from De Vis, 2017[48].

In the setting of proximal stenosis, CBF will decline and the oxygen extraction fraction (OEF; ratio of oxygen consumed to oxygen delivered) will rise in order to maintain a constant $CMRO_2$[49], as described in Equation 1:

$$Oxygen\ extraction\ fraction\ (OEF) \quad = \quad \frac{oxygen\ consumed}{oxygen\ delivered} \quad = \quad \frac{CMRO_2}{CBF \cdot C_a} \quad [1].$$

Oxygen delivered is dependent on the CBF as well as the carrying capacity of oxygen in the blood (C_a). This relationship is governed by the Fick principle, which was originally determined with nitrous oxide uptake experiments, and states that the total amount of a substance consumed by the tissue (in this case oxygen; $CMRO_2$) is equal to the product of the blood flow to the tissue and the arterial-venous concentration difference[43]. This principle has been shown to be true in other organ sites as well. In the setting of anemia, while blood flow may be normal or compensatorily elevated from baseline[50,51], the carrying capacity of oxygen in the blood is decreased.

Figure 6 demonstrates the relationship between hemodynamic parameters in the setting of decreasing cerebral perfusion pressure. When autoregulatory reserve is exhausted, and extraction of oxygen can no longer meet the demands of the tissue, cell death and ischemia occur[52]. If this occurs transiently a TIA will result, but sustained loss of oxygen and nutrients results in ischemic stroke due to hypoperfusion.

Mechanisms of vasodilation

Regulation of smooth muscle cell vasodilation in response to hemodynamic alterations is one way the brain is able to maintain sufficient perfusion even in the setting of severe insults. The molecular pathways involved in this process are relevant, as manipulation of this vasodilatory mechanism is often employed for evaluation of vascular reserve capacity, often termed cerebrovascular reactivity (CVR). Endothelial cells and the smooth muscle cells play an important role in chemoregulation of vascular tone. When blood flow is reduced due to a proximal stenosis, both carbon dioxide and hydrogen ions accumulate in the perivascular space causing a locally decreased pH[53,54]. Preclinical experiments that involved direct

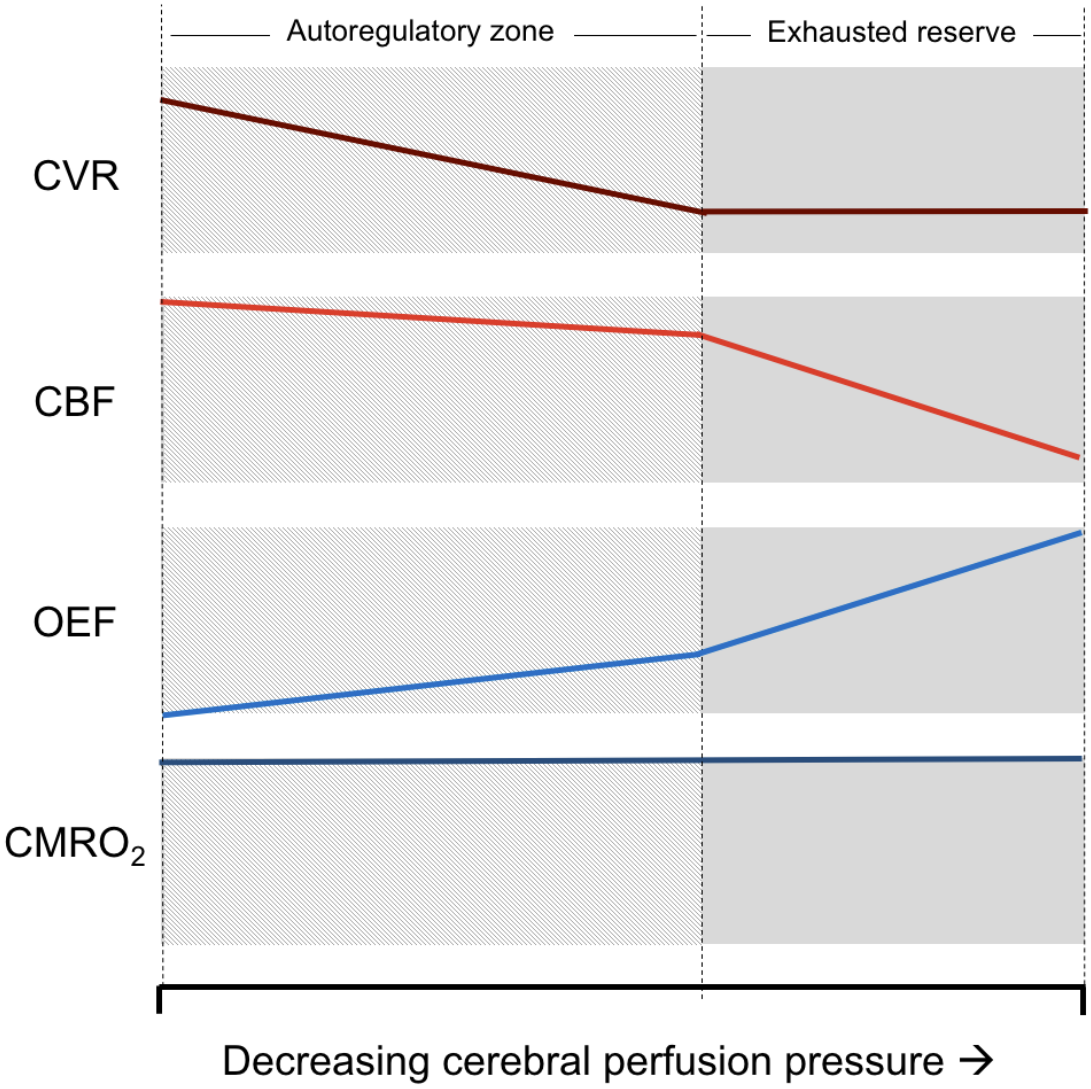

Figure 6. Model of hemodynamic autoregulation. The relationship between cerebrovascular reserve (CVR), cerebral blood flow (CBF), oxygen extraction fraction (OEF), and cerebral metabolic rate of oxygen consumption ($CMRO_2$) are shown. In the autoregulatory zone, cerebral blood volume can increase in order to maintain sufficient cerebral blood flow. As perfusion pressure continues to decrease, OEF which is the ratio of oxygen consumed ($CMRO_2$) to oxygen delivered (dependent on the CBF and carrying capacity of oxygen in the blood) will increase. When vessels are no longer able to dilate to increase flow and CVR is exhausted, CBF decreases as function of cerebral perfusion pressure, and OEF increases significantly. Even when vascular reserve is exhausted, $CMRO_2$ is believed to be unchanged. Figure adapted from Powers et al., 1991[49] and Derdeyn et al., 2002[64].

observation of pial arteries using cranial windows show that lowering of perivascular pH causes vasodilation and conversely elevation of pH causes vascoconstriction[55]. Decreased pH induces activation of endothelium, nerves, and astrocytes which produce vasoactive mediators including prostaglandins, nitrous oxide, endothelium-derived hyperpolarizing factor, and endoethelin-1, which exert their effect on smooth muscle cells[56]. Pharmacologic targeting of vasodilation can be performed for experimental, diagnostic or therapeutic purposes. Acetazolamide (trade name Diamox), a carbonic anhydrase inhibitor, decreases perivascular pH and therefore results in vasodilation and can be administered orally or by intravenous injection. Oral administration has the benefit of not requiring venipuncture, although requires two separate scan sessions, whereas intravenous injection can occur while the participant is in the scanner and does not require multiple scan sessions. Diamox-SPECT, sometimes referred to as "cerebral perfusion SPECT" has been used in the clinical evaluation of reserve capacity in patients with cerebrovascular disease, Alzheimer's, atrophy, suspected brain death, mood disorders, and other conditions, but is currently not clinical standard-of-care at most centers in the United States[57]. Therapeutic use of acetazolamide in the United States is limited, restricted primarily to patients with increased intracranial pressure[58].

1.3 Imaging of cerebral hemodynamics

Imaging cerebral hemodynamics using SPECT, PET, and MRI has greatly enhanced the understanding of cerebral physiology. The relationship between CBF, CBV, $CMRO_2$, vascular reserve and OEF in both health and disease has been explored in depth using ^{15}O-PET tracers. The advancements made by studying absolute and relative changes in hemodynamic parameters in patients using ^{15}O-PET, and its relevance to stroke risk, has motivated much of the development of MRI techniques to measure these parameters non-invasively and without ionizing radiation.

Positron emission tomography (PET)

PET is a nuclear medicine technique that involves the injection of radioactively labeled molecules in order to observe metabolic processes. Clinically, the most commonly used

radioactive tracer is ^{18}F-fluorodeoxyglucose, which can assess tumor burden and glucose metabolism. ^{15}O labels, when incorporated into different molecules, can be used to evaluate oxygen metabolism in the brain.

^{15}O-PET for measurements of hemodynamics and oxygen metabolism

In order to obtain regional measures of CBF[59], CBV[60], $CMRO_2$[61], OEF[62] using ^{15}O-PET, three different tracers are required. All of the tracers used for ^{15}O-PET studies are analogs of naturally occurring molecules, however have a non-radioactive oxygen molecule replaced with a radioactive oxygen molecule (^{15}O). This unstable isotope then decays, emitting positrons, and annihilation events are detectable and localizable using gamma ray detectors with PET scanners. Due to the short half-life of ^{15}O (122 s), an on-site cyclotron is required and an arterial line is required in order to correct for isotope decay. The need for an on-site cyclotron limits ^{15}O-PET studies to specialized centers. Infusion of ^{15}O labeled water ($H_2{}^{15}O$) is used for CBF quantification, ^{15}O labeled carbon monoxide ($C^{15}O$) is used for CBV quantification, and ^{15}O labeled oxygen ($^{15}O_2$) is used to measure OEF, but also requires knowledge of CBF and CBV from $H_2{}^{15}O$ and $C^{15}O$ for inputs to the kinetic model. The product of OEF, CBF and arterial oxygen content is calculated to generate pixel-wise $CMRO_2$ measurements. Table 1 contains a summary of the physiological measurements obtained using each tracer. To evaluate CVR, two scans are required, one at baseline, and one following a vasodilatory stimulus such as acetazolamide[63]; changes in CBF and/or CBV serve as indicators of autoregulation and can be assessed to determine absolute or relative

Measurement	^{15}O tracer	Mechanism	Units
CBF	$H_2{}^{15}O$ (i.v)	Diffuses with blood water	ml blood/100g tissue/min
CBV	$C^{15}O$ (inhaled)	Remains intravascular	ml blood/100g tissue
OEF	$^{15}O_2$ (inhaled)	Metabolized into $H_2{}^{15}O$	unitless
$CMRO_2$	--	--	ml O_2/100g tissue/min

Table 1. ^{15}O positron emission tomography. Hemodynamic and metabolic measurements obtained, their mechanism, and typical units used to describe each. $H_2{}^{15}O$ requires intravenous (i.v) injection.

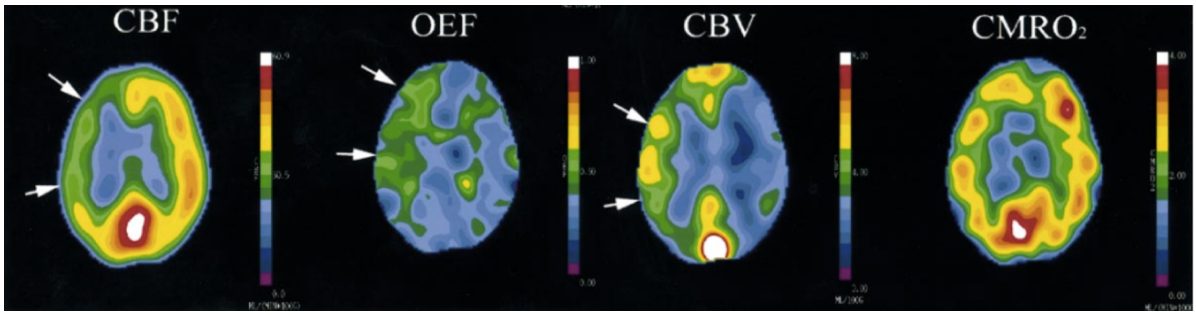

Figure 7. ^{15}O-PET data in steno-occlusive disease. This patient has unilateral carotid stenosis resulting in reductions in cerebral blood flow (CBF). Autoregulation resulted in a unilateral increase in CBV in this patient, and elevated OEF. Symmetric $CMRO_2$ is observed. Figure adapted from Derdeyn et al., 2002[64].

changes in blood flow and blood volume. Figure 7 shows an example of ^{15}O-PET data from a patient with unilateral carotid stenosis due to atherosclerosis. Studies of patients with different degrees of hemodynamic impairment concluded that autoregulation (resulting in increased CBV and CBF) in addition to increased OEF are two compensatory responses to decreased perfusion pressure, but that the reduction of CBV can be highly variable, with some patients demonstrating increased OEF in the absence of increased CBV[64].

^{15}O-PET and clinical use

Despite the technical requirements needed to perform ^{15}O-PET studies, during the late 1990s and early 2000s, many studies evaluating stages of cerebrovascular impairment and impact of intervention were performed using ^{15}O-PET[65-67]. In a study published in 1998 called the St. Louis Carotid Occlusion Study (STLCOS), it was found that in a cohort of 81 patients with unilateral carotid occlusion, that hemispherically-elevated OEF as measured by PET is an independent risk factor for subsequent stroke (Odds-ratio: 6.87; average time to follow-up = 31.5 months) on multi-variate analysis[68]. The hemispheric cut-off for determination of elevated OEF was >1.082, which was determined based on a control participant cohort. Other variables entered into the multivariate model included age, prior infarct, hemoglobin, time since most recent symptom, and triglycerides. Kaplan-Meir analysis of this study with event defined as stroke in the ipsilateral hemisphere to stenosis is summarized in Figure 8.

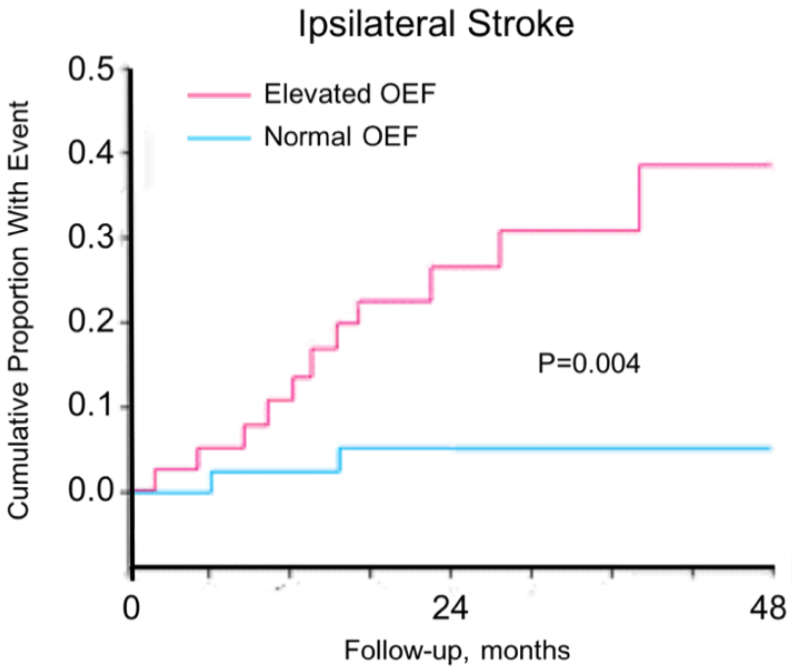

Figure 8. Elevated OEF and stroke occurrence. Kaplan-Meir curve for the end point of ipsilateral stroke. Figure from Grubb et al., 1998[68].

Additional studies corroborated elevated OEF as a strong predictor of subsequent stroke. For example, a study by Yamauchi et al., which included patients with symptomatic ICA or MCA steno-occlusion, reported a 5-year stroke rate of 71% in patients with elevated OEF (defined as OEF >53.3%), compared to 18% in patients with normal OEF[65]. This quantitative OEF cut-off was based on healthy control subject data, in which OEF was 42.6% ±5.1%. The study by Yamauchi et al. also evaluated hemispheric ratios of OEF, and found this to be an inferior measure of stroke risk compared to absolute quantification, and moreover, that hemispheric ratios of OEF identified different patients as having elevated OEF.

Results of STLCOS, in addition to multiple reports of hemodynamic improvement, specifically decreased OEF, following surgical revascularization in small-scale studies of patients with carotid stenosis[69-71], prompted the evaluation of revascularization surgery in a randomized controlled trial setting. The Carotid Occlusion Surgery Study (COSS) was performed to determine if direct STA to MCA surgical revascularization of patients with carotid artery disease and elevated OEF would reduce ipsilateral stroke at two years when

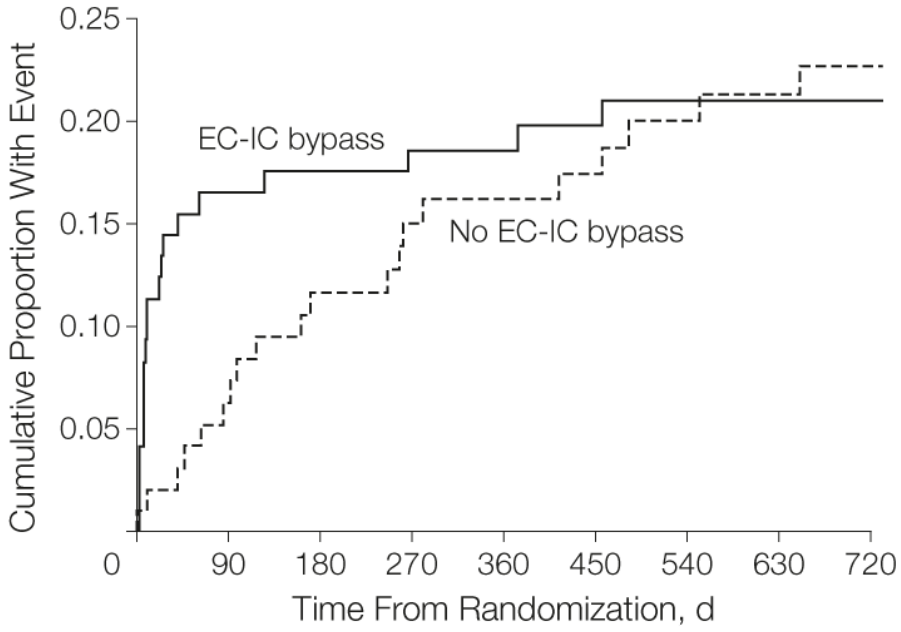

Figure 9. COSS trial. Kaplan-Meier curves for stroke events in surgical bypass and non-surgical groups as a function of time from randomization in days (d). This study enrolled patients with elevated OEF and unilateral carotid stenosis between 2002 and 2010. Figure from Powers et al., 2011[73].

compared to medical management alone[73]. In this study, a hemispheric ratio 1.130 distal to carotid occlusion was required (when compared to contralateral MCA territory). Absolute quantitation of OEF was only able to be performed on a subgroup of patients due to technical limitations including inability to obtain an arterial line and serial arterial sampling during the course of the study. On repeat PET scan to evaluate change in OEF in the patients randomized to surgery, the mean ratio improved from 1.258 at baseline to 1.109 at the post-operative PET scan performed 30-60 days following surgery. Despite improvements in hemodynamics and 98% graft patency in the surgery group, at 30 days, the ipsilateral stroke rate in the surgical group was 14% compared to 2% in the medical management group.

Due to the large number of peri-operative events, it was determined that based on the defined study end-point (either new stroke event or two years following intervention) that there was no added benefit of surgery. These results are shown in Figure 9. There is however controversy over the use of hemispheric ratios instead of absolute quantitation of OEF values[72]. While direct STA-MCA anastomosis is not standard-of-care for patients with

symptomatic carotid disease based on this trial, it is important to recognize that the decrease in OEF following surgery was greater than 10% indicating that changes in OEF were correlated with improved hemodynamics in this patient group. It should also be noted that due to the involved protocol required to perform ^{15}O-PET studies, sample sizes in both the STLCOS and COSS trials are limited. In the COSS study, 491 patients were referred to the study, but only 81 ultimately consented to participate.

Overall, evaluation of cerebrovascular dynamics using ^{15}O has been vital to understanding operative mechanisms in cerebrovascular disease and compensation in the setting of decreased perfusion pressure[67]. While ^{15}O-PET is not used clinically for evaluation of cerebrovascular disease, the use of ^{15}O-PET derived measures such as OEF, in which elevations have strong predictive power of subsequent stoke, was important due to its use as a biomarker of stroke risk in clinical trial settings. Looking forward, the use of less-invasive and non-invasive methods for determination of parenchymal function and disease may serve as important tools for evaluation of therapy success, severity of disease, and longitudinal evaluation of disease progression and prognosis in validated settings.

Magnetic resonance imaging (MRI)

The non-invasive nature of MRI makes it an attractive tool for evaluation of not only brain structure, but also brain function. The development of higher-field magnets coupled with the advent of sequences that evaluate hemodynamics, have afforded further understanding of cerebrovascular disease. In this section, I will focus on MRI methods that quantitatively evaluate CBF, and OEF. Additionally, I will discuss traditional and more novel methods used to assess cerebrovascular compliance, and delays in vascular reactivity. Most MRI methods for measuring cerebral hemodynamics and metabolism have not been compared directly with ^{15}O-PET due to technical limitations. While reported ranges for hemodynamic measurements generally agree between modalities, fundamental differences exist between the mechanism of contrast between the modalities, make it such that normative ranges of parameters are not always directly comparable. Table 2 provides a concise list of common MRI methods used to evaluate brain hemodynamics and metabolism.

Measurement (units)	Method	Contrast mechanism	Normative Values	References
CBF (ml blood /100g tissue/min)	Pseudo-continuous arterial spin labeling (pCASL)	Magnetically labeled arterial blood that exchanges with tissue water and attenuates signal in M_z.	Gray Matter: 40–60 ml/100g/min	Grubb et al., 1974[74]; Petersen et al., 2010[76]; Zheng et al., 2014[86]
			White Matter:16-30 ml/100g/min	Grubb et al., 1974[74]; van Osch et al., 2009[77]; Wu et al., 2013[85]
OEF (unitless)	T_2-relaxation-under-spin tagging (TRUST)	Deoxyhemoglobin in the superior sagittal sinus that results in T_2 decay.	0.30 - 0.40	Qin et al., 2011[78], Lu et al., 2011[79]
CBV (ml blood / ml tissue)	Inflow-based vascular space occupancy (iVASO)	Nulling of blood water resulting in extravascular water signal only, which is proportional to intravascular volume.	Gray Matter: 4.7–5.5 ml/ml tissue	Hua et al., 2011[83]; Donahue et al., 2009[80]; Grubb et al., 1974[74], 1978[75];
			White Matter: 1.9–2.8 ml/ml tissue	Grubb et al., 1974[74], 1978[75]
$CMRO_2$ (ml oxygen/100g tissue/min)	Calculated from OEF and CBF based on Fick Principle; uptake = blood flow x arteriovenous differences	---	2 – 4 ml oxygen/100g/min	Lu et al., 2011[79]; Powers et al., 1985[81]
CVR-weighted (Z-statistic)	Hypercapnic blood oxygenation level-dependent (BOLD) MRI	Proportional increase in deoxyhemoglobin in venules and veins that induce dephasing of spins, and decreased T_2 or T_2*.	Semi-quantitative	Spano et al., 2013[82]; Donahue et al., 2014[84].

Table 2. MRI methods for measuring cerebrovascular physiology.

Measurement of cerebral blood flow with arterial spin labeling (ASL)

CBF is a tissue-level measurement of the amount of blood delivered to an area per unit time, and is frequently measured in units of ml blood/100g tissue/min. Contrast based methods rely on the measurement of signal loss as a gadolinium bolus travels through the capillary bed. This method is termed Dynamic-Susceptibility-Contrast MRI. In this approach, a kinetic model is used to relate signal loss to blood blow, blood volume, and meant transit time. Arterial spin labeling does not require exogenous contrast, and employs the magnetic labeling of blood-water applied outside of the imaging volume. Due to considerations of blood-water labeling efficiency and compatibility with clinical coil transmission hardware, the specific type of blood-water labeling recommended for clinical use by the International Society of Magnetic Resonance in Medicine (ISMRM) Perfusion Study Group is pseudo-continuous arterial spin labeling (pCASL)[87]. Continuous ASL approaches, which transmit a continuous radiofrequency (RF) pulse, are not compatible with most clinical scanners, and require additional hardware.

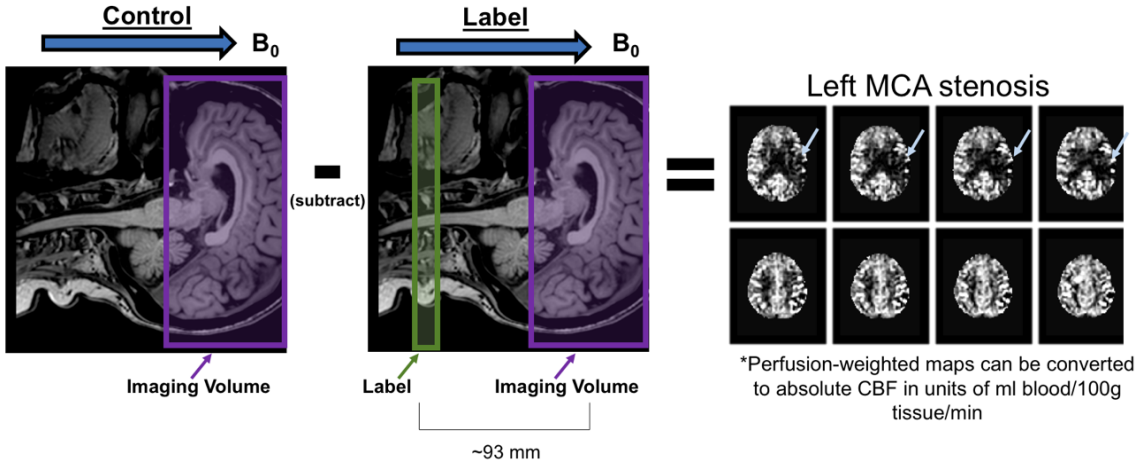

Figure 10. Pseudo-continuous arterial spin labeling. Magnetic labeling of blood-water is applied outside the imaging volume. The labeled blood-water then flows into the imaging volume and attenuates tissue signal after exchange in the capillaries with tissue water. Subtraction of a magnetically labeled image from an image with no blood-water labeling yields signal from cerebral blood flow only. In this example, decreased signal in the left middle cerebral artery (MCA) is observed as a result of left-sided intracranial stenosis (blue arrow).

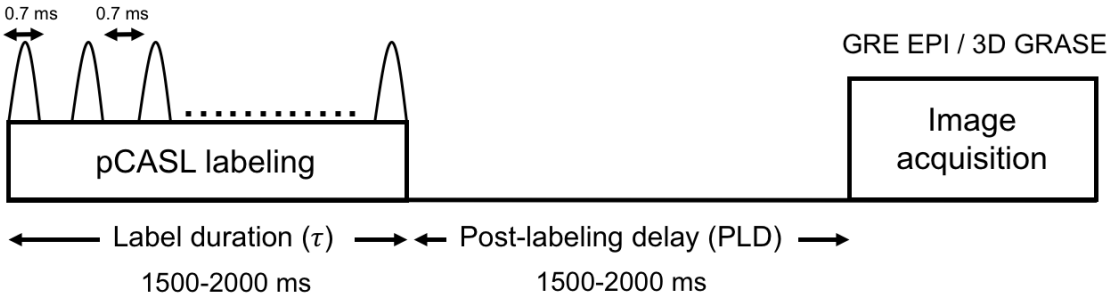

Figure 11. Timing diagram of pCASL.

In pCASL, a 1500-2000 ms train of RF pulses, which invert inflowing spins ($+M_z$ to $-M_z$) through principles of flow-driven adiabatic inversion, are applied to the labeling plane at a frequency of 1/millisecond[88]. The labeled blood-water then flows into the imaging volume and attenuates tissue signal after capillary exchange with the unlabeled blood pool in tissue. By obtaining images also without labeled blood-water, known as 'control' images, and voxel-wise subtracting the label images from the control images, signal attributed only to CBF can be isolated. Figure 10 shows a schematic of the placement of label and imaging volumes in pCASL.

The signal recovery of labeled blood is governed by the T_1 of arterial blood (1650ms in healthy adults at 3 Tesla (T)[89]). Therefore, the time between blood labeling and imaging volume acquisition, known as the post-labeling delay (PLD), needs to be short enough for sufficient label to be present, but also long enough for the bolus of labeled blood-water to be delivered to the capillary bed. A diagram of pulse timings for pCASL, and recommended values for use in healthy adults less than 70 years old is shown in Figure 11. Importantly, in settings of either increased or decreased blood arrival times to tissue, different PLDs are often used. A notable example of delayed blood arrival times to tissue is in the setting of collateral networks, such as in moyamoya, and other conditions of chronic hypoperfusion. The PLD however cannot be so long such that there is no signal present (>>1650ms). Often in patients where there are areas of significantly delayed blood arrival time, hyperintense artifacts occur due to intravascular labeled blood that has not yet mixed with tissue blood at the time of image acquisition[90].

Different models have been proposed and utilized to determine absolute blood flow measurements from perfusion-weighted signal maps obtained from ASL. These models are based on flow-modified Bloch equations that account for inflow of inverted spins due to magnetic labeling of blood along the z-direction The single compartment model assumes rapid exchange of labeled blood-water at the capillary bed, that there is no outflow of labeled blood-water from the voxel due to the unlabeled tissue water pool being much larger than that the labeled blood pool, and that relaxation of the labeled spins is governed by only the T_1 of blood (~1650 ms at 3T[91]). Therefore, when using a one-compartment model, there is no reference to the T_1 of tissue (700-1100 ms), which is slightly shorter than the T_1 of blood. A two-compartment model for CBF quantification includes a pre-capillary arterial compartment within the voxel, in addition to the tissue compartment where mixing occurs[92].

A simplified one-compartment model was proposed in 2014 by the ISMRM Perfusion Study Group, with the goal of providing a standardized method for ASL data processing that does not require the additional information often required by more complex models. The simplified equation is comprised of the following terms: blood brain barrier partition coefficient (λ; 0.9 ml/g[93]), subtracted signal intensities (ΔM), a proton density weighted image for signal normalization (M_0), T_1 of blood (1650ms at 3T[89]), PLD, label duration (τ), and labeling efficiency (α). The labeling efficiency corresponds to the degree of inversion of labeled spins and depends on ASL implementation, and blood flow velocity in labeling plane[94]. Generally a labeling efficiency of 0.85 is used for pCASL. Voxel-wise CBF can be then calculated by Equation 2:

$$Cerebral\ blood\ flow\ (CBF) = \frac{6000 \cdot \lambda \cdot \Delta M \cdot e^{PLD/T_{1,blood}}}{2 \cdot \alpha \cdot T_{1,blood} * M_0 \cdot (1 - e^{-\tau/T_{1,blood}})}\ \text{ml/100g/min} \qquad [2].$$

The factor of 6000 coverts the units from ml blood/g/s to ml blood/100g tissue/ minute. When a two dimensional acquisition is used, the PLD is slice time corrected to take into account the delay between acquired slices.

Cerebrovascular reactivity using blood oxygenation level-dependent (BOLD) imaging

The hemodynamic response to a neuronal or vascular stimuli can be measured by BOLD imaging, which is sensitive to the relative amount of paramagnetic deoxyhemoglobin in the post-capillary venous system. I will focus on the BOLD response to vascular stimuli, which can evaluate the vascular reserve (autoregulatory) capacity in the brain.

BOLD contrast was first described by Ogawa et al., in 1990 in a preclinical model in which an elevated level of carbon dioxide was administered[95]. Hypercarbia results in smooth-muscle lined arteriolar dilation and therefore upregulation of CBF. An increase in blood flow results in more oxyhemoglobin delivery to the brain parenchyma, which results in proportionally less paramagnetic deoxyhemoglobin in the venous system, as metabolic demand of the tissue ($CMRO_2$) does not increase. Even in the setting of strong neuronal stimuli, increase in CBF and delivery of oxyhemoglobin greatly exceeds any increase in oxygen metabolism in the tissue, thus making functional evaluation of activated brain regions also able to be evaluated using BOLD imaging. Specifically, decreased paramagnetic deoxyhemoglobin results in less dephasing of proton-spins, therefore a larger signal intensity

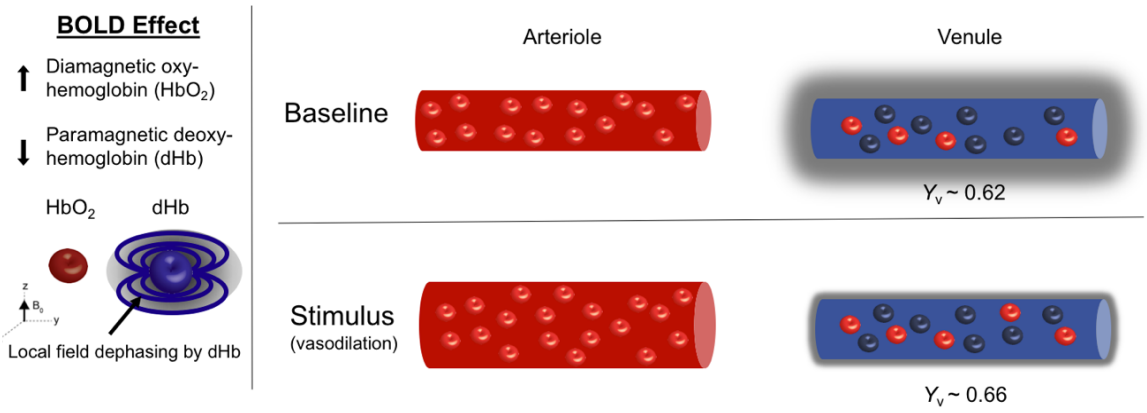

Figure 12. Physiological basis of BOLD. At baseline, venous oxygenation is approximately 62%, but in conditions of induced vasodilation and resultant increased cerebral blood flow, venous oxygenation increases. This proportional decrease in amount of paramagnetic deoxyhemoglobin results in the BOLD effect, which results from increased signal due to less dephasing of water spins in and around capillaries and veins.

(BOLD effect) when evaluated by MR using T_2 or T_2^*-weighted imaging which is sensitive to magnetic field dephasing. The increase in signal intensity on T_2 or T_2^*-weighted imaging results from less proton dephasing of protons in blood-water which is in the vascular system and brain tissue. Figure 12 shows an example of the effect of vasodilation on local field dephasing and venous oxygenation (Y_v).

Vascular reserve capacity can be assessed by BOLD imaging using a stimulus that results in elevated content of carbon dioxide in the blood (e.g. breath hold, acetazolamide, or mild hypercapnia delivered through nasal cannula or face mask). In the setting of decreased, or absent, vascular reserve capacity, where arterioles are near or at maximal

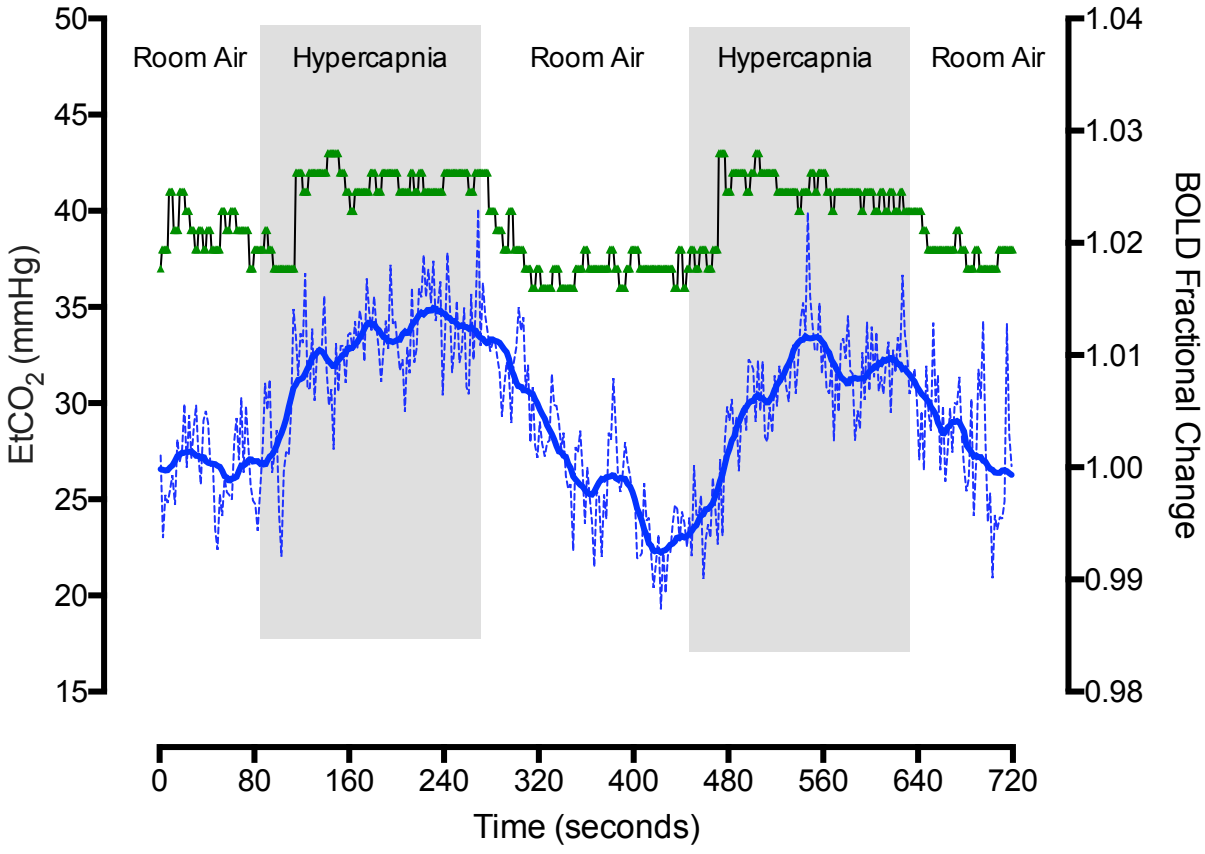

Figure 13. Hypercapnia BOLD time-series. BOLD signal change increases above baseline upon administration of hypercapnia. Signal is normalized by baseline (room-air) intensity values.

dilation, the BOLD effect will be small due to the limited ability to upregulate blood flow further in the presence of a vascular stimulus.

Figure 13 shows an example of a BOLD time series obtained from a participant undergoing a protocol consisting of two blocks of hypercapnia interleaved with air. The end -tidal carbon dioxide ($EtCO_2$) elevates quickly upon stimulus administration and then plateaus. The BOLD signal takes longer to increase due to the time it takes for the smooth muscle cells to respond to upregulation of vasodilatory mediators induced by elevated carbon dioxide and subsequently decreased perivascular pH. The BOLD signal is normalized by baseline magnitude values and fractional change in the BOLD signal is therefore plotted.

Ultimately, a voxel-wise analysis is performed on the BOLD time–series using the gas paradigm as a regressor function. The correlation between the paradigm and signal time-series at each voxel is determined, resulting in a parameter estimate image, with higher values indicating stronger correlation with stimulus paradigm. This value is then normalized by the standard error, which is dependent on the standard deviation of the signal at the voxel over time and number of measurements. T-statistics can then be converted to z-statistic values. Equation 3 describes the z-statistic (also referred to as z-score) measure with X equal to the average of the signal during the stimulus in each voxel, μ referring to the average signal during the stimulus at all voxels (population average), and σ corresponding to the standard deviation of the signal over time:

$$z - statistic = \frac{X - \mu}{\sigma} \qquad [3].$$

An alternative approach for analyzing BOLD data is to evaluate relative signal change ($\Delta S/S_0$) by dividing the mean signal change between the stimulus and baseline block (ΔS) from the mean signal during the baseline periods (S_0). Ideally this method would take mean values when the signal is stable (e.g. towards the end of the stimulus or baseline block). Unlike z-statistic measures, this method does not take into account the contribution of noise. Additionally, subject specific determination of which baseline and stimulus periods of time to include in the mean value measurement may be necessary if delays in the BOLD response

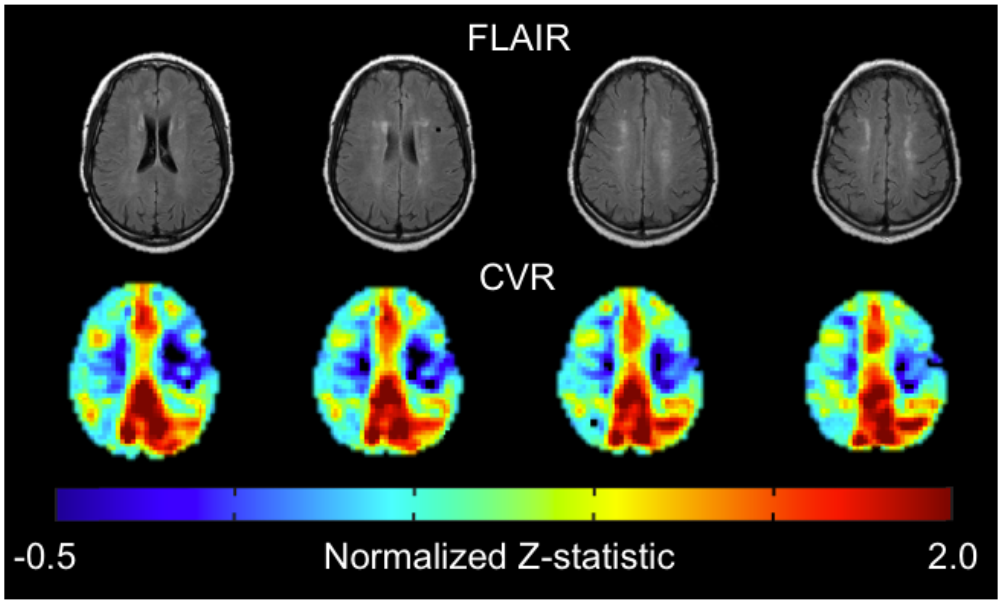

Figure 14. FLAIR and BOLD examples in moyamoya. On the top panel, structural imaging shows bilateral chronic infarcts. BOLD imaging shows bilaterally decreased cerebrovascular reactivity (CVR). Posterior CVR is preserved, consistent with moyamoya disease affecting anterior, but not posterior, circulation. This patient went on to have bilateral revascularizations. The z-statistic values are normalized to whole brain CVR.

are observed or if there is a limited period of stable signal during stimulus or baseline periods. As such, z-statistic measures are most commonly used when evaluating BOLD data, however a strong correlation is expected between relative signal change and z-statistic measures. Figure 14 shows axial slices of structural FLuid-Attenuated Inversion Recovery (FLAIR) and BOLD imaging in a patient with bilateral moyamoya. In this example, higher z-statistic values are seen in the posterior circulation when compared to anterior circulation. Cortical decreases in CVR are seen bilaterally, with more severe disease on the left. This patient later had bilateral revascularizations, with the left performed first.

Time-delay processing of BOLD

Vascular disruption has been shown to cause significant delays as well as attenuation of the hyperemic response in preclinical models of endothelial injury[96]. When determining z-

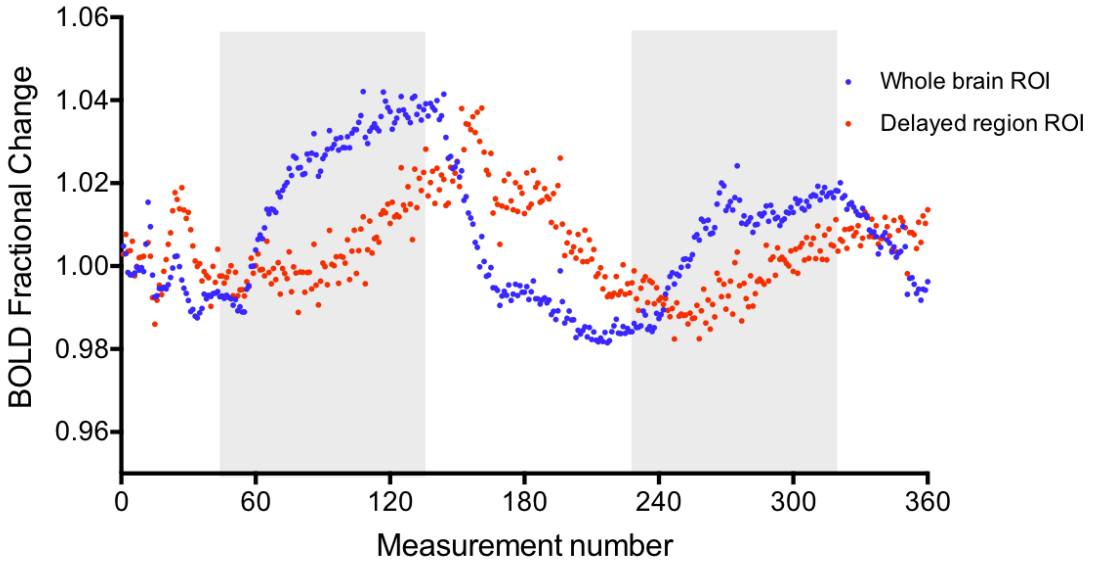

Figure 15. Time-delay of BOLD signal. The blue points represent average BOLD fractional signal change using an entire brain region-of-interest (ROI). The red points represent average BOLD fractional signal change from an area that has delayed reactivity. The shaded regions represent when hypercapnic stimulus was delivered.

statistic values using a single regressor, as is most common, it is assumed that all voxels increase at the same time, and only the magnitude of the responses differ. While time-delays in resting-state low frequency potentials have been an area of interest for some time[97], only recently have delays in the hyperemic response to vascular stimuli been evaluated. In the setting of vascular stimulus, such as carbon dioxide, one possible explanation for large time-delays in BOLD reactivity is that there is dysfunction in the endothelial and/or smooth muscle cells at the arteriole level. The time-delay observed in the BOLD signal in patients with vascular pathology (>>10 seconds) greatly exceeds any differences in blood arrival time[98,99]. Figure 15 shows an example of two BOLD time courses; one time course is the average whole-brain BOLD fractional signal change (blue), and the other is the average across voxels that have delayed response to vascular stimulus (red).

To determine voxel-wise reactivity delays, a jittered-regressor approach can be applied where a rectangular regressor is progressed in time, and at every regressor time point, z-statistic values are calculated[100]. Alternatively, more advanced cross-correlation analysis

can be used to determine time-delay based on individual hemodynamic response functions[101]. Using either of these methods, the time at which maximum correlation occurs can be determined, which is measured in seconds relative to stimulus start. Time-delay can also be reported in seconds relative to an individually determined hemodynamic response function, which may have advantages in settings of tissue impairment. The appendix of this dissertation details two methods for determination of time-delay from BOLD data.

While in healthy subjects, where the response to vascular stimulus is rapid, a single regressor approach may be appropriate assuming that the stimulus duration is sufficient to allow for plateau in BOLD signal change, and that the stimulus washout period is sufficient in length to allow for return to baseline signal. In the setting of vascular disease however, a single regressor analysis may contribute to error in z-statistic calculation. For example, a low z-statistic value could either be due to limited or non-existent vascular reserve capacity, or could be due to a significant delay in response to vascular stimulus, which results in lower correlation between the single regressor despite similar maximum fractional changes in the BOLD signal.

Additional contributions to decreased z-statistic measures should also be considered. Vascular steal refers to a pathophysiological process in which blood is diverted towards vascular beds with lower resistance[102]. In the setting of a brain region where arterioles are not able to dilate in response to vascular stimulus, blood may be diverted towards vascular beds able to dilate rapidly and therefore have lower resistance to flow. In the case of vascular steal, a negative BOLD response would be anticipated. Vascular steal in the central nervous system however is controversial, and studies evaluating blood flow response in stroke patients have found that the blood flow in the areas of negative BOLD signal are varied, with the majority patients not exhibiting a decrease in CBF in the area of negative BOLD signal, which would be consistent with vascular steal[103]. Future studies that evaluate vascular steal, time-delay, and other changes in physiology (such as increase in $CMRO_2$) in disease are required for a better understanding of decreased z-statistic values. Chapter 3 explores the contribution of reactivity time-delay to decreased CVR in stroke patients.

ASL vs BOLD for CVR

It should be noted that both ASL and BOLD can be used to measure CVR. When using ASL to evaluate CVR, the absolute change in CBF, in ml blood/100g tissue/minute, can be quantified between baseline and stimulus conditions. Generally, for every 1 mmHg increase in $EtCO_2$, which can be accomplished using hypercapnia, breath hold, or pharmacologic vasodilator, a 1-2 ml/100g tissue/minute increase in CBF is observed in healthy tissue. When using BOLD to evaluate CVR, the observable is changes in magnetic field dephasing (specifically transverse relaxation rates), which is dependent on multiple hemodynamic and metabolic constituents including CBF, CBV, OEF and $CMRO_2$. Due to this, in certain settings more quantitative methods, such as ASL and are preferred when evaluating CVR. However, use of ASL has limitations including artifacts that arise in the setting of long blood arrival times, labeling efficiency heterogeneity, and sensitivity to motion. Appropriate consideration of intravascular signal hyperintensities must be considered if quantifying CVR from ASL. Multi-PLD ASL, which affords the ability to determine bolus arrival time of magnetically labeled blood, can be used to address this issue; however, this approach extends scan time significantly or decreases the number of repeat-measures obtained within a given time interval[104,105]. Additionally, as discussed in the prior section, ASL is a subtraction technique, so even small movements can cause large calculation errors due to partial voluming. Lastly, the repetition time (TR) of ASL (~4 seconds) is generally longer than that of BOLD (~2 seconds), and requires both a control and label image, therefore ASL has lower temporal resolution.

Oxygen extraction fraction (OEF) with T_2-Relaxation-Under-Spin-Tagging (TRUST)

As previously discussed, deoxyhemoglobin is paramagnetic, and therefore induces changes in water signal in the presence of an externally applied magnetic field. The relative percent of oxygenated and deoxygenated hemoglobin has a known effect on the T_2 of blood[106]. In brief, T_2 is a time-constant that describes spin-spin dephasing; more paramagnetic deoxyhemoglobin results in a shorter T_2. The origin of this effect is that the magnetic fields created by the deoxyhemoglobin induce dephasing of water protons in the blood. Small

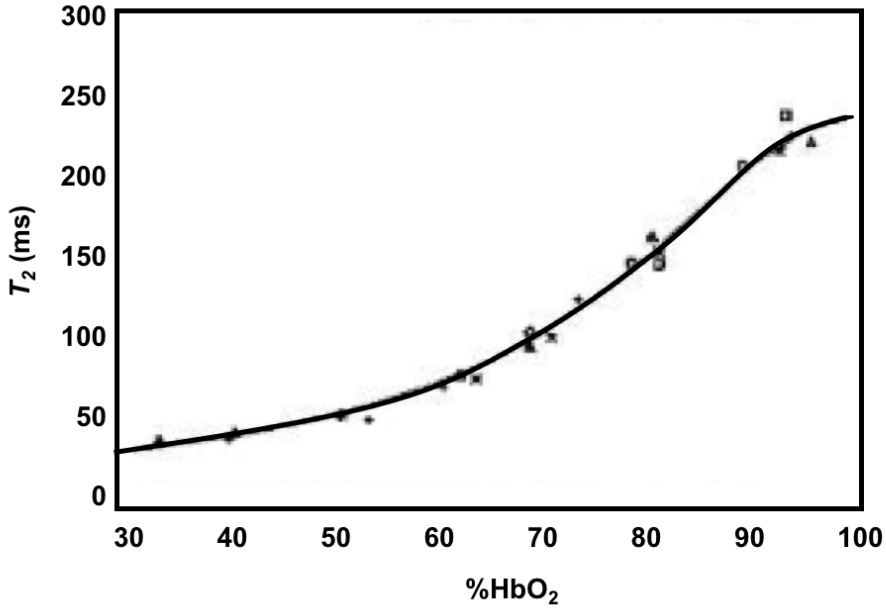

Figure 16. The relationship between oxyhemoglobin and T_2. Each point represents an *ex vivo* blood sample. To obtain a range of oxyhemoglobin levels (%HbO_2), prior to venipuncture the subject's arm was placed in cool water (decreased % HbO_2). Sample aeration was used to increase %HbO_2. From this data, a calibration plot can then be derived to determine %HbO_2 across a range of experimentally measured T_2 values. Figure from Wright et al., 1991[106].

gradients are established, and the dephasing induced by these gradients is proportional to the concentration of deoxyhemoglobin found in the red blood cell[107]. *In vitro* determination of the relationship between blood T_2 and percent oxyhemoglobin was first established by Wright et al. in 1991[106]. T_2 values were determined using a Carr-Purcell-Meiboom-Gill (CPMG) sequence, which uses a train of refocusing pulses following excitation. The duration of this pulse train is changed such that signal intensities at different effective echo times (eTEs) are determined, and therefore a T_2 decay curve can be fit. Experimentally-determined T_2 values in blood samples across a range of oxygenation levels combined with *in vitro* measurement of blood oxygenation, resulted in a calibration curve for this relationship and is shown in Figure 16. In the same paper, *in vivo* measurements of blood T_2 were obtained using a modified CPMG sequence, with additional sequence components addressing the effect of moving blood and surrounding tissue signal. The *in vivo* measurement of venous T_2

can then be converted to venous oxygenation (Y_v) with knowledge of the function that describes the calibration curve relating T_2 and Y_v.

Subsequent *in vivo* studies were performed based on this calibration model to determine OEF by calculating the fractional difference in arterial and venous oxygen content[108,109]. With knowledge of arterial oxygenation (Y_a), which is typically between 97-99% in healthy subjects, and can be easily measured by peripheral pulse oximetry, an oxygen extraction fraction can be determined by calculating the percent change in oxygen content, $(Y_a\text{-}Y_v)/Y_a$. These preliminary OEF studies were able to evaluate the relationship between oxygen metabolism and blood flow, demonstrating that upon functional activation CBF exceeds $CMRO_2$. Specifically, upon visual stimulation, draining veins from the activated brain region had higher amounts of oxygenated blood, and therefore longer T_2 values, when compared to control scans with no visual stimuli. These studies were fundamental to the understanding of operative hemodynamics during brain activation, and confirmed findings from PET studies evaluating the relationship between OEF and CBF during strong neural stimuli[110]. However, this method for determining OEF suffered from the inability to reliably isolate pure venous blood signal from surrounding tissue and cerebrospinal fluid (CSF). Partial voluming, especially with CSF which has a very long T_2, can lead to large calculation errors. Subject specific variations in arachnoid granulations, which are CSF filled projections of the arachnoid membrane into the dural veins, make isolation of blood from even large vessels difficult. Hand picking of voxels based on the combination of thresholded activation maps, literature reported T_2 values, and anatomic landmarks, was required in these studies.

The TRUST method, summarized in Figure 17, is based upon the relationship between Y_v and T_2 described in the aforementioned studies, but extends upon this prior work by applying principles of spin labeling to quickly and effectively isolate venous blood-water in the superior sagittal sinus (SSS)[111]. Instead of labeling inflowing arterial blood inferior to the imaging plane as is done in ASL, in TRUST, venous blood is labeled superior to the imaging plane. Following venous labeling, and allowing time for the labeled venous blood to drain into the SSS, a single slice containing the SSS is acquired. An important difference between TRUST and ASL is that in TRUST, the magnetically labeled blood-water does not mix with surrounding tissue, as blood-water in veins does not undergo exchange with

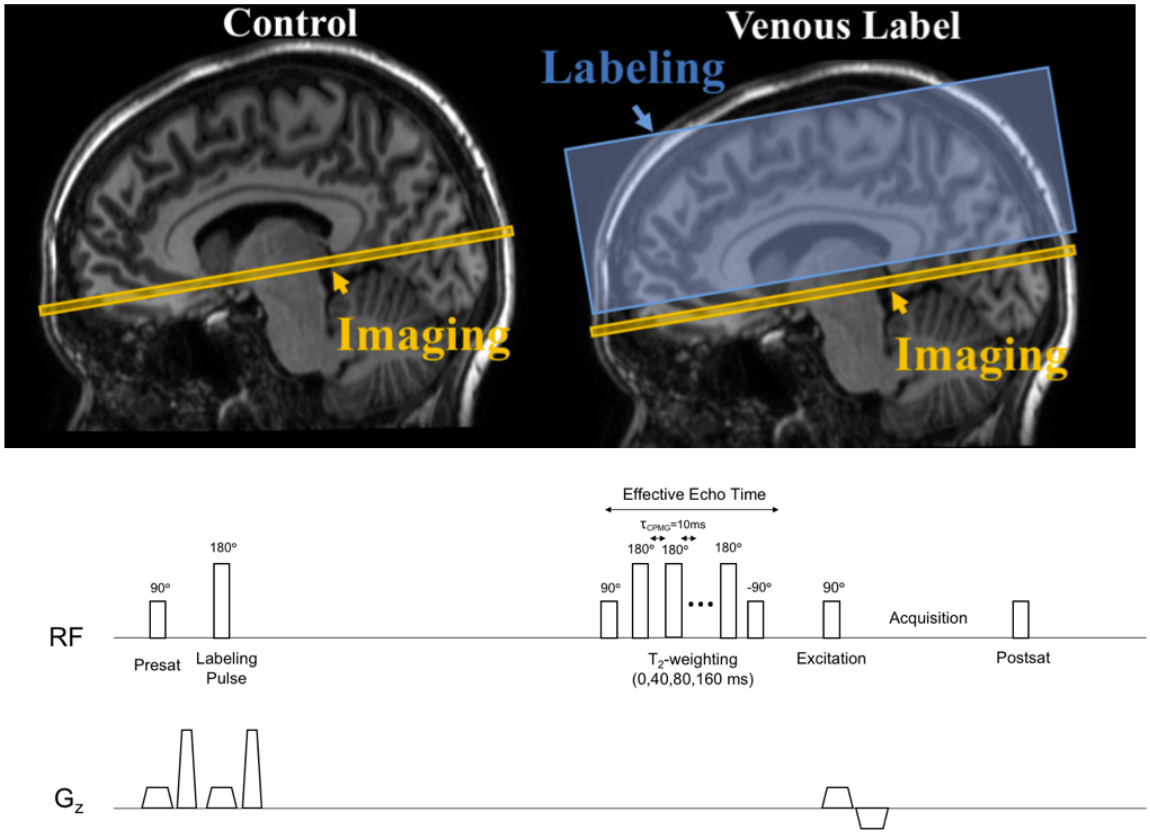

Figure 17. TRUST labeling. Venous labeling occurs superior to the imaging plane and attenuates venous blood signal. A delay then allows labeled venous blood-water to drain into the superior sagittal sinus, which is located within the imaging plane. Non-slice selective T_2-preparation pulses are then applied (0, 40, 80, and 160 ms train lengths) which confer T_2-weighting. A control scan is acquired without venous blood labeling, and subtraction of the label from the control allows isolation of venous blood. Plotting T_2 intensity values from subtracted images as a function of effective echo time allows for determination of venous blood T_2.

surrounding tissue. Following venous blood labeling, a non-slice selective refocusing CPMG pulse-train is applied to achieve T_2-weighting. This pulse train is performed for different lengths of time (0, 40, 80, 160 ms) in order to obtain different amounts of T_2-weighting, with longer pulse-trains allowing for more T_2 decay, and lower signal intensity. Identical to previous methods, the length of the pulse train is the eTE; the echo time (TE), which is the time between excitation and acquisition, is very short and only contributes minimally to the

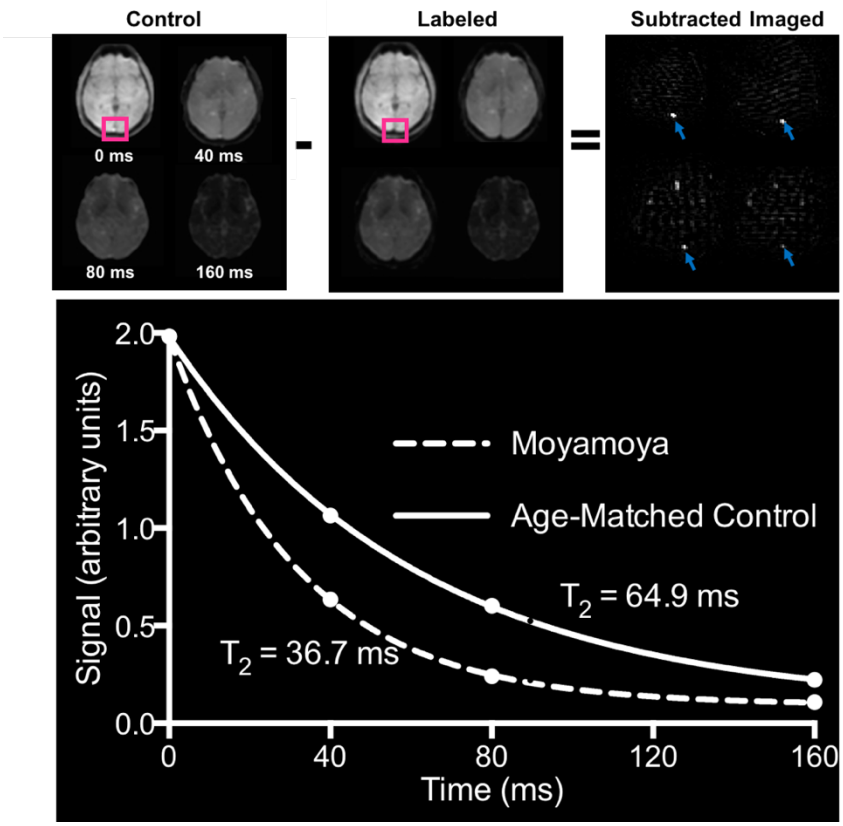

Figure 18. Control and label images in TRUST. Signal in the superior sagittal sinus (pink box) is attenuated in the venous labeled image. The control image contains static tissue signal and inflowing unlabeled blood signal. Subtraction of the label from the control image results in isolation of venous blood signal. The signal intensity from the subtracted images at each effective echo time (eTE) can be plotted as a function of eTE, and a T_2 decay curve can be fit. In the setting of normal range hematocrit values, a shorter T_2 (as is observed in the moyamoya participant) is a result of increased fraction of deoxyhemoglobin in the venous blood.

signal attenuation. By pair-wise subtracting the attenuated venous labeled image from the control image, which contains the static issue and unlabeled blood signal, an isolated venous signal is obtained at each eTE. It is then possible to determine the venous T_2 by plotting signal intensity in the SSS from the subtracted image as a function of eTE. An example of control, label, and subtracted images at different eTEs is shown in the top panel of Figure 18. The bottom panel of Figure 18 shows case examples. The healthy age-matched control has a venous T_2 of 64.9 ms. which is within range for healthy volunteers. In a patient with moyamoya disease, in which it is hypothesized that flow-limiting stenosis results in elevated oxygen extraction and therefore more venous deoxyhemoglobin, the T_2 is shorter. Using a

calibration plot similar to the plot shown in Figure 16, but determined *in vivo* using TRUST sequence parameters, the measured venous T_2 can be converted to Y_v and OEF can be determined. Blood gas manipulation of blood oxygen content combined with venous sampling has validated the TRUST method for accuracy of measuring venous oxygen content[112]. Additionally of note, this TRUST implementation takes only 1 minute 22 seconds to perform, and has been evaluated in a multi-site trial which found equivalent venous oxygenation results across sites once values were corrected for age; standard error across all sites was also determined to be small (1.4±0.6%)[113].

Comparison of MRI methods for measuring OEF

Methods for measuring OEF can be classified into groups depending on the contrast mechanism and compartment from which measurements are taken. TRUST only provides a global measurement of OEF, which has clear limitations. As such, advances have been made towards quantitation of regional and voxel-wise OEF. While the theory behind many of these methods is elegant, these methods require measurement of multiple additional physiological parameters, certain assumptions about complex biophysical systems, and/or manual selection of voxels for analysis, making their current use limited. I will summarize currently used methods for determination of regional OEF. Additional discussion is provided in Chapter 5.

One experimental method to perform voxel-wise OEF measurements is termed quantitative BOLD (qBOLD)[114]. This method is based on the theoretical model of BOLD contrast which relates measured susceptibility changes attributed to capillary and post-capillary-level field inhomogeneities to physiologic parameters of CBV, deoxyhemoglobin concentration, and OEF[115]. In order to solve for OEF using this theoretical model, assumptions need to be made regarding a suitable model for multi-compartment tissue structure, deoxyhemoglobin blood volume, microvascular hematocrit, vessel orientation (which is usually modeled as randomly oriented cylinders of infinite length), and contributions from macroscopic sources of field inhomogeneities (due to hardware imperfections and body-air interfaces). Calibrated BOLD methods, using gas administration,

are also used, which are based on measured susceptibility differences between baseline and stimulus conditions[116,117]. The calibrated BOLD method is rooted in an extravascular model for spin dephasing, despite 30% of the BOLD signal at 3T arising from the intravascular compartment[118].

T_2-Relaxation-Under-Phase-Contrast (TRU-PC), is an extension of the TRUST method, which quantifies venous oxygenation in other major veins and uses bipolar gradients to isolate venous blood signal from surrounding tissue[119]. This method has potential to provide more regional information, and exhibits excellent agreement when compared to TRUST for venous blood in the SSS. However, this method is still limited to large veins, which are midline in the brain. Therefore, this method does not provide hemispheric measures of venous oxygenation.

Quantitative Imaging of eXtraction of Oxygen and Tissue Consumption (QUIXOTIC[120]) and venous oxygenation mapping using Velocity-Selective Excitation and Arterial Nulling (VSEAN[121]), use velocity-selective labeling targeted at flow in the veins. A velocity selective pulse is applied at the null point of arterial blood such that only moving spins are labeled, and static tissue is not labeled. Voxel-wise maps are generated from these methods by extending the venous oxygenation measurements to surrounding brain tissue. As microvasculature blood volume is only ~5%, these methods are limited by low signal-to-noise, therefore they require many repeat measures. Additionally, the consideration of CSF and static tissue contribution to measured T_2 values is still not fully understood, and could potentially be a large source of error in these methods.

Quantitative susceptibility methods (QSM) methods (e.g. Phase-based Regional Oxygen Metabolism (PROM)) utilize the complex data from multi-echo gradient echo imaging to evaluate signal phase. QSM methods assume a cylinder structure of veins, and require either manual segmentation or restrictive masking to determine usable voxels for analysis. Substantial progress has been made using QSM however; a recent study by Kudo et al. 2016[122], compared hemispheric OEF ratios obtained from QSM to ^{15}O-PET measured OEF ratios in patients with unilateral carotid stenosis and found strong correlation between the modalities (r=0.62), but significant differences in absolute value measurements.

A limitation of all methods that evaluate venous oxygenation in small veins and microvasculature is limited knowledge regarding vessel hematocrit, which is known to decrease with vessel size[123]. Hematocrit has an inverse relationship with blood T_2[124]; therefore, incorrect assumptions about hematocrit could lead to errors. A potentially large limitation to qBOLD and QSM mapping in stroke patients is also the difficulty encountered when considering patients with prior hemorrhage, in which large areas of dephasing occur, but not due to venous oxygenation changes.

	BOLD	Intravascular T_2	Susceptibility
MRI observation	T_2, T_2* (magnitude)	T_2 relaxation	Signal phase
Baseline values?	Difficult	Yes	Yes
Regional?	Tissue voxel-wise maps	Large draining veins (TRUST/TRU-PC); Voxel-wise maps (QUIXOTIC, VSEAN)	Large draining veins, small pial veins
Major challenge	Complex biophysical model, extravascular model (calibrated BOLD)	Global (TRUST/TRU-PC); Isolation of blood signal (QUIXOTIC, VSEAN)	Partial voluming, manual selection of oriented vessels
Methods	qBOLD[114] Respiratory calibrated BOLD[116, 117]	TRUST[111], TRU-PC[119] QUIXOTIC[120], VSEAN[121]	QSM/ PROM[122]

Table 3. Methods for evaluating oxygen extraction fraction. Table adapted from Fan et al. 2017[125].

Table 3 contains a summary of current methods being used to evaluate global, regional, and voxel-wise OEF. Overall, there is still substantial work that can be done in this area to develop tools that are robust and validated, but also clinically deployable. Chapter 5 of this dissertation addresses another potential approach to measuring hemispherical and regional OEF, by adapting the TRUST method to isolate signal from a more restricted (hemisphere, sub-region) area of interest.

1.4 Overview

The overall theme of this dissertation work is to develop and implement non-invasive neuroimaging protocols capable of quantifying hemodynamic and metabolic biomarkers of tissue health, and to apply these methods to test focused hypotheses regarding tissue impairment and improvement following intervention in patients with intracranial stenosis. In intracranial disease, hemodynamic compensation occurs in order to maintain tissue perfusion and oxygenation downstream of stenosis. To understand the underlying physiology of hemodynamic impairment in these patients, and find sensitive markers of tissue-level impairment, I have employed hemo-metabolic imaging methods in addition to standard structural imaging. These hemo-metabolic imaging methods include T_2^*-weighted BOLD imaging with the vasostimulatory gas carbogen (5% CO_2/95% O_2) to assess changes in cerebrovascular reactivity, pCASL to assess blood flow dynamics, and TRUST to measure whole-brain OEF. Additionally, I have extended upon the current implementation of TRUST with the goal of being able to obtain hemispheric and regional measures of OEF. Together, these projects share the common theme of evaluating tissue level compensation mechanisms using non-invasive methods in patients with intracranial stenosis. Future work evaluating outcomes such as recurrent TIA or stroke in patients with intracranial disease will determine if these tools are suitable as clinical tests to assess stroke risk.

CHAPTER 2

ELEVATED OXYGEN EXTRACTION FRACTION IN INTRACRANIAL DISEASE

2.1 Purpose

To evaluate a potential marker of global hemodynamic impairment (oxygen extraction fraction, OEF: ratio of oxygen consumed to oxygen delivered) in cerebrovascular disease compared to healthy controls. I specifically focus on patients with intracranial stenosis due to moyamoya, and compare measures of global OEF and blood flow to healthy control participants. To our knowledge, detection of globally elevated OEF using MRI in the setting of intracranial stenosis has not been reported. Previous studies using ^{15}O-PET have identified OEF elevation as predicative of future stroke event. Evaluation of elevated OEF using MRI in patients with elevated stroke risk is therefore important, and will determine if this method is sensitive to hemodynamic impairment in patients with intracranial disease.

2.2 Summary

Moyamoya syndrome is a bilateral, complex cerebrovascular condition characterized by progressive non-atherosclerotic intracranial stenosis and collateral vessel formation. Moyamoya treatment focuses on restoring cerebral blood flow (CBF) through surgical revascularization, however stratifying patients for revascularization requires abilities to quantify how well parenchyma is compensating for arterial steno-occlusion. Globally elevated OEF secondary to CBF reduction may serve as a biomarker for tissue health in moyamoya patients, as suggested in patients with sickle cell anemia (SCA) and reduced oxygen carrying capacity. In this study, OEF was measured using T_2-relaxation-under-spin-tagging (TRUST) to test the hypothesis that OEF is globally elevated in patients with moyamoya (n=18) and SCA (n=18) relative to age-matched controls (n=43). Mechanisms underlying the hypothesized OEF increases were evaluated by performing sequential CBF-weighted, cerebrovascular reactivity (CVR)-weighted, and structural MRI. Patients were

stratified by treatment and non-parametric tests applied to compare study variables (significance: two-sided $P<0.05$). OEF was significantly elevated in moyamoya participants (interquartile range=0.38-0.45) compared to controls (interquartile range=0.29-0.38), similar to participants with SCA (interquartile range=0.37-0.45). CBF was inversely correlated with OEF in moyamoya participants. Elevated OEF was only weakly related to reductions in CVR, consistent with basal CBF level, rather than vascular reserve capacity, being most closely associated with OEF.

2.3 Introduction

Moyamoya is characterized by progressive stenosis of the supraclinoid internal carotid arteries (ICAs) and their proximal branches and the corresponding development of collateral blood vessels[18]. Moyamoya can be idiopathic (i.e., disease) or secondary (i.e., syndrome) to more common cerebrovascular conditions such as atherosclerosis and Down's syndrome, and places patients at more than a seven-fold risk increase for stroke[126].

Stroke screening procedures for patients with moyamoya, which can be used to prescribe prophylactic revascularization procedures[127], focus on characterizing large vessel steno-occlusion using angiographic techniques at the spatial resolution of major arteries, as well as evaluating prior infarct presence and extent. While helpful, these methods are not conclusive for prognosis, and, due to the invasive nature of many of these methods, are not used routinely for surveillance owing to safety concerns. Therefore, there is a need to better understand the pathophysiology of moyamoya and to develop associated stroke screening protocols.

Due to the highly variable way in which brain parenchyma may compensate for the array of arterial steno-occlusions in moyamoya, as well as inabilities of angiographic techniques to identify all microvascular stenoses at available spatial resolutions, tissue-level imaging is of great interest and required for characterizing how parenchyma compensates for large vessel steno-occlusion. More specifically, brain parenchyma downstream of arterial stenosis may compensate for reduced perfusion pressure through the formation of collateral vessels[128, 129] and/or increasing arteriolar cerebral blood volume (CBV, ml blood/ml

parenchyma) through autoregulatory vasodilation[64, 130,131]. While collateral vessels can be evaluated with gold-standard catheter angiography, it is also important to understand the function of these collaterals specifically and whether these collaterals adequately maintain oxygen delivery to tissue. This issue is fundamental, as patients with nearly identical degrees and extents of measureable stenosis may carry contradistinct stroke risks due to different compensation mechanisms and extents of collateralization[128, 132]. When the extent of collateralization and/or autoregulation is insufficient to maintain adequate oxygen delivery to tissue, the OEF will increase as described by Equation 1:

$$Oxygen\ extraction\ fraction\ (OEF) = \frac{oxygen\ consumed}{oxygen\ delivered} = \frac{CMRO_2}{CBF \cdot C_a} \quad [1].$$

where $CMRO_2$ is the cerebral metabolic rate of oxygen consumption (ml O_2/100g tissue/min), CBF is the cerebral blood flow (ml blood/100g tissue/min) and C_a is the oxygen carrying capacity of arterial blood, which depends on the arterial oxygen saturation and total hemoglobin. For constant $CMRO_2$, which is believed to be preserved up until very advanced stage disease[64], OEF may increase (i) for normal CBF and reduced oxygen carrying capacity[133], or (ii) for normal oxygen carrying capacity but reduced CBF[64].

Indeed, based on ^{15}O-PET studies in individuals with extracranial and intracranial steno-occlusion, it has been shown that OEF increases regionally when CBV is inadequate to maintain CBF over a normal range, and importantly that regionally elevated OEF is prognostic for recurrent stroke risk[64,65]. It has also been shown that in patients with symptomatic carotid occlusion due to atherosclerosis, increased OEF is associated with prior stroke or transient ischemic attack (TIA)[66]. Iwama et al. evaluated a cohort of patients with moyamoya using ^{15}O-PET and elevated OEF was identified in middle cerebral artery flow territories in patients with moyamoya configuration compared to adults without moyamoya disease[134]. This work has motivated the potential use of OEF as a biomarker of stroke risk in patients with moyamoya, however difficulty performing ^{15}O-PET routinely in non-specialized centers has limited translation of these promising findings, as well as

mechanisms underlying these elevated OEF measurements in patients with moyamoya have not been thoroughly clarified.

More recently using non-invasive MRI, it has been shown that OEF increases globally in patients with reduced oxygen carrying capacity secondary to SCA and elevated OEF correlates with increasing levels of clinical impairment defined as vasculopathy or prior stroke[133]. Such MRI methods for determining global OEF have additionally been applied across the lifespan of healthy individuals[79], as well as in end-stage renal disease[135], anorexia nervosa[136] and neonates[137], all populations in which cerebrovascular oxygen metabolism and hemostasis is thought to be abnormal.

The purpose of this work is to extend these promising OEF studies to patients with moyamoya to test the hypothesis that owing to the known, bilateral nature of the disease and associated hypoperfusion, globally elevated OEF is detectable using an MRI-based approach. Two supplemental objectives are also of interest: 1) To confirm the mechanistic origin of the hypothesized OEF elevation by performing OEF and CBF measurements in sequence in patients with steno-occlusive disease due to moyamoya and in patients without steno-occlusive disease but reduced oxygen carrying capacity secondary to SCA and 2) To evaluate the relationship between cerebrovascular reactivity (CVR) and the hypothesized globally elevated OEF. CVR studies have been performed in patients with arterial steno-occlusion due to moyamoya and atherosclerosis using computed tomography[138], single-photon emission computed tomography[139], PET[140,141], and MRI[84,142]; however to our knowledge no study has evaluated the relationship between basal CBF, CVR, and global elevations in OEF in patients with moyamoya.

Results of this work are intended to improve our understanding of the mechanism by which brain parenchyma compensates for multiple arterial steno-occlusions in moyamoya, and to determine if OEF is globally elevated in moyamoya, which is logical but not confirmed. If confirmed, this work could provide a foundation for future investigations that may evaluate the utility of using fast and non-invasive measures of OEF as an additional biomarker of tissue impairment and stroke risk in patients with moyamoya.

2.4 Materials and Methods

Ethical considerations and participant groups

All participants (n=79) provided informed, written consent for this prospective IRB-approved study. Participants were grouped into four categories: (i) moyamoya participants, (ii) age-matched controls for moyamoya, (iii) SCA participants, (iv) age-matched controls for SCA. Inclusion criteria for the SCA arm included adult participants homozygous for hemoglobin-S on oral hydroxyurea therapy, not receiving routine blood transfusions, and without significant (>70%) steno-occlusion of any major intracranial (first segment of ACA, PCA and MCA) or cervical artery (to control for heterogeneity). All SCA participants were recruited between 2014 and 2016 from a comprehensive SCA clinic at our institution. Inclusion criteria for the moyamoya arm was clinical diagnosis of moyamoya and prior TIA or stroke; exclusion criteria included extracranial carotid stenosis >50% and anemia. Moyamoya participants were recruited between 2014 and 2016 from the adult neurological surgery service at our institution either during clinic appointments or during a follow-up call after the patient was seen in clinic. Revascularization surgery and location was recorded in patients and sub-analyses were performed to understand how revascularization was associated with the findings. Importantly, a heterogeneous group of moyamoya patients was included, with varying degrees of steno-occlusion and time since diagnosis. This enables a large range of hemo-metabolic parameters to be contrasted to evaluate the study hypotheses, and also increases generalizability beyond a limited and unrepresentative cohort (e.g., short disease duration without revascularization). No control participants for the moyamoya or SCA arm had a history of anemia, significant vasculopathy defined as >70% extracranial or intracranial stenosis, or sickle trait. All components of this study were performed in compliance with the Declaration of Helsinki, Health Insurance Portability and Accountability Act, and all protocols were approved by the Vanderbilt University Institutional Review Board (IRB Study 111116 – control participants; IRB Study 110468 – moyamoya participants; IRB Study 140915 – SCA participants).

Image acquisition

All MR imaging and angiography was performed on a 3 Tesla (T) scanner (Philips Healthcare, Best, The Netherlands) using body coil radiofrequency transmission and SENSitivity Encoding (SENSE)-array reception.

(i) Structural imaging and angiography. FLuid-Attenuated-Inversion-Recovery (FLAIR; TR/TE=11000/120 ms) and T_1-weighted (TR/TE=9.0/4.6 ms) MRI were performed in the same scan session as hemodynamic and metabolic imaging. All participants with moyamoya underwent digital subtraction angiography (DSA) of the neck and intracranial arteries within 60-days of MRI for stenosis assessment. Participants with SCA and control participants underwent time-of-flight magnetic resonance angiography (MRA) of the neck and intracranial arteries either in the same session, or within 30-days of MRI for stenosis assessment.

(ii) CBF imaging. CBF-weighted images were obtained from pseudo-continuous arterial spin labeling (pCASL) data. pCASL data from 13 control-label pairs were pair-wise subtracted and used to generate the mean difference magnetization, which was then normalized by a proton-density-weighted (TR=15,000 ms) equilibrium magnetization image. While pCASL labeling schemes with similarly long post labeling delay (PLD) times were used in all subjects, the PLDs did vary over a small range between some controls and patient volunteers. The PLD range was 1.53-1.9s and label duration range was 1-1.65s. These parameters have been investigated in more detail previously[98,133], and variation in quantified CBF due to variation in these parameters[143] is anticipated to be much smaller than differences in CBF due to reduced oxygen carrying capacity or steno-occlusion. The reason for the range in PLD and label duration values in this participant cohort is that the scans were obtained over a 3-year period in which small modifications to the scan protocol were made. A list of the the scan parameters is provided in the Discussion section. Phase contrast has been previously used to determine labeling efficiency in SCA participants who have known elevated cervical blood velocity; consistent with these results, a labeling efficiency of 0.60 was used for SCA participants, and a labeling efficiency of 0.85 was used for all other volunteers[144].

(iii) OEF imaging. Whole brain OEF values were quantified using the non-invasive MRI approach T_2-relaxation-under-spin-tagging (TRUST)[111,112]. To perform TRUST, data from an imaging slice containing the inferior portion of the superior sagittal sinus were motion-corrected and pair-wise subtracted at four effective echo times (eTEs) of 0, 40, 80, and 160 ms for both label and control images. The imaging plane (3.4x3.4x5 mm^3) was placed 20 mm superior to the confluence of the sinuses for both the control and label images. TRUST duration was 1min12s. Additional details of TRUST acquisition are included in Chapter 1.

(iv) Cerebrovascular reactivity imaging. Cerebrovascular reactivity (CVR) was assessed in moyamoya participants. All moyamoya participants were fitted with a nasal cannula (Salter Labs, Ref 400F) for end tidal CO_2 ($EtCO_2$) monitoring and a non-rebreathing mask (Salter Labs, ref 8130) for administration of medical grade room air (21% O_2, 79% N_2) and hypercapnic hyperoxia (i.e., carbogen-5: 5% CO_2, 95% O_2). Medical grade carbogen, rather than hypercapnic normoxia, was required in high-risk patients at our center by our ethical review board, and this stimulus has been shown to correlate with hypercapnic normoxic stimuli and to provide expected sensitivity to lateralizing stenosis in patients with intracranial stenosis[84]. The CVR was assessed using a paradigm consisting of two blocks of 3-minute carbogen administration interleaved with 3-minute blocks of medical grade room air. Blood pressure, $EtCO_2$ and oxygen saturation were monitored by a respiratory therapist. Gradient echo BOLD images were acquired with a spatial resolution of 3x3x3.5 mm^3 with TE/TR of 35/2000 ms.

Analysis

(i) Structural imaging and angiography evaluation. Stenosis and infarct grading was performed by a board-certified neuroradiologist to ensure inclusion criteria and appropriate group assignment. Moyamoya classification was assigned based on clinical criteria and DSA data that were separately acquired as part of the clinical work-up for these patients[18]. FLAIR images were evaluated for presence and size of infarct. In addition, for moyamoya participants, a modified Suzuki score (mSS) was calculated for each hemisphere[145]. The

range is 0 to 4, with 0 representing no steno-occlusive changes and 4 representing complete occlusion of both proximal anterior and middle cerebral arteries.

(ii) CBF determination. Voxel-wise CBF analysis was performed according to the ISMRM Perfusion Study Group guidelines using pCASL. Specific post-labeling delays and label durations used for the participants in this study are provided in Table 5[87]. CBF was quantified in native space for each voxel and then transformed into a 2 mm T_1 -weighted Montreal Neurological Institute atlas using the FMRIB Software Library[146,147]. Due to the dependence of hematocrit on $T_{1,blood}$ [89], the $T_{1,blood}$ was determined individually for the SCA participants, and the mean arterial $T_{1,blood}$ for this group was 1900±53 ms. For the non-anemic control and moyamoya participants, the $T_{1,blood}$ for males and females was assumed to be 1671 ms and 1700 ms, respectively, which accounts for males having a higher mean hematocrit than females. Mean gray matter CBF (GM CBF) was calculated and reported as region-of-interest CBF, and a partial volume calculation was performed based on structural determination of white and gray matter contribution to the imaging voxel; these values are reported as partial volume corrected, GM CBF. Gray matter was the focus of the analysis due to the approximately two-fold longer arterial blood arrival times in white matter, which are on the order or longer than arterial blood-water T_1. Measured CBF values were scaled by a common factor of 1.22, to convert the voxel CBF measurement to a gray matter CBF measurement. This factor was calculated by measuring the fraction of gray and white matter in the common mask and using voxel partial volume estimates from FSL FAST and the T_1-weighted structural images, which were determined to be 70% gray matter and 30% white matter, and did not vary significantly between groups or patients. We also applied the relationship that white matter CBF is 2.5-fold lower than gray matter CBF[148]. It should be noted that this procedure slightly increases the reported CBF for all volunteers, but does not change any trends between volunteers or groups.

(iii) OEF determination. The quantification procedure has been outlined in detail in the literature and Chapter 1[111,112]; in brief, Carr-Purcell-Meiboom-Gill (CPMG) T_2 was calculated in the sagittal sinus for each participant by performing pair-wise subtraction of

the label from the control image at the four effective echo times (eTE). Four voxels within the sagittal sinus were analyzed for each subject at each eTE to determine the pure-blood (CPMG)-T_2. CPMG-T_2 is then converted to venous oxygenation (Y_v) using knowledge of blood-water T_2, Y_v, and hematocrit[112]. The standard error of the Y_v measurement, from which OEF was calculated, was calculated for each participant to determine if the error in fitting differed between groups. Arterial oxygenation (Y_a), which was recorded for each participant using pulse oximetry at time of the TRUST scan, was incorporated to calculate OEF as (Y_a-Y_v)/Y_a. This equation assumes that oxygen dissolved in blood plasma contributes minimally to OEF[133]. A diagram of the labeling and acquisition plane are shown in Figure 17.

(iv) CVR determination. FSL software[146] was used for motion correction, baseline drift correction and z-statistic calculation. In addition, the relative signal change ($\Delta S/S_0$) was determined as the mean difference in the signal during the final 30s of the carbogen block divided by the baseline signal, similar to as previously described[84]. Data were registered to 4 mm T_1 -weighted Montreal Neurological Institute and a gray matter region of interest (GM ROI) was used to determine mean GM CVR. Data were normalized by change in $EtCO_2$ in units of mmHg.

Statistical concerns and hypothesis testing

The primary objective of this study was to quantify OEF in participants with clinical diagnoses of moyamoya, and to compare these measurements to participants with SCA and to healthy age-matched controls. The primary hypothesis was that participants with moyamoya will have increased OEF and decreased CBF compared to age-matched controls, whereas SCA volunteers will have increased OEF and increased CBF (but reduced oxygen carrying capacity). To test this hypothesis, a two-sided Wilcoxon rank-sum test was performed. A supplemental objective was to confirm the mechanistic origin of OEF elevation by performing OEF and CBF measurements to test the hypothesis that moyamoya participants with hypoperfusion (decreased CBF), have increased OEF, and a Spearman's rank coefficient was calculated. To evaluate the relationship between CVR and globally

elevated OEF, a Spearman's rank coefficient was also calculated. In all comparisons, two-tailed P-value<0.05 was required for significance. Additionally, for the primary and supplemental objectives, a sub-analysis of the moyamoya participants was performed whereby non-revascularized participants were evaluated separately to determine whether the findings were preserved

2.5 Results

Demographics

Table 4 summarizes participant demographics and calculated OEF and CBF values. 18 participants with primary (n=16) or secondary moyamoya (n=2) (mean age = 47 years; range = 26-79 years) were included. Nine of the moyamoya participants had prior indirect revascularization, which comprised either encephalo-duro-arterio-synangiosis (EDAS; n=8) or encephalo-duro-arterio-myo-synangiosis (EDAMS; n=1). Of the participants who underwent revascularization, neuroimaging was performed at least five months post-operation and these participants were also considered separately to understand if revascularization affected the study hypothesis. 18 participants with SCA were included (mean age = 27 years; range = 19-32 years). Control participants were enrolled to obtain age-matched data sets for the moyamoya (mean age = 44 years; range = 21-75 years) and SCA cohorts (mean age = 26 years; range = 21-39 years). A larger cohort of age-matched control volunteers for the moyamoya arm of the study were included due to the larger age-range of moyamoya participants (range = 26-79 years). Hematocrit was measured for most SCA participants on the day of imaging, and all within seven days of imaging. The mean (%) hematocrit in SCA participants was 28.6±2.5. For moyamoya participants, the mean mSS for the right and left hemispheres were 2.4 and 1.9, respectively. No participants had moyamoya secondary to SCA. Prior stroke or TIA was an inclusion criterion for the moyamoya arm of the study and 15/18 of the participants had remote infarcts (defined as I_1 hypointense, FLAIR hyperintense lesions>3 mm). Of the SCA participants, 8/18 had remote infarcts.

	Moyamoya arm		Sickle cell anemia (SCA) arm	
Parameters	Controls (n=43)	Moyamoya (n=18)	Controls (n=11)	SCA (n=18)
Age (years)	44.8 ± 21.7	47.2 ± 14.9	26.5 ± 5.1	27.0 ± 5.1
Hemoglobin S (%)	0	0	0	75.6 ± 10.3
Gender (% male)	71	5	45	55
Arterial oxygen saturation (%)	97.1 ± 1.2	97.2 ± 1.3	97.3 ± 1.2	95.6 ± 1.8
Venous oxygen saturation (%)	63.7 ± 6.0	56.3 ± 7.7	62.4 ± 5.1	56.5 ± 5.7
Standard error of Y_v (%)	1.62	1.50	1.41	0.83
TRUST-measured T_2 (ms)	68.0 ± 1.2.2	59.6 ± 11.8	65.7 ± 10.2	78.0 ± 11.4
Oxygen extraction fraction	0.343 ± 0.061	0.419 ± 0.083	0.359 ± 0.052	0.410 ± 0.056
Region-of-interest cerebral blood flow, (ml blood/ 100g tissue/minute)	40.2 ± 10.3	36.4 ± 8.8	42.2 ± 7.1	69.3 ± 15.2
Gray matter cerebral blood flow, partial volume corrected (ml blood/100g tissue/minute)	49.2 ± 12.5	44.4 ± 10.7	51.4 ± 8.6	85.3 ± 19.4
Modified Suzuki score, right hemisphere	NA	2.44 ± 0.86	NA	NA
Modified Suzuki score, left hemisphere	NA	1.89 ± 0.96	NA	NA
Infarct on FLAIR imaging >3mm (%)	0	83	0	44

Table 4. Summary of study participants. Continuous variables reported as mean±standard deviation.

OEF and CBF

Figure 19 summarizes case examples of structural and functional imaging data from a representative control participant, participant with SCA, and a participant with moyamoya. In Figure 19A, a control participant with a normal OEF and normal findings on structural and CBF imaging is shown. This is contrasted with a participant with SCA (Figure 19B) and moyamoya (Figure 19C), both of whom have elevated OEF of 0.481 and 0.412, respectively. The participant with SCA has a venous oxygen saturation of 48% and the participant with moyamoya has venous oxygen saturation of 57%, both lower than the venous oxygen saturation of the control (62%) and consistent with elevated OEF for the measured range of arterial blood oxygen saturation. The participant with SCA demonstrates elevated CBF in the setting of decreased oxygen carrying capacity (i.e. reduced hematocrit). The participant with bilateral moyamoya demonstrates right and left anterior/middle cerebral artery territory infarcts, bilateral hypoperfusion on CBF imaging, and elevated OEF.

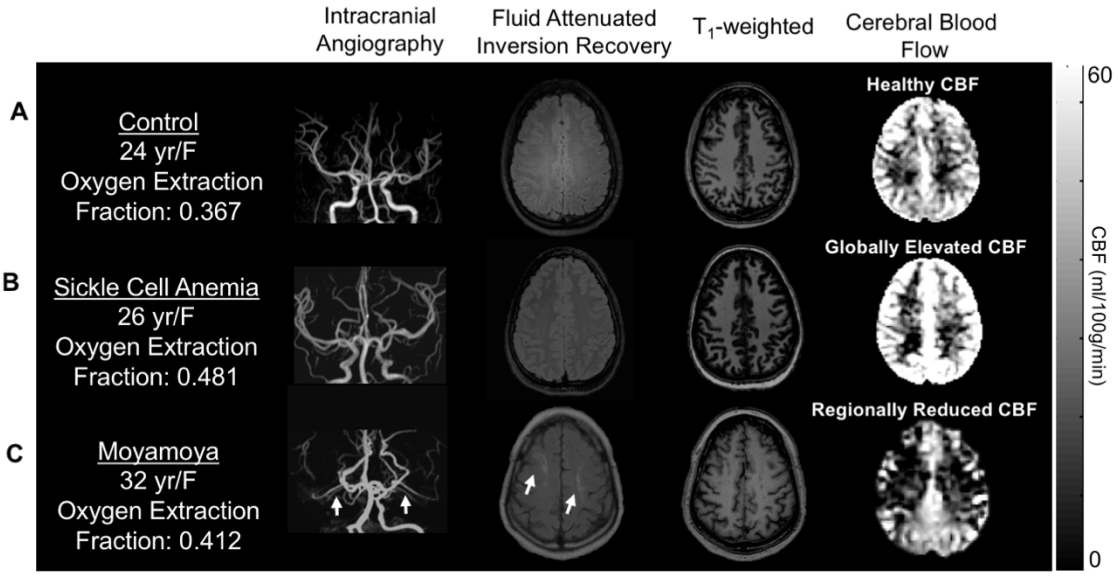

Figure 19. Structural, CBF, and OEF imaging. (A) A healthy control participant with a normal OEF, and normal findings on structural and CBF imaging. (B) A participant with sickle cell anemia (SCA) and (C) moyamoya. The participant with SCA demonstrates elevated CBF in the setting of decreased oxygen carrying capacity of hemoglobin and increased OEF (OEF=0.481). The participant with bilateral moyamoya with lenticulostriate collaterals (white arrows on intracranial angiography), demonstrates right and left anterior and middle cerebral artery territory infarcts seen on FLAIR, bilateral anterior-territory hypoperfusion, and globally elevated OEF (OEF=0.412) relative to control data.

Group-analysis of data in SCA and moyamoya participants is shown in Figure 20. OEF values (mean±s.d.) of moyamoya participants (OEF=0.419±0.083) compared to age-matched controls (OEF=0.343±0.061) are shown in Figure 20A. These data are consistent with the primary hypothesis of the study that OEF is elevated in participants with moyamoya (P<0.001). GM CBF values (mean±s.d.) of age-matched controls (CBF=49.2±12.5 ml/100g/min) and moyamoya participants (CBF=44.4±10.7 ml/100g/min) are summarized in Figure 20B. A trend for a reduction in mean GM CBF in moyamoya participants compared to control participants was observed, however this did not meet criteria for significance (see Discussion). To better understand OEF in the context of moyamoya patients who had not undergone revascularization procedure (n=9) vs. those that had undergone revascularization (n=9), we considered the groups separately in a sub-analysis. OEF was similarly and significantly elevated in participants who had not undergone revascularization (P=0.0023)

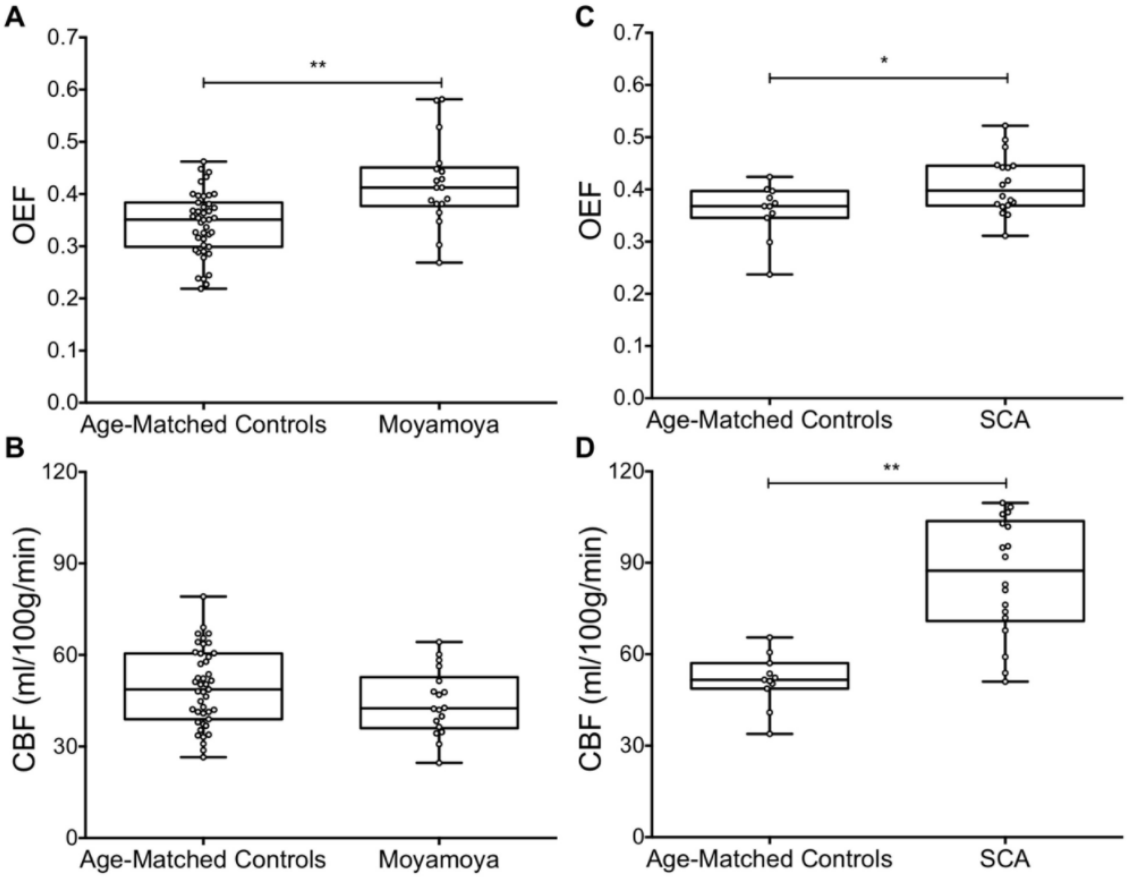

Figure 20. OEF and CBF in moyamoya. A two-sided Wilcoxon rank-sum test was performed to test the primary hypothesis that OEF was elevated in moyamoya and SCA participants compared to age-matched controls, and that CBF was decreased in moyamoya participants compared to controls. (A) OEF is elevated in moyamoya participants compared to age-matched controls (P<0.001). (B) Reduced mean whole-brain CBF in moyamoya participants relative to controls, but this reduction was not significant, likely due to preserved posterior territory CBF in many patients and regions of high ASL intravascular signal. (C) OEF is elevated in SCA participants compared to age-matched controls (P=0.045). (D) CBF is elevated in SCA participants compared to age-matched controls (P<0.001). *P<0.05, **P<0.01. In the moyamoya arm of the study, a sub-analysis was performed that evaluated only females in both the control (n=15) and moyamoya (n=17) groups. Trends were identical, and the OEF was elevated in the moyamoya participants compared to the controls (P=0.06), and CBF was decreased in the moyamoya participants comparted to controls (P=0.02).

and participants who had undergone revascularization surgeries (P=0.026), compared to age-matched controls, even with these smaller sample sizes. There was no significant difference in OEF values between participants who had undergone revascularization and participants who had not undergone revascularization, however the study may not be powered

sufficiently to investigate this effect rigorously. When considering the SCA arm of the study, OEF was significantly elevated in participants with SCA (OEF=0.410±0.056) compared to age-matched control participants (OEF=0.359±0.052) and summarized in Figure 20C. Additionally, GM CBF values in SCA participants (CBF=85.3±19.4 ml/100g/min) were significantly elevated compared to age-matched controls (CBF=51.4±8.6 ml/100g/min) and summarized in Figure 20D. The standard error of the Y_v measurement across all participant groups was less than 2%, and there was no difference in confidence intervals or standard error measurements of the T_2-decay curve-fitting calculation from the TRUST-MRI imaging of OEF.

Mean CBF maps for each participant group are shown in Figure 21. Central slices of the T_1-weighted atlas with the gray matter mask used for quantification overlaid are shown in Figure 21A. Mean CBF maps from controls and SCA participants are shown in Figure 21B and Figure 21C, respectively. Figure 21D shows mean CBF maps from moyamoya participants (n=18). Mean CBF maps from moyamoya participants with bottom quartile OEF values (OEF<0.38), and moyamoya participants with upper quartile OEF values (OEF>0.45) are shown in Figure 21E and Figure 21F, respectively.

Hemo-metabolic Relationships in Moyamoya between CBF, CVR and OEF

To evaluate our supplemental objectives, we analyzed the relationship between the hemo-metabolic parameters of CBF, CVR an OEF in participants with moyamoya. In a sub-analysis we included only patients without prior surgical revascularization. The (mean±s.d.) change in $EtCO_2$ during the hypercapnic CVR study in moyamoya participants was 4.82±2.15 mmHg and the BOLD signal change during hypercapnia normalized by baseline signal strongly correlated with z-statistic values (ρ=0.80, P=<0.0001). BOLD-weighted CVR positively trended with CBF when considering all moyamoya participants (Figure 22A; ρ=0.43, *P*=0.073) and only moyamoya participants undergoing surgical revascularization (Figure 22B; ρ=0.40, *P*=0.29), however these findings did not meet criteria for significance. The rank-sum coefficient was nearly identical in both cases, but the p-values differed owing to differences in the sample sizes. Next, to understand the mechanistic origin of the

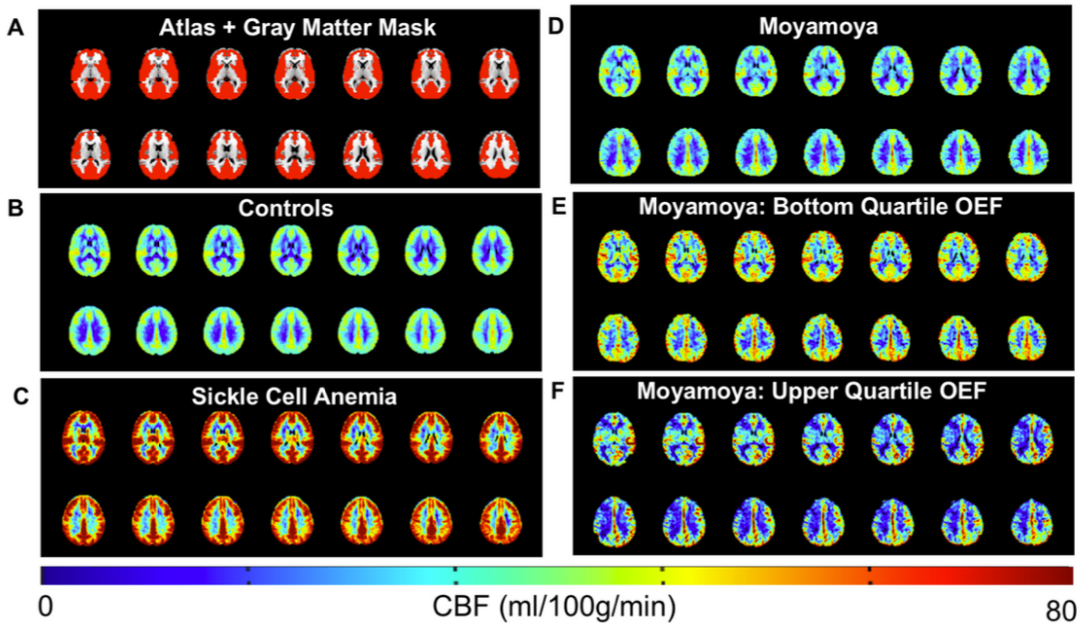

Figure 21. CBF imaging using pCASL. Central slices of a T_1-weighted atlas with gray matter mask (red) overlaid are shown in (A). Mean CBF maps in healthy controls (n=43) and participants with sickle cell anemia (n=18) are shown in (B and C). (D) shows mean CBF maps from moyamoya participants (n=18). Mean CBF maps from moyamoya participants with with bottom quartile OEF values (OEF<0.38), and moyamoya participants with upper quartile OEF values (OEF>0.45) are shown in (E) and (F), respectively.

hypothesized OEF elevation due to decreased CBF in moyamoya participants, we evaluated the relationship between OEF and CBF and found a significant inverse relationship between CBF and OEF when considering all moyamoya participants (Figure 22C; ρ=-0.56, *P*=0.016) and a trend in moyamoya participants who had not undergone surgical revascularization (Figure 22D; ρ=-0.62, *P*=0.082), however this latter relationship did not meet criteria for statistical significance. There was only a weak and non-significant inverse relationship between CVR and OEF when considering all moyamoya patients (Figure 22E; ρ=-0.13, *P*=0.082) and moyamoya participants who had not undergone surgical revascularization (Figure 5F; ρ=-0.26, *P*=0.50).

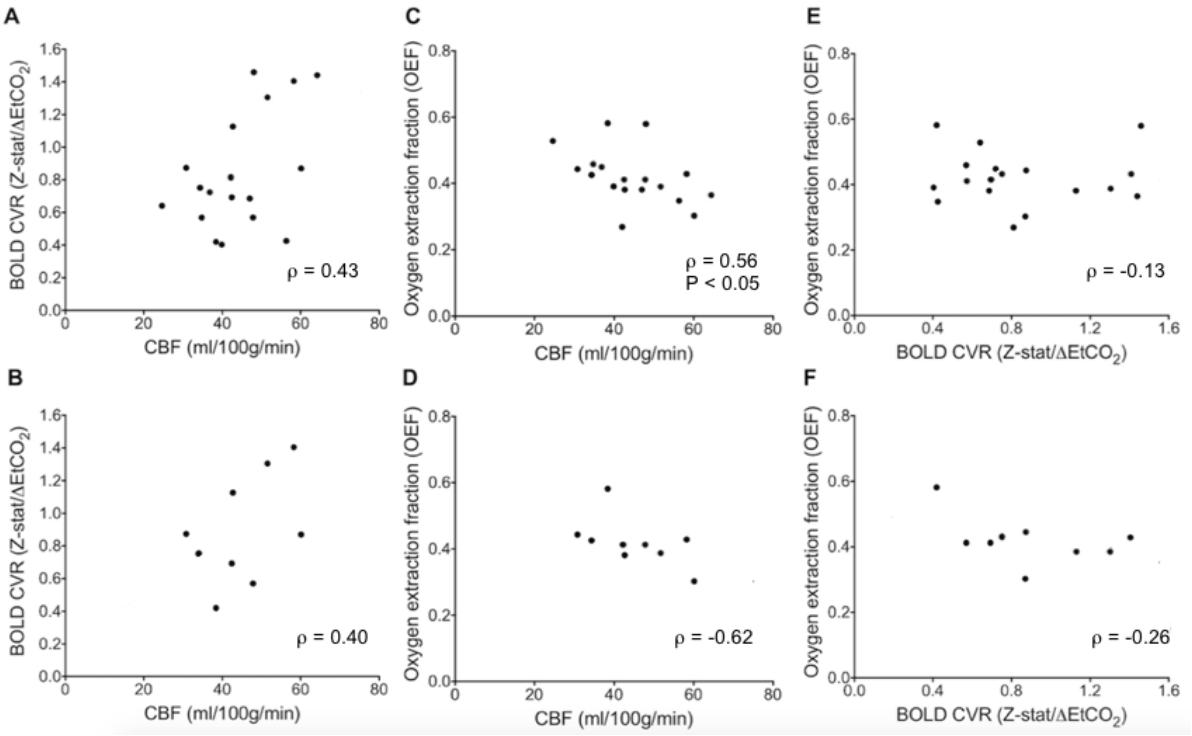

Figure 22. Relationship between CBF, CVR. and OEF in moyamoya. A Spearman's rho (ρ) was calculated to test the relationships between CBF, CVR and OEF. A sub-analysis was performed in only participants who had not undergone surgical revascularization (n=9; lower). CBF trended positively with blood oxygenation level-dependent (BOLD) hypercapnia-induced cerebrovascular reactivity measured as mean gray-matter z-statistic divided by mean change in end-tidal CO_2 ($\Delta EtCO_2$) in mmHg (Z-stat/ΔmmHg) when considering all moyamoya participants (A; ρ=0.43, *P*=0.073) and moyamoya participants who had not undergone surgical revascularization (B; ρ=0.40, *P*=0.29). The larger range in CBF was attributable to known, regional hyperintensity artifacts in ASL due to residual intravascular signal at the time of imaging. CBF was inversely correlated with OEF when considering all moyamoya participants (C; ρ=-0.56, *P*=0.016) and moyamoya participants who had not undergone surgical revascularization (D; ρ=-0.62, *P*=0.082). There was a non-significant inverse relationship between BOLD reactivity and OEF when considering all moyamoya patients (E; ρ=-0.13, *P*=0.61) and moyamoya participants who had not undergone surgical revascularization (F; ρ=-0.26, *P*=0.50). The mean change in $EtCO_2$ during the hyercapnic CVR study was 4.82±2.15 mmHg. Additionally, the BOLD signal change during hypercapnia normalized by baseline signal strongly correlated with z-statistic values (ρ=0.80, *P*<0.0001).

2.6 Discussion

We applied non-invasive CBF-weighted imaging using pCASL and whole-brain OEF imaging using TRUST in participants with moyamoya and compared results to SCA and age-matched controls. The major findings from this study are (i) OEF is globally elevated in participants with moyamoya compared to controls, a finding that was observed both in patients with and without prior surgical revascularization, and (ii) an inverse relationship between whole-brain OEF and CBF in the moyamoya participant population is robustly detectable. We additionally evaluated the relationship between CVR and OEF in moyamoya participants and found no significant relationship between our measures of CVR and OEF.

To our knowledge, this is the first time elevated whole-brain OEF has been reported in participants with moyamoya using TRUST-MRI, which can be performed in under two minutes and without exogenous contrast agents. Inter-subject variation in this parameter may provide a biomarker of hemodynamic compensation and possibly stroke risk, which is a logical extension of these initial findings. In our data set, there is a range of OEF values in the age-matched, moyamoya and SCA cohorts which is consistent with large ranges of previously reported OEF values in healthy populations and patient populations with perturbed cerebrovascular hemodynamics[65,134,149]. In ^{15}O-PET studies, OEF values are reported as high as 0.54±0.06[134] and 0.56±0.11[64] in diseased hemispheres of patients with intracranial steno-occlusion, and using global OEF studies with TRUST, values in SCA adults are reported as 0.45±0.08[133], and in patients with end-stage renal disease, values are reported as high as 0.472±0.10[135]. In healthy populations using MRI based methods, OEF measurements are reported within range of our age-matched mean[116]. These ranges across different populations highlight the possibility of using OEF as a biomarker of impairment and stroke risk, as considerable inter-subject variation exists.

Elevated whole-brain OEF in participants with moyamoya is an expected finding given that moyamoya most often affects both cerebral hemispheres, and is a progressive condition that results in widespread, albeit variable, hypoperfusion. In participants with moyamoya, compared to participants with SCA, the oxygen carrying capacity of blood is

normal, and the OEF is elevated due to decreased overall delivery of oxygenated blood to tissue (e.g., CBF).

While the moyamoya participants as a group exhibited a strong inverse relationship between CBF and OEF, group-level CBF was only marginally reduced in moyamoya subjects relative to control volunteers. There are several explanations for this finding which should be considered. First, while regional variation in CBF as visualized by pCASL, consistent with previous reports[138,150], was observed and is expected given the underlying pathology of moyamoya, intravascular signal from delayed blood arrival time to collateral vessels is likely a cause of a non-statistically significant decrease in GM CBF on average compared to age-matched controls. ASL in the setting of very delayed bolus arrival times may lead to focal hyperintensities in ASL signal. Multiple groups have studied patients with moyamoya and reported the presence of arrival time artifacts seen in cortical gray matter using ASL in this population[90,151]. Zaharchuk et al. proposed a scoring mechanism for grading collateral presence based on ASL transit time artifacts, and concluded that non-invasive ASL can even predict the presence and intensity of collateral flow on gold-standard catheter angiography. The presence of arrival time artifacts in ASL in such patients however also motivates the need for improved methods for quantifying hemodynamic and metabolic compensation as ASL may not be a quantitative marker of CBF itself in moyamoya patients with significantly delayed arrival times. An additional reason for this finding is that posterior circulation CBF in patients with moyamoya is frequently preserved and the current study focused on global hemodynamics. Therefore, while it is anticipated that ASL provides a good indicator of CBF, it additionally suffers from these contributions which may bias some of the group level findings in this study.

In addition to OEF and CBF measurements, we examined the relationship between CBF, CVR, and OEF in moyamoya participants. Impaired CVR in moyamoya patients has been reported previously and is well-known[84,152-154]. The impaired CVR could be attributable to flow-limiting stenosis at the level of large vessels, exhausted vascular reserve capacity, or collateral vessels not capable of responding to vasoactive stimuli owing to fundamental differences in the structure of these neo-angiogenic vessels relative to healthy vessels. The

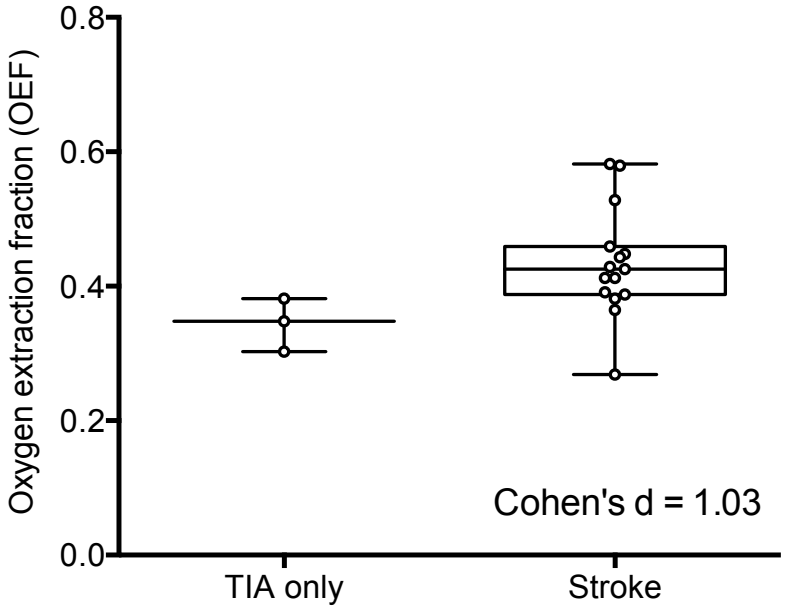

Figure 23. OEF measurements in TIA versus stroke. Categorization for stroke was defined as imaging findings consistent with infarct on FLAIR imaging > 3mm and hypointensity on T_1-weighted images. In the current sample, patients with stroke relative to TIA had a higher OEF, however additional studies with more patients are required to understand the relationship between OEF and stroke risk in this population. A Cohen's d test was used to compare the standardized difference between the average OEF values in order to determine effect size between patients with TIA only compared to stroke.

ability of neoangiogenic collateral vessels to respond to vasoactive stimuli is not well known. In one report, a positive trend between CVR and extent of collateral vessels was found, however the CVR was still reduced in hemispheres affected by steno-occlusion, compared to individuals with normal cerebral vasculature[151]. In our cohort, we found that reduced CVR was not present in volunteers with elevated OEF. As the focus of our study was on moyamoya, CVR data were not available from the participants with SCA. Autoregulatory capacity in patients with impaired cerebrovascular hemodynamics due to SCA is an area of active investigation and preliminary studies support the finding that patients with SCA have reduced CVR and that patients with the highest CBF have correspondently lowest CVR, which is likely due to exhausted autoregulatory capacity[155]. While we only provide cross-sectional results to provide motivation for increased OEF as a possible biomarker of interest in moyamoya patients, the extension of this method to longitudinally monitor individuals at risk for new or recurrent stroke could provide a simple, reproducible method for stratifying

Group	n	PLD (seconds)	τ (seconds)	PLD + τ (seconds)
SCA arm				
Controls	11	1.9	1	2.9
SCA patients	18	1.9	1	2.9
Moyamoya arm				
Control group 1	2	1.7	1.5	3.2
Control group 2	3	1.9	1.5	3.5
Control group 3	9	1.8	1.65	3.45
Control group 4	11	1.9	1	2.9
Control group 5	18	1.525	1.65	3.175
Moyamoya patients I	10	1.525	1.65	3.175
Moyamoya patients II	8	1.8	1.65	3.45

Table 5. pCASL parameters. Number of subjects (n) scanned with each protocol; pCASL parameters of post-labeling delay (PLD) and label duration (τ) listed for each cohort.

stoke risk in a diverse patient population and/or evaluating treatment success of therapies. Beyond regional CBF measurements from ASL, OEF values from TRUST provide discrete values reflective of energy homeostasis of the brain across a large dynamic range. This range of values potentially provides a gradient of disease severity, and while mean CBF could be within normal limits, elevated OEF could be a sensitive marker of disease.

Limitations of this study should also be considered. First, there is heterogeneity in the moyamoya cohort owing to the varied course of the disease, as patients have variable degrees of stenosis and time since disease onset. Therefore, extent of collateralization either by way of spontaneous formation of collaterals or surgical revascularization may affect study findings. However, the focus of this study was alternatively to understand whether elevated OEF was present at the tissue level and related to CBF and CVR. The range of patients included therefore is ideally suited to provide a range of values to investigate these relationships. Additional efforts in larger samples are required to better define normal ranges of OEF values for patients with cerebrovascular disease of varying severity and stroke history. To provide motivation for this future work, we evaluated whether patients with prior TIAs vs. overt strokes had differences in the degree of OEF elevation (Figure 23) and found evidence for higher OEF in patients with a history of overt stroke compared to a history of TIA only, however additional patients are required to confirm this finding. Second, there

were more females than males in the moyamoya participant arm, as this disease predominantly effects females. It is known that across the lifespan females have slightly elevated CBF values compared to males, however it is unlikely that this is a cause of significant bias, and we performed a sub-analysis of only female participants in the moyamoya arm and found identical trends. Third, slightly different pCASL parameters were employed during the course of this study (Table 5). Importantly, in pCASL, CBF quantification error due to post-labeling delay (PLD) variation is low when data are sampled on the decaying portion of the kinetic curve, which occurs when the labeling duration + PLD >> bolus arrival time. This time ranged from approximately 2.9s-3.4s in all data sets, and therefore this requirement is expected to be met and these errors small. A recent study compared GM CBF measures utilizing 1.5s and 2.5s PLDs with pCASL, and found no difference in GM CBF values between the two conditions (46.67 vs 46.86 ml/100g/min for 1.5s and 2.5 PLDs, respectively, in eight volunteers)[143], and our variation in PLD is approximately 1/3 of this range. Overall the PLD and label duration variation was relatively small and likely to contribute much less to CBF variation than factors related to steno-occlusion and anemia[143]. Nonetheless this was a limitation of the current study. Lastly, while we find it encouraging that TRUST-MRI is sensitive to detect whole-brain elevations of OEF in moyamoya, regional information, as is acquired using ^{15}O-PET based approaches, has the potential to provide important additional information in the context of hemispheric interval stroke risk and surgical planning for revascularization. A future direction is to evaluate regional OEF using MRI in this population, as has been recently described[156], as well as integrating new methods for high-resolution mapping of OEF[157].

2.7 Conclusions

We applied a novel MRI-based approach to quantify OEF in patients with moyamoya, and compared these findings to data from SCA patients, who have known elevated OEF, and to healthy controls. OEF was significantly elevated in moyamoya participants compared to controls, similar to participants with SCA and CBF was inversely correlated with OEF in moyamoya participants. Elevated OEF was only weakly related to reductions in CVR,

consistent with basal CBF level, rather than vascular reserve capacity, being most closely associated with OEF. These results (i) are consistent with non-invasive MRI being able to quickly detect elevated OEF in multiple cases of reduced oxygen delivery to tissue, (ii) provide insights regarding differing pathological hemodynamic compensation mechanisms, and (iii) suggest that globally elevated OEF in moyamoya is present and inter-subject variation in this parameter could be indicative of tissue-level impairment and elevated stroke risk.

CHAPTER 3

COMPLIANCE CHANGES FOLLOWING REVASCULARIZATION IN MOYAMOYA

3.1 Purpose

To evaluate improvement in cerebrovascular compliance measures following surgical intervention in moyamoya, and compare these findings to gold-standard digital subtraction angiography (DSA). Currently, invasive methods are used to evaluate surgical outcome and furthermore, these methods are not suitable for continued surveillance of tissue health. Therefore, the goal of our work was to directly compare outcomes as determined by DSA, which requires ionizing radiation and arterial access, with non-invasive cerebrovascular compliance imaging. We focused on patients with moyamoya due to surgical revascularization being standard-of-care at specialized centers. However, as new approaches emerge for treating other causes of intracranial disease, the methods described in this chapter could provide important information regarding effect of intervention on tissue health.

3.2 Summary

Surgical revascularization is often performed in patients with moyamoya, however non-invasive methods for evaluating efficacy are not well-developed. The gold-standard is DSA, however this approach requires ionizing radiation and is not ideally suited for routine surveillance and assessment of tissue function. The goal of this work therefore is to understand whether traditional or novel vascular compliance measures, obtained non-invasively using magnetic resonance imaging (MRI), provide a surrogate of revascularization success by comparing these measures directly with DSA before and after surgical revascularization. Twenty surgical hemispheres in moyamoya patients (mean age = 38 ± 14 years [range = 16-59 years]) with DSA and MRI performed before and after revascularization were evaluated. Cerebrovascular reactivity (CVR)-weighted images were acquired using hypercapnic 3-Tesla (T) gradient echo blood oxygenation level-dependent

MRI. Standard and novel analysis algorithms were applied to (i) quantify relative cerebrovascular reactivity ($rCVR_{RAW}$), and decompose this response into (ii) relative maximum CVR ($rCVR_{MAX}$) and (iii) time for parenchyma to respond maximally to the stimulus (CVR_{DELAY}). Measures between time points in patients with good and poor surgical outcomes based on collateral formation on DSA were compared (significance: $P<0.05$; Wilcoxon signed-rank test). Increases in $rCVR_{RAW}$ ($P=0.010$) and decreases in CVR_{DELAY} ($P=0.001$) were observed in hemispheres with good revascularization; no difference was found in hemispheres with poor revascularization. No significant change in $rCVR_{MAX}$ was observed in either group, or between any of the MRI measures before versus after surgery in the contralateral hemisphere. Increases in vascular compliance measures post-surgery, primarily attributed to reductions in vascular response time, are concurrent with revascularization success defined from DSA; these metrics may be useful for longitudinal monitoring of surgical success.

3.3 Introduction

There is currently no treatment that is known to halt or reverse moyamoya, and rather treatment focuses on improving cerebral blood flow (CBF; ml/100g tissue/min) through surgical revascularization[158]. Indirect surgical revascularization is being performed more frequently despite a lack of clinical trial evidence supporting efficacy. One limitation to performing formal efficacy trials is that surgical success is most commonly evaluated qualitatively through changes in symptomatology or collateral visualization on DSA. While DSA is useful for anatomical visualization of the collateral network, it provides limited spatial information (from large vessels only) and is insensitive to tissue-level changes in perfusion. Additionally, DSA requires ionizing radiation and carries procedural risks, and thus may not be performed for continued surveillance. As such, the mechanism and temporal course of how revascularization surgery impacts parenchyma function is not well characterized; alternative imaging approaches that can provide comparable or additional information to DSA with fewer risks would be helpful.

One promising approach is hypercapnic CVR mapping[82,159-162]. The premise for this

approach is that reductions in cerebral perfusion pressure secondary to arterial steno-occlusion may be wholly or partially compensated for at the tissue-level by autoregulatory increases in cerebral blood volume (CBV; ml blood/100g tissue). By challenging vessels with a vasodilatory stimulus (e.g., acetazolamide, breath hold, or mild hypercapnia) it is possible to evaluate the corresponding hyperemic response, which will be reduced in parenchyma operating at or near autoregulatory reserve capacity. This approach has been applied in SPECT[163-165] and MRI-CBF[116,150,166-168] studies, however these methods suffer from the need for exogenous contrast agents, ionizing radiation, or low sensitivity to delayed blood-arrival time.

Noninvasive hypercapnic blood oxygenation level-dependent (BOLD)-MRI, which provides a qualitative surrogate of CBF and CBV changes can be applied to record changes in tissue-level hemodynamics over a longer blood arrival and vascular response time. It has recently been shown that neoangiogenic collaterals formed due to cerebrovascular disease have distinct vasoactive properties relative to healthy vessels[169]. Additionally, recent preclinical optical imaging work has revealed that endothelial disruption significantly attenuates and the functional hyperemia response[96]. These findings suggest that not only the magnitude of the change in parenchymal blood volume and flow, commonly referred to as CVR, but also the time for parenchymal vessels to respond maximally to vasoactive stimuli or progressive reductions in cerebral perfusion pressure, may represent distinct features of parenchymal health. Both constructs can be evaluated non-invasively[99] and may provide information on revascularization success.

Importantly, there is a clinical need for non-invasive methods to monitor surgical outcomes in patients with moyamoya, but first these methods must be compared directly with accepted angiographic techniques. Here, we evaluated moyamoya patients using gold-standard DSA and hypercapnic BOLD-MRI before and after surgical revascularization. Our first objective was to understand the relationship between collateral vessel formation from DSA and the change in MRI-measured CVR using a conventional analysis. A secondary objective was to apply a more novel time-delay analysis to the MRI data to understand whether (i) the magnitude of the vascular response, or (ii) the vascular response time, provided the best revascularization response indicator. The goal was to inform on whether

non-invasive MRI methods provide similar information to DSA in patients with moyamoya undergoing surgical revascularization and thus provide a non-invasive surrogate for evaluating surgical outcomes.

3.4 Materials and Methods

Ethical considerations and participants

The study was approved by the institutional review board (IRB) at Vanderbilt University Medical Center. Patients presenting to the clinical neurosurgery services between March 2011 and March 2016 with suspected moyamoya underwent a protocol of DSA and BOLD-MRI, and any patient with symptomatic moyamoya underwent revascularization. Decision regarding direct versus indirect revascularization was made based on the caliber of the superficial temporal artery (STA). Revascularized patients underwent post-operative DSA and repeat BOLD-MRI at approximately 12 moths following surgery. 68 patients with a diagnosis of moyamoya from DSA were identified during this time period of which 66 patients provided consent to participate in research. The 66 patients were then evaluated for the following inclusion criteria for this cohort analysis: (i) Revascularization of one or both hemispheres; (ii) pre- and post-surgical DSA; (iii) pre- and post-surgical BOLD-MRI. Healthy adults (n=9) also provided consent and were enrolled for reference evaluation of vascular compliance measures.

Surgical revascularization

All surgical revascularizations were indirect, with the exception of one where the patient presented with multiple crescendo-type ischemic symptoms and the STA caliber was large and therefore a direct STA to middle cerebral artery (MCA) bypass was performed. The indirect procedures were encephaloduroarteriosynangiosis (EDAS) type, in which the STA is sutured either directly to the cortex or dura, and one procedure was encephalomyosynangiosis (EMS), which is similar to EDAS, however instead of dissection of the STA, the temporalis muscle with associated vasculature is dissected and placed onto the surface of the brain. EMS was performed in this patient due to low STA

caliber, but sufficient temporalis graft muscle. Of note, as the purpose of this study was to evaluate consistency between DSA and MRI, rather than how the type of surgical revascularization impacted collateral formation, all patients were included.

Image acquisition

MRI was performed on a 3T Achieva scanner (Philips Healthcare, Best, The Netherlands).

(i) Digital subtraction angiography. Moyamoya participants underwent diagnostic DSA with catheterization and injection with intra-arterial contrast of bilateral common carotid arteries (CCA), external carotid arteries (ECA) when feasible, ICAs when feasible, and vertebral arteries using an Allura Xper (Philips Healthcare, Best, The Netherlands) biplane neuro X-ray system.

(ii) Anatomical imaging. T_2-weighted FLuid-Attenuated-Inversion-Recovery (FLAIR; spatial resolution=0.4x0.3x5.0 mm^3; repetition time (TR)/ echo time (TE)/ inversion time (TI)=11000/120/2800 ms), 3D T_1-weighted (spatial resolution=1.0x1.0x1.0 mm^3; TR/TE=9.0/4.6 ms), and diffusion-weighted (spatial resolution=0.9x0.9x5.0 mm^3; TR/TE 9636.6/92.6, b=0 and b=1000s/mm^2) imaging was performed for infarct determination.

(iii) Cerebrovascular reactivity imaging. Participants were fitted with a nasal cannula for end tidal CO_2 ($EtCO_2$) monitoring and a non-rebreathing facemask for administration of medical grade room air (21% O_2, 79% N_2) and carbogen (5% CO_2, 95% O_2). Medical grade carbogen, which is an FDA-approved drug, rather than hypercapnic normoxia (5% CO_2/95% air), was used as mandated by our IRB. This stimulus has been shown to correlate with hypercapnic normoxic stimuli and to provide sensitivity to impaired reactivity in intracranial stenosis[84,170]. We additionally evaluated both stimuli in healthy controls using identical block paradigms to understand effect on output metrics. The paradigm consisted of 90s of room air, followed by two 3 minute blocks of carbogen interleaved with 3 minute blocks of room air. Blood pressure, $EtCO_2$ and oxygen saturation were monitored by a respiratory therapist. Whole-brain (slices=31) single-shot gradient echo echo-planar-imaging (EPI) BOLD images were acquired with spatial resolution=3x3x3.5 mm^3 and TE=35 ms.

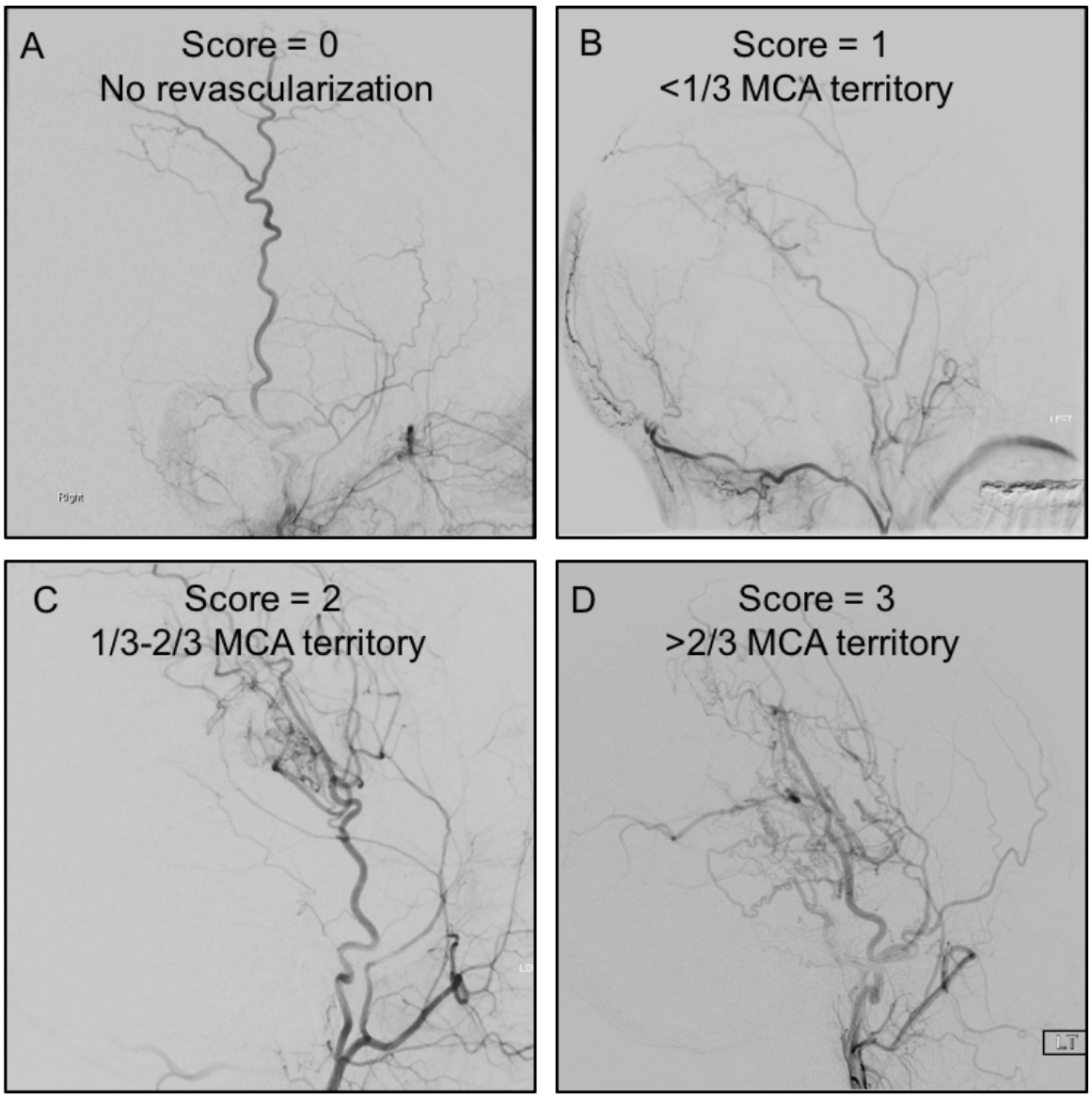

Figure 24. Revascularization scoring system. Lateral projections of digital subtraction angiography (DSA) images were used to assess coverage of middle cerebral artery (MCA) territory. The four categories used for classification were 0: no revascularization (A), 1: <1/3 of the MCA territory (B), 2: 1/3 to 2/3 of MCA territory (C), and 3: >2/3 of the MCA territory.

Image analysis

(i) Digital subtraction angiography. Hemispheric modified Suzuki Score (mSS) was scored by a board-certified neuroradiologist and neurosurgeon. For mSS grading, the range is 0-4, with 0 representing no steno-occlusive changes and 4 representing complete occlusion of

both proximal anterior and middle cerebral arteries[18,145]. Revascularization success was determined by DSA based on amount of MCA territory revascularized using a grading system from 0 to 3, similar to Matsushima et al.[171] and described in Figure 24. A neurosurgeon and neuroradiologist were blinded to results of cerebrovascular imaging while performed scoring from DSA.

(ii) Anatomical imaging A neuroradiologist evaluated images for presence and size of chronic infarcts (defined as FLAIR hyperintense lesions ≥ 3 mm with T_1 hypointensity approaching CSF signal). Acute infarcts were assessed by the same neuroradiologist using diffusion-weighted imaging and standard clinical criteria[172].

(iii) Cerebrovascular reactivity imaging. Data were pre-processed using FSL software[146] to correct for motion and baseline drift. The vascular compliance measures were generated using two different approaches. First, conventional CVR maps were generated based on the calculated z-score using a standard rectangular regressor that corresponded to the gas stimulus paradigm. The z-scores were then normalized by dividing by the mean z-score in the area perfused by the posterior circulation to allow for group-level analysis of changes in relative CVR ($rCVR_{RAW}$). Here the assumption, which is not necessarily true and investigated here, is that all voxels increase at a similar time and the only difference contributing to the z-score is due to the magnitude of the BOLD response.

Next, we performed time-delay analysis[99] to understand the separate contribution from the vessel response times and the magnitude of the response. Here, the above regressor was progressed in time and we recorded the time at which maximum correlation occurs (CVR_{DELAY}) between BOLD signal from each voxel in a given time series compared to the reference regressor, and the resultant z-score was normalized by the reactivity in the posterior circulation ($rCVR_{MAX}$). This time-delay analysis allowed for decomposition of the CVR response into the time required for the vessels to respond maximally to the stimulus as well as a statistical measure of this maximum response, which is very similar to the signal change. Note that vascular compliance times may not be temporally correlated with $EtCO_2$ changes due to differences in smooth muscle and endothelial rigidity, and this secondary

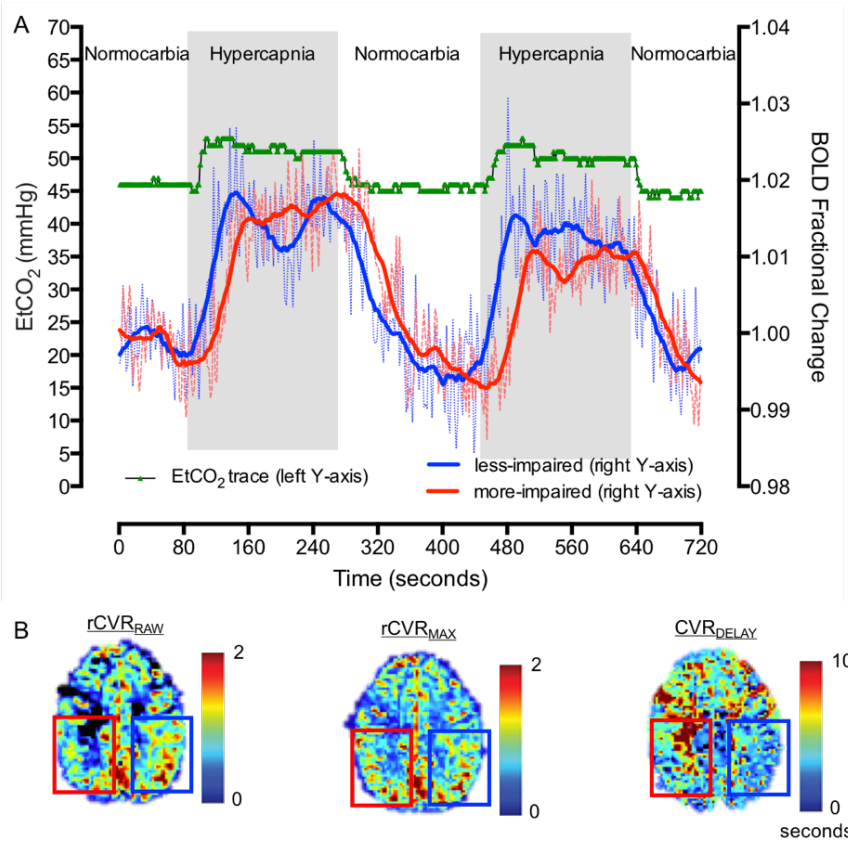

Figure 25. Analysis of the BOLD response**.** Hypercapnia-induced vasodilation results in increased fractional BOLD signal change and contemporaneous increase in end-tidal CO_2 ($EtCO_2$) (left). A more-impaired region (red time course) and a less-impaired region (blue time course) in a 44 year-old female participant with bilateral (mSS on right = 2, mSS on left =1) moyamoya disease are shown. The red time course demonstrates an increased CVR_{DELAY} relative to the start of the hypercapnia. Maps of vascular compliance measures are shown on the right. Conventional relative CVR ($rCVR_{RAW}$) maps are generated based on the calculated z-score from a rectangular regressor and normalized by uninvolved posterior circulation values. CVR_{DELAY} and relative CVR_{MAX} ($rCVR_{MAX}$) measures were determined using a time-delay analysis to find the time at which maximum correlation occurs between BOLD signal from each voxel compared to the reference regressor, and the resultant z-score. This analysis allows for calculation of voxel-wise maximum z-scores, even in the setting of delayed reactivity timing. In this subject, the more-impaired region has decreased $rCVR_{RAW}$ and increased CVR_{DELAY} measures compared to the less-impaired region.

analysis provides a distinct construct from using the $EtCO_2$ trace or gas paradigm as the regressor, as is most common. A BOLD time course and combined $rCVR_{RAW}$, $rCVR_{MAX}$ and CVR_{DELAY} maps are shown in Figure 25. Data were registered to a 2 mm Montreal Neurological Institute (MNI) T_1-weighted standard space atlas[147] and mean $rCVR_{RAW}$,

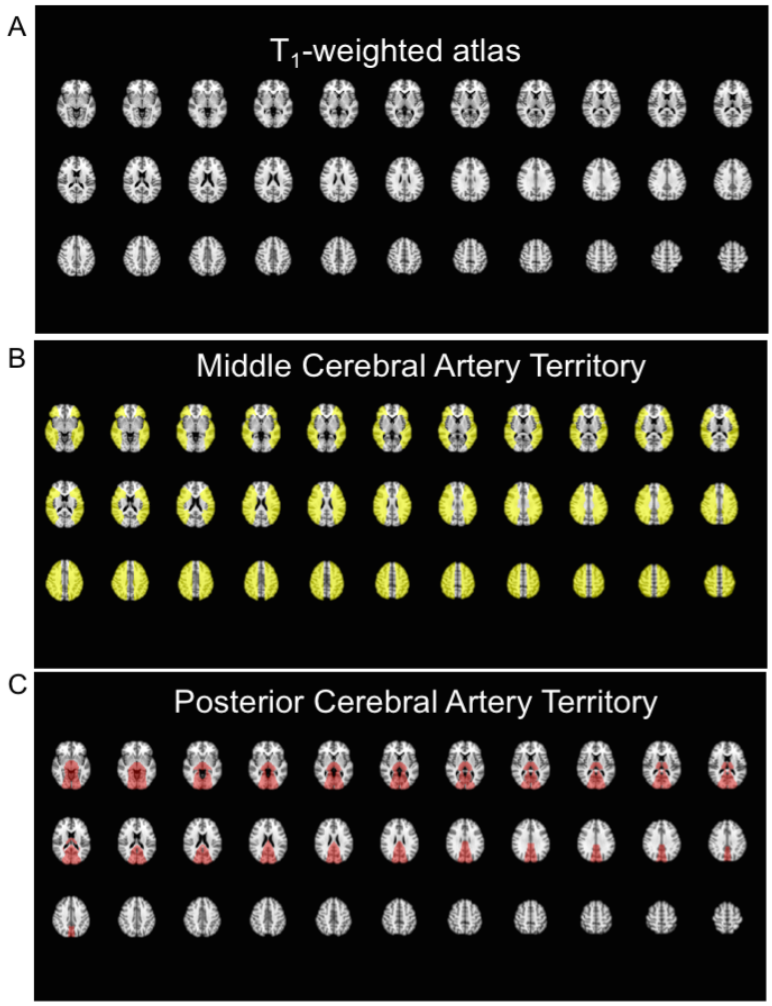

Figure 26. ROIs used for compliance measures. A T_1-weighted atlas is shown in (A). Middle cerebral artery (MCA) and posterior cerebral artery territory were determined by including all tissue in the area of corresponding MCA Alberta Stroke Programme early CT score regions. Axial slices with overlaid territory map for the MCA and posterior cerebral artery territory are shown in (B) and (C), respectively.

$rCVR_{MAX}$ and CVR_{DELAY} values were calculated in the MCA territory of the operative hemisphere pre- and post-revascularization (Figure 26). In one case there was significant unilateral posterior disease, and the contralateral posterior territory was used for normalization of CVR_{RAW} and $CVR_{MAX.}$ Non-operative hemispheres and control subjects were also evaluated in an identical fashion. MCA territory values were the observables preserved for hypothesis testing.

Statistical concerns and hypothesis testing

The primary hypothesis was that participants with successful revascularization, defined as neovascularization on DSA that covers more than 1/3 of the MCA territory, will have increased post-operative $rCVR_{RAW}$ values. A secondary aim was to evaluate the effect of surgical revascularization on novel vascular compliance metrics, $rCVR_{MAX}$ and $rCVR_{DELAY}$. Descriptive statistics, including means, standard deviations, and ranges of continuous parameters were recorded. To test both study objectives, patients were divided into those with >1/3 MCA territory revascularized vs. those with <1/3 MCA territory revascularized, and a two-sided Wilcoxon signed-rank test was used to compare separately $rCVR_{RAW}$, $rCVR_{MAX}$, and CVR_{DELAY} (both in operative and non-operative hemispheres) for pre-surgical and post-surgical time points. Two-tailed P-value<0.05 was required for significance.

3.5 Results

Demographics

Table 6 summarizes baseline demographic information of the moyamoya cohort. 26 brain hemispheres from 17 participants met inclusion criteria. Three patients were excluded due to technical issues: one patient due to suboptimal $EtCO_2$ changes (<3 mmHg) from the gas delivery, likely due to mask motion, one patient due to an implanted screw that caused a large artifact, and one patient due to claustrophobia and inability to complete the scan. Therefore, 20 total operative hemispheres from 14 participants were included. BOLD-MRI was evaluated at 13.9 ± 6.6 months post-revascularization, collateralization was evaluated with DSA at 12.8 ± 4.8 months post-revascularization. Table 7 summarizes cerebrovascular compliance measures. Mean change in $EtCO_2$ in response was 6.0 ± 1.6 mmHg, and there was no significant difference in $EtCO_2$ change when comparing pre-surgical scans to post-surgical scans (P=0.27). A significant correlation between all vascular compliance measures using hypercapnic normoxia and hypercapnic hyperoxia (e.g., carbogen) in control subjects age-matched within one decade of life (age=29±4.1 years) to moyamoya participants was

Parameters	Moyamoya (n=14)
Age (years, mean ± st. dev.) [range]	44.8 ± 21.7
Biological Sex (% female)	0
Race (% Asian/White/Black)	71
Antiplatelet (% on therapy)	97.1 ± 1.2
Cardiovascular Risk Factors	63.7 ± 6.0
Diabetes Mellitus (%)	1.62
Smoking (%)	68.0 ± 1.2.2
Modified Suzuki Score Right (mean ± std. dev.)	0.343 ± 0.061
Modified Suzuki Score Left (mean ± std. dev.)	40.2 ± 10.3
Idiopathic Moyamoya (%)	49.2 ± 12.5
Change in End Tidal CO_2 (mmHg, mean ± std. dev.)	NA
Infarct at presentation (%)	NA
New infarct at follow-up (%)	0

Table 6. Summary of study participants and vascular compliance measures

observed (Figure 27), consistent with carbogen and hypercapnic normoxic stimuli eliciting correlated BOLD responses. Additionally, while it is well known that the magnitude of the BOLD response to carbogen exceeds that in response to hypercapnic normoxia, the time for vessels to respond to both stimuli is not significantly different (Figure 27D).

Revascularization response

Revascularization success in the included hemispheres using the DSA grading system of 0/1/2/3 yielded categorization of 1/4/12/3 hemispheres, respectively.

Vascular compliance measures in control compared to moyamoya subjects

Group-level composite maps of vascular compliance measures in control participants and pre-surgical moyamoya participants is shown shown in Figure 28. Noted is bilaterally decreased $rCVR_{RAW}$, $rCVR_{MAX}$ and bilaterally increased CVR_{DELAY}. Consistent with moyamoya pathology, $rCVR_{RAW}$ and $rCVR_{MAX}$ are higher posteriorly compared to middle and anterior cerebral artery territory values.

	>1/3 MCA territory revascularization (n=14 hemispheres)		<1/3 MCA territory revascularization (n =5 hemispheres)	
Vascular compliance measures	Pre-surgery	Post-surgery	Pre-surgery	Post-surgery
$rCVR_{RAW}$ (mean ± std. dev.) [range]	0.46 ± 0.26 [-0.19-0.79]	0.63 ± 0.12 [0.40-0.83]	0.59 ± 0.20 [0.38-0.88]	0.58 ± 0.24 [0.31-0.85]
$rCVR_{MAX}$ (mean ± std. dev.) [range]	0.83 ± 0.07 [0.71-0.95]	0.86 ± 0.06 [0.75-0.95]	0.88 ± 0.12 [0.67-0.96]	0.86 ± 0.12 [0.72-0.98]
CVR_{DELAY} (mean ± std. dev.) [range]	57.9 ± 13.6 [34.7 – 83.7] sec	49.0 ± 8.2 [33.7- 66.6] sec	50.4 ± 6.0 [45.6 – 60.7] sec	52.9 ± 14.3 [37.7- 72.4] sec

Table 7. Summary of cerebrovascular compliance measures

Vascular compliance measures pre- and post-revascularization

Group-level vascular compliance measures in operative hemispheres are shown in Table 7 organized by patients with >1/3 MCA territory revascularized (n=15 hemispheres) and <1/3 MCA territory revascularized (n=5 hemispheres). Consistent with the primary hypothesis, $rCVR_{RAW}$ increases following surgical revascularization in the cohort with >1/3 MCA territory neovascularization (pre-surgery $rCVR_{RAW}$=0.46±0.26; post-surgery $rCVR_{RAW}$=0.63±0.12; P=0.010).

In participants with <1/3 MCA territory revascularized, there was no significant change in $rCVR_{RAW}$ (pre-revascularization $rCVR_{RAW}$=0.59±0.20; post-revascularization $rCVR_{RAW}$=0.58±0.24; P>0.50). There was no significant change in $rCVR_{MAX}$ in either group. In participants with >1/3 MCA territory revascularized, a significant decrease in CVR_{DELAY} was found following revascularization (pre-revascularization CVR_{DELAY}= 57.9±13.6s; post-revascularization CVR_{DELAY}=49.0±8.2s; P=0.001).

In participants with <1/3 MCA territory revascularized, no significant change in CVR_{DELAY} was found (pre-revascularization CVR_{DELAY}=50.4±6.0s; post-revascularization CVR_{DELAY}=52.9±14.3s; P>0.50). Therefore, when considering the operative hemisphere in participants who had >1/3 MCA territory revascularized, both $rCVR_{RAW}$ and CVR_{DELAY} were discriminatory in determining surgical outcome. No significant difference in any vascular compliance measure was observed in the non-revascularized hemispheres. Figure 29 shows case examples. Graphs of each pre- and post-surgical vascular compliance measure

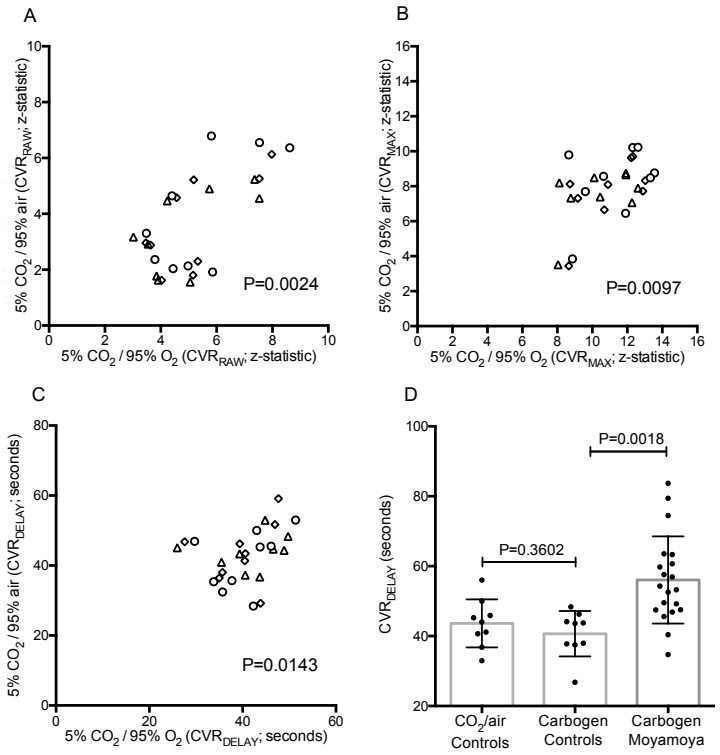

Figure 27. Comparison of carbogen and hypercapnic normoxia. Vascular compliance measures were compared between carbogen (5% CO_2 / 95% O_2) versus hypercapnic normoxia (5% CO_2 / 95% air) mixture in controls. Cerebrovascular reactivity measures (CVR_{RAW} and CVR_{MAX}) in addition to CVR_{DELAY} measures were evaluated in healthy control subjects (n=9) in the left middle cerebral artery (MCA) territory (diamond), right MCA territory (triangle) and posterior circulation (circle). Region-of-interest correlations were evaluated between the vascular stimuli; to allow for comparison across all voxels, no normalization by values in posterior circulation was performed. A significant correlation was observed between carbogen and hypercapnic normoxia in CVR_{RAW} (ρ=0.53, P=0.0024; panel A), CVR_{MAX} (ρ=0.45, P=0.0097; panel B), and CVR_{DELAY} (ρ=0.42, P=0.0143; panel C). Panel D demonstrates a non-significant difference between CVR_{DELAY} values between carbogen and hypercapnic normoxia stimulus. As expected, CVR_{DELAY} values in moyamoya participants were significantly elevated compared to controls.

are shown in Figure 30. Group-level maps of vascular compliance measures are shown in Figure 31. Hemispheres with >1/3 MCA territory revascularization were included in Figure 31A, and non-operative hemispheres are shown in Figure 31B. $rCVR_{RAW}$ values improve following robust revascularization, and CVR_{DELAY} values decrease. $rCVR_{MAX}$ values do not significantly change. These trends are not observed in non-operative hemispheres.

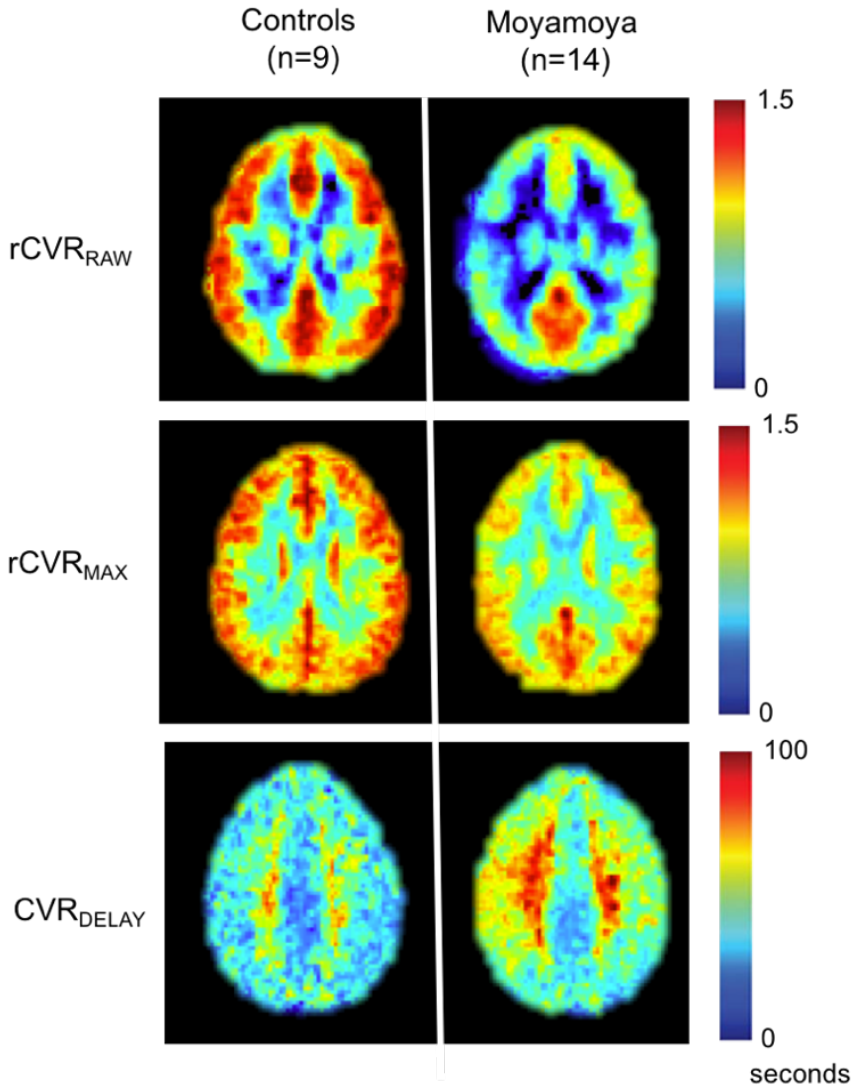

Figure 28. Group-level maps of vascular compliance measures in control and moyamoya participants. Pre-surgical imaging was evaluated in the moyamoya group. Single axial views of each group-averaged vascular compliance measure are shown. Noted is bilaterally decreased $rCVR_{RAW}$, $rCVR_{MAX}$ and bilaterally increased CVR_{DELAY}. Consistent with moyamoya pathology, $rCVR_{RAW}$ and $rCVR_{MAX}$ are increased posteriorly compared to middle and anterior cerebral artery territories. Vessel reactivity time as reflected in the CVR_{DELAY} maps is longer in the deep white matter compared to cortical gray matter in both the control and moyamoya participant groups.

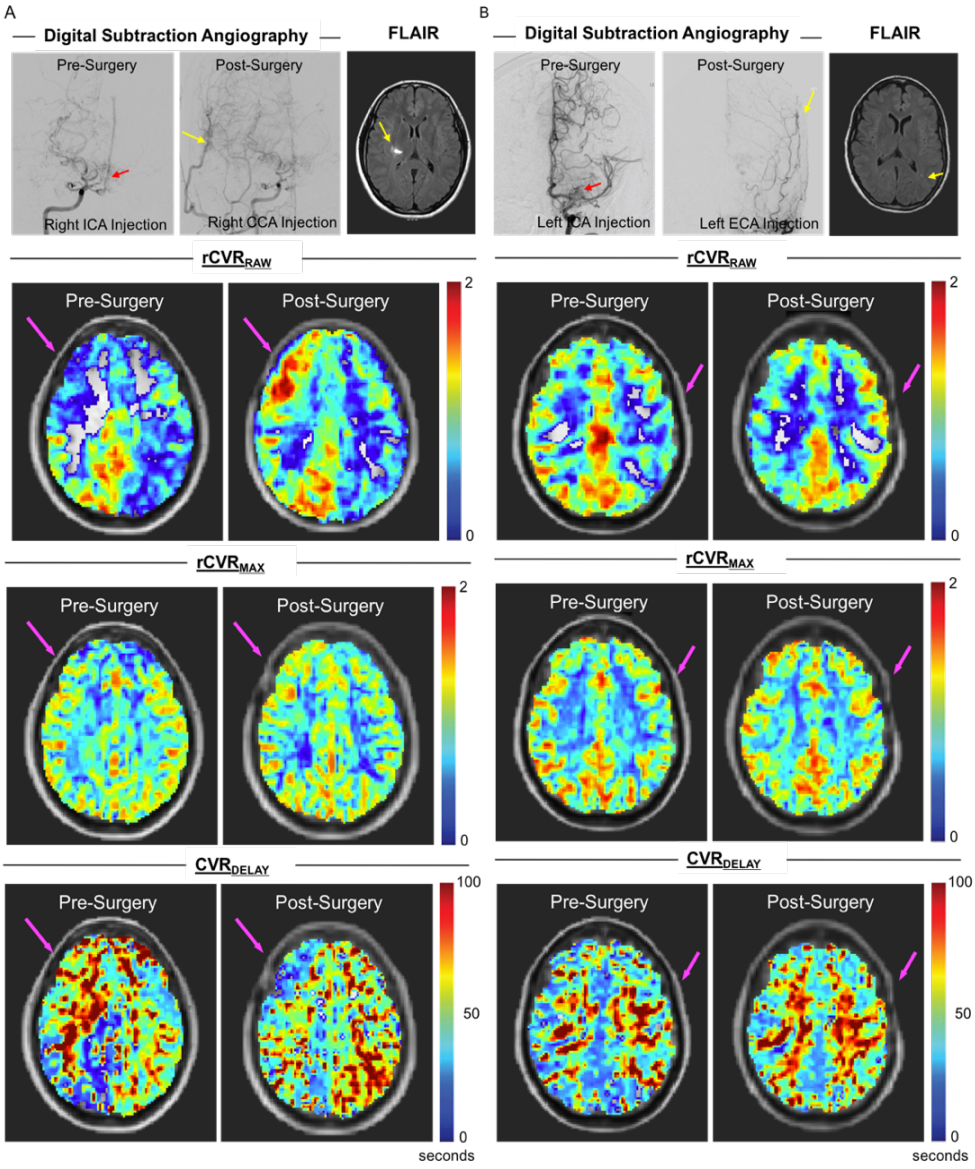

Figure 29. DSA and vascular compliance imaging pre-and post- revascularization. (A) A participant with robust post-surgical revascularization of the right middle cerebral artery (MCA) territory; shown are anterior-posterior projections of internal carotid artery (ICA), common carotid artery (CCA) and external carotid artery (ECA) injections. The red arrow denotes moyamoya collaterals in the pre-surgical image, and the yellow arrow shows the region of neovascularization. This patient presented with an infarct in the right hemisphere resulting in a hyperintense signal on FLAIR. Additional panels in (A) show correspondent BOLD-derived vascular compliance measures. Improvement (increase) in $rCVR_{RAW}$, modest improvement in $rCVR_{MAX}$, and improvement (decrease) in CVR_{DELAY} are observed post-surgery in the right hemisphere (magenta arrows denote operative hemisphere). In contrast, a participant with minimal post-surgical neovascularization following left-sided surgery is shown in (B). This patient presented with a left sided infarct which appears as a punctate FLAIR hyperintense lesion in the periventricular white matter. Corresponding BOLD-derived vascular compliance measures show decrease in left-sided $rCVR_{RAW}$, stable $rCVR_{MAX}$, and increase in CVR_{DELAY}.

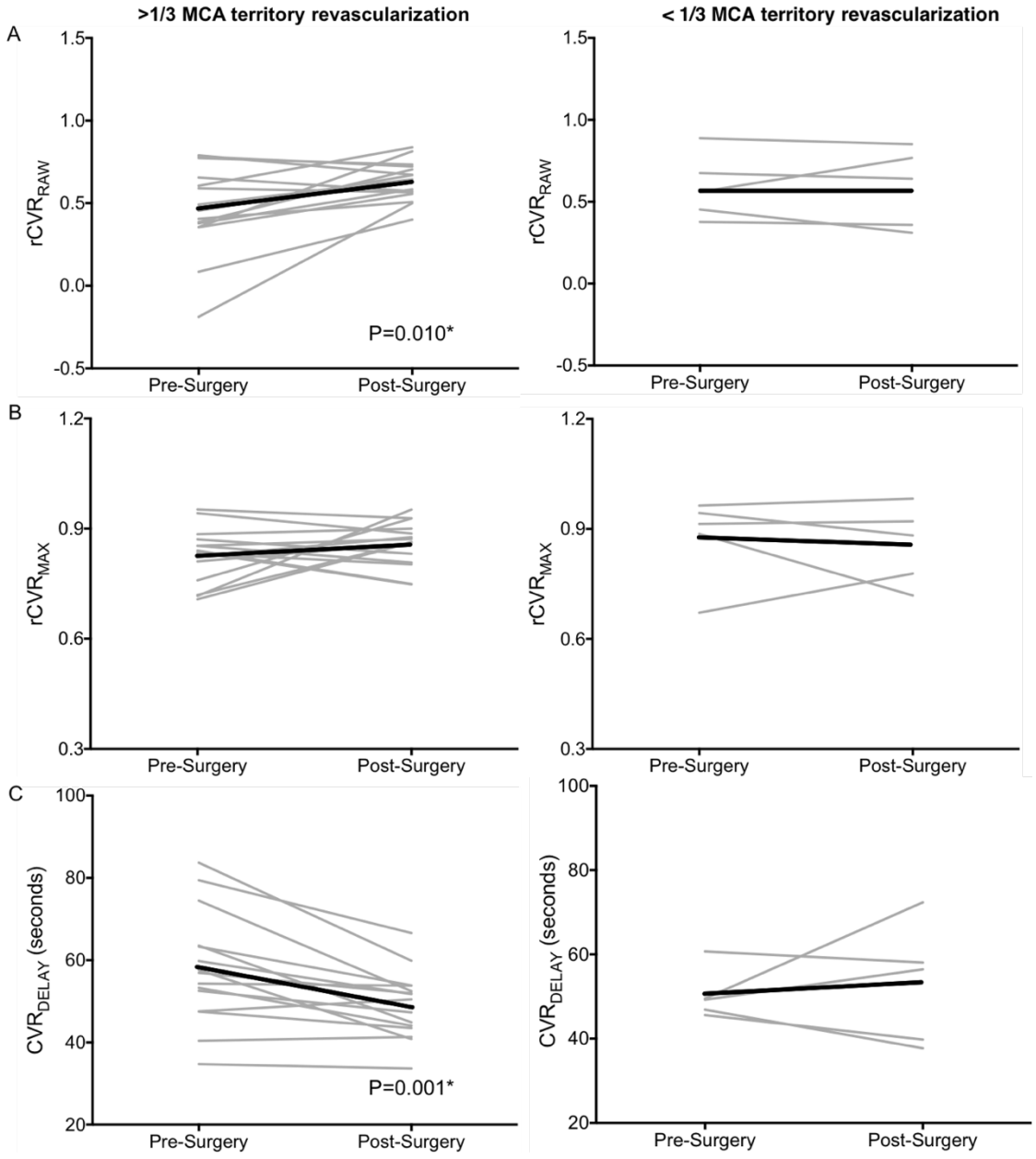

Figure 30. Group-level results of vascular compliance measures. A two-sided Wilcoxon signed-rank test was performed to test the primary hypothesis that improvements in $rCVR_{RAW}$ will be present and the secondary aim to evaluate $rCVR_{MAX}$ and CVR_{DELAY} in patients following surgery. (A) An increase in $rCVR_{RAW}$ in participants with >1/3 MCA territory revascularization (P=0.010) and no significant change in $rCVR_{RAW}$ in participants with <1/3 MCA territory revascularization. (B) No significant change in $rCVR_{MAX}$ in participants classified in either group. (C) A decrease in CVR_{DELAY} in patients with >1/3 MCA territory revascularization (P=0.001) and no significant change in CVR_{DELAY} in participants with <1/3 MCA territory revascularization.

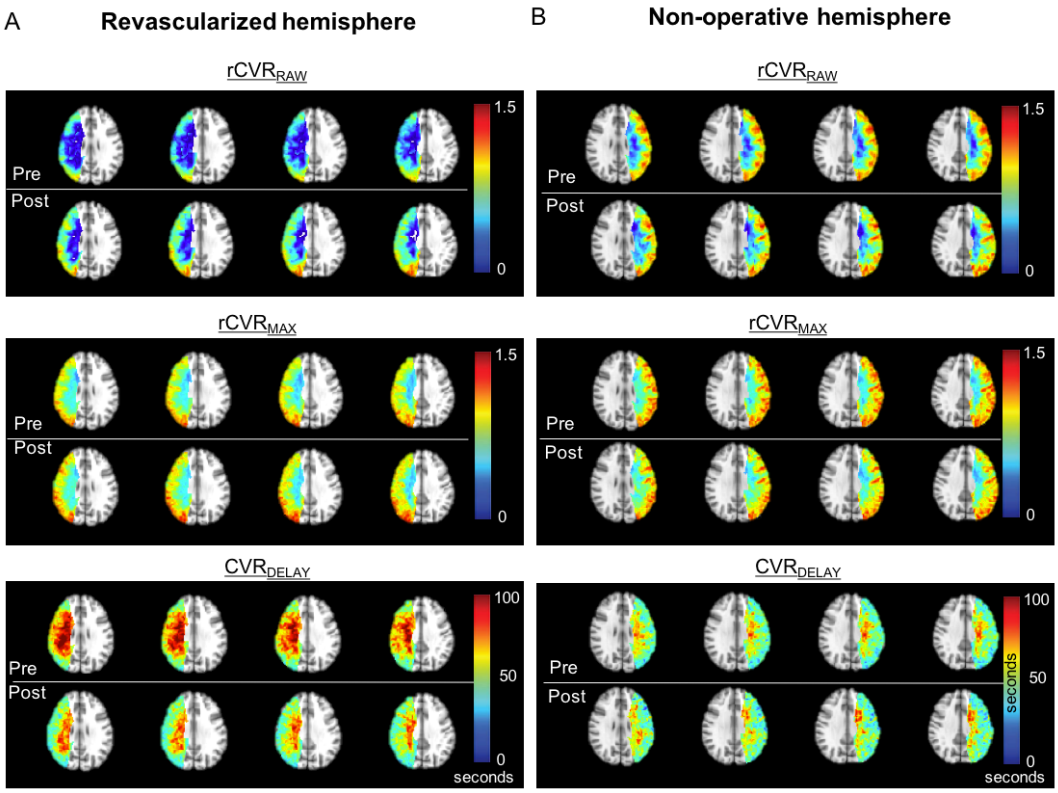

Figure 31. Vascular compliance measures in operative and non-operative hemispheres. Maps of revascularized hemispheres (n=15 with revascularization >1/3 MCA territory) and maps of non-operative hemispheres (n=8 hemispheres). Improved $rCVR_{RAW}$, small increase in $rCVR_{MAX}$, and decrease in CVR_{DELAY} are observed following revascularization (A). In non-operative hemispheres, no significant changes in $rCVR_{RAW}$, $rCVR_{MAX}$, or CVR_{DELAY} are observed (B).

3.6 Discussion

While elegant studies of CVR changes in response to surgical revascularization in moyamoya have been performed, these changes have never been compared directly and longitudinally with collateral changes on gold-standard DSA[173-175]. We applied traditional CVR and novel time-delay BOLD image processing in patients with moyamoya before and after surgical revascularization for the first time to determine vascular compliance measures that were predictive of successful neovascularization. Revascularization response as determined by DSA is similarly reflected in increased CVR as determined by traditional

analysis and decreased reactivity time, as determined by time-delay approach in hemispheres with a revascularization response of >1/3 MCA territory. In participants with <1/3 MCA territory revascularization and in non-operative hemispheres, no significant change in any vascular compliance measure was observed.

Time-delay processing of BOLD may provide additional information beyond more qualitative measures such as z-statistic or signal change. Our findings are consistent with prior reports that traditional CVR analysis is sensitive to surgical response to revascularization[173], but we extend this analysis to include decomposed BOLD signal parameters, which we hypothesized contribute to the changes in CVR. In the group of participants with >1/3 MCA territory revascularization, the significant decrease in CVR_{DELAY} coupled with no significant change in $rCVR_{MAX}$ can potentially indicate that the absolute vascular compliance (ability to accommodate increases in CBF in response to hypercapnia) in territories fed by large vessels with arterial vasculopathy is often not exhausted, but rather that reactivity time-delay may be prolonged and may play a large role in apparent decreased reactivity values as evaluated by traditional analysis. This is a relatively novel finding, as most CVR-MRI approaches apply either arterial spin labeling (ASL)-MRI, which has lower temporal resolution (4-8s) and is largely insensitive to very delayed blood arrival times, or BOLD-MRI that is performed for much shorter stimulus durations and uses only the gas paradigm or $EtCO_2$ as a regressor. Of note, CVR_{DELAY} is a measure that is absolute, and reported in seconds (relative to stimulus start, which is the same between subjects); other similar measures of reactivity delay such as $CVR_{lagtime}$ have been described, but are relative to the hemodynamic response function, which is unique to each participant in each scan session[99,176].

A prior study evaluating spontaneous collateral development shows that collaterals in patients with cerebrovascular disease have fundamentally different hemodynamic properties when compared to healthy vessels as evaluated by DSA, BOLD and ASL methods [169]. Here, we provide the first evaluation into the functional underpinnings of newly formed vessels by performing traditional and time-delay CVR analysis. Upon new vessel formation, it is possible that the newly formed smooth muscle lined arterioles are capable of a more rapid response to vascular stimulus which results in increased traditional CVR measurements

and decreased reactivity delay. Of note, reactivity delay values greatly exceed arterial circulation time (ACT) even in patients with steno-occlusion and delayed filling due to collateral pathways (wherein ACT ~3 seconds)[168]. Using time-delay regression, we report a metric indicative of the ACT and microvascular dilation time (>20 seconds in some vessels). Additionally in support of neovascularization contributing to decreased time-delay and increased reactivity, a recent cadaveric evaluation of the arteriogenesis following an EDAS procedure showed that the formed vessels had the characteristic 3-layer arterial wall anatomy on microscopic analysis (with smooth muscle actin contributing to the medial layer), and that these vessels had formed and maintained integrity since their inception from the surgery 22 years prior to death[177].

There is a clinical need for non-invasive tools to monitor surgical outcomes in moyamoya patients, as many patients with this condition are diagnosed at young ages and serial imaging using ionizing radiation involves risks over the lifespan. CVR studies using low levels of carbon dioxide are safe, well-tolerated, feasible on clinical scanners without using exogenous contrast or special instrumentation[82,84], and minimally affected by craniotomy hardware [178]. Also, this method allows for larger spatial coverage and reflects tissue-level function of collateral vessels, versus large vessel patency alone.

There are several limitations that should be considered. First, our sample size for participants with minimal revascularization is limited, and we may be underpowered to robustly evaluate post-surgical changes in this group. However, the group with >1/3 MCA territory revascularization yielded consistent and significant results that reflected post-surgical findings on DSA. Second, hypercapnic hyperoxia instead of hypercapnic normoxia, was used for CVR studies in moyamoya patients. Hypercapnia hyperoxia (e.g., carbogen) is an FDA-approved drug which makes its use as a vascular stimulus widely accepted, however the added influence of hyperoxia has a complicated hemodynamic profile[170]. We provide additional data using both stimuli in control subjects, and prior studies have compared regional differences between both stimuli. Additionally, vascular stimuli, which increase cerebral blood volume, can result in relocation of cerebral spinal fluid (CSF). Prior work performed however has shown that inter-voxel CSF relocation during strong neuronal stimulation is small (approximately 1%) at similar spatial resolution, and is also localized

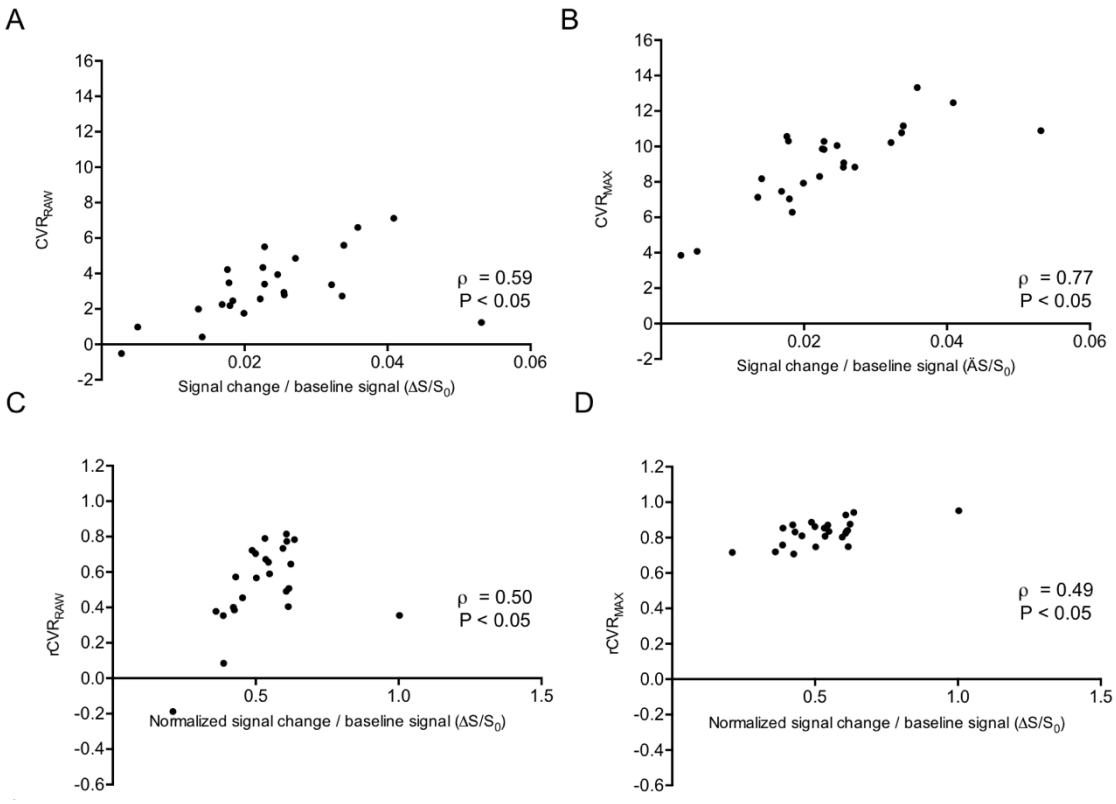

Figure 32. Correlation of CVR compliance measures and BOLD signal Average values were calculated in the middle cerebral artery territory of operative hemispheres in participants with moyamoya. Relative BOLD signal changes ($\Delta S/S_0$) is defined as the mean difference in the signal during the final 90s of each stimulus block (total stimulus block duration = 180s) and baseline block, divided by the mean signal during the final 90s of the baseline block. Un-normalized (e.g., prior to normalization by posterior cerebral artery flow territory) z-statistic values are reported for CVR_{RAW} and $CVR_{MAX,}$ and are plotted against $\Delta S/S_0$ and shown in panels A and B, respectively. Normalized z-statistic values of $rCVR_{RAW}$ and $rCVR_{MAX}$ are plotted against normalized $\Delta S/S_{0,}$ and shown in panel C and D, respectively. CVR_{RAW} and CVR_{MAX} are significantly correlated with $\Delta S/S_0$ (P=0.002, P<0.001, respectively). The correlation between CVR_{MAX} and $\Delta S/S_0$ is stronger, potentially due to reactivity time-delay contributing to more variable CVR_{RAW} z-statistic measures during wash-in of the hypercarbia. When evaluating normalized measures, both $rCVR_{RAW}$ and $rCVR_{MAX}$ are significantly correlated with normalized $\Delta S/S_0$ (P=0.014, P=0.014, respectively).

primarily to superficial cortical layers[179]; given the more mild stimulus used here and larger ROIs, we do not believe that this effect represents a major confound. Third, more quantitative approaches such as ASL have been evaluated in revascularized patients, and have the advantage of yielding measures of CBF in ml/100g tissue/min[150,180], however ASL is of limited use with recommended parameters when blood arrival times are delayed more than

a few seconds, due to the finite lifetime of the magnetic tag on the blood ($T_{1,blood}$ = 1.65s at 3T[89]). Of note, in the composite maps of the vascular compliance measures, many of the regional changes were most notably observed in the deep white-matter, which due to delayed blood arrival time, cannot be accurately measured by ASL approaches[77]. Finally, we focused on statistical measures, rather than absolute signal changes, in the time regression approach as these have been shown to be better indicators of lateralizing disease in these patients[84]. However, we also quantified absolute change in BOLD signal from baseline, which was also significantly correlated with the rCVR measures, as expected (Figure 32).

3.7 Conclusions

We applied traditional CVR and novel time-delay BOLD image processing in patients with moyamoya before and after surgical revascularization in addition to DSA evaluation of collateral vessels. Neovascularization as seen on DSA was associated with tissue-level improvements in vascular compliance measures as determined by traditional regressor and reactivity time-delay approaches. Traditional and time-delay analysis of CVR data may provide a non-invasive tool for monitoring of revascularization success, tissue-health, and potentially future stroke risk.

CHAPTER 4

CASE REPORT: REVASCULARIZATION IN ATYPICAL MOYAMOYA

4.1 Purpose

To report on a case of a personalized use of the vascular compliance imaging discussed in Chapter 3. In this chapter, a patient with an atypical case of moyamoya syndrome and complicated medical history presented with recurrent stroke. In this case report, non-invasive hemodynamic and metabolic imaging was able to evaluate pre-treatment deficits in vascular reserve and oxygen extraction fraction, and subsequent improvement following intervention.

4.2 Summary

Herpes zoster ophthalmicus (HZO) results from reactivation of the varicella zoster virus (VZV) in the ophthalmic segment (V1) of the trigeminal nerve[181]. Severe cases of HZO can result in ipsilateral cerebral angiitis and subsequent cerebral dysfunction.[182] The proposed pathological mechanism is transmission of the virus from the trigeminal nerve to the vessels of the circle of Willis, either via trigeminal branches that innervate the middle cerebral artery (MCA) or direct internal carotid artery (ICA) contact within the cavernous sinus[183]. Vasculopathic changes, if present, typically occur eight weeks following disease onset, although this can range from several days to six months following presentation[184].

Standard treatment options for HZO-related vasculitis are medically-based and focus on anti-inflammatory agents, anti-viral treatment, and support of any underlying vascular insufficiency. However, prolonged vasculitis may lead to significant arterial steno-occlusion[185] and potentially collateral formation in a moyamoya pattern. Medical treatment is unlikely to reverse these end-result changes; thus, surgical revascularization may be reasonable. The most common type of direct surgical revascularization involves a superficial temporal artery (STA)-to-MCA bypass, which can result in immediate improvement in cerebral blood flow (CBF; ml/100g/min).[186] Indirect revascularization most often involves

placement of the STA in proximity to the pia or dura, which leads to neoangiogenesis and enhanced CBF over a longer duration through formation of collateral vessels[186].

We report on a combined direct-and-indirect surgical revascularization performed in a patient presenting with HZO-induced vasculopathy with moyamoya changes and multiple ischemic infarctions.

4.3 Case History

A 57-year-old Caucasian female with no significant past vascular medical history developed HZO along the right V1 trigeminal nerve distribution. The cutaneous manifestations resolved following treatment with oral valacyclovir (1000 mg, three times daily). However, two months post-infection she presented to an outside facility with an acute episode of slurred speech and weakness of the left arm, face, and leg. Magnetic resonance imaging (MRI) and computed tomography angiography (CTA) were performed, and the patient was discharged after being prescribed 81 mg aspirin therapy. Four months post-infection, the patient again experienced multiple episodes of left hemiparesis, dysarthria, and gait ataxia, and clinical evaluation demonstrated a concern for underlying vasculitis. Digital subtraction angiography (DSA), vessel wall imaging (VWI), and hemodynamic imaging, along with magnetic resonance angiography (MRA) and CTA were performed to assess hemodynamic

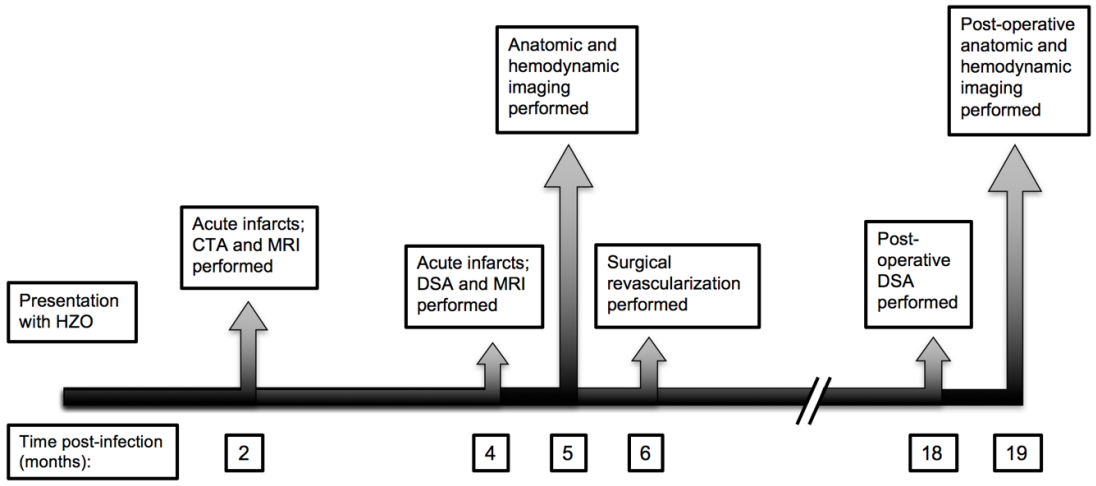

Figure 33. Timeline of clinical history.

compromise (Figure 33, Table 8). All other typical ischemic stroke evaluations were negative, including echocardiogram, cholesterol panel, and infectious/inflammatory laboratory studies (erythrocyte sedimentation rate and C-reactive protein). Lumbar puncture was planned but deferred following the angiogram findings. She was treated with aspirin and cilostazol (50 mg, twice daily), and surgical revascularization was offered due to the continued failure of medical management and the progressive nature of the imaging findings.

Measurement (units)	Method	Relevant parameters
Angiographic (Allura Xper, Philips Healthcare, Best, The Netherlands)		
Lumen diameter (percent stenosed)	Digital subtraction angiography	Catheterization and injection of the right ICA, right ECA, left vertebral artery, and left common carotid artery.
Anatomical (3.0T Achieva, Philips Healthcare, Best, The Netherlands)		
Infarcts (count and volume)	FLAIR	Spatial resolution=0.4x0.3x5.0 mm^3; TR/TE/TI=11000/120/2800 ms, 2D spin echo EPI
Tissue structure	T1-weighted	Spatial resolution=1.0x1.0x1.0 mm^3; TR/TE=9.0/4.6 ms, 3D MPRAGE
Vessel wall thickness (mm)	3D turbo-spin-echo MRI	Spatial resolution=0.6x0.5x0.5 mm^3; variable refocusing angle=40-120deg; TR/TE=1500/38.5 ms; TSE-factor=56, duration=6 min 51 s
Hemodynamic (3.0T Achieva, Philips Healthcare, Best, The Netherlands)		
CBF (ml/100g/min)	Pseudo-continuous arterial spin labeling (pCASL)	Spatial resolution=3.5x3.4x5.0 mm^3, duration=4 min 20 s, TR/TE/post-labeling delay = 4000/13/1800 ms, 2D gradient echo EPI. CBF was quantified using a two-compartment kinetic model.
CVR (Z-statistic)	Hypercapnic blood oxygenation level-dependent (BOLD) MRI	Statistical measure of how well each voxel responds to hypercapnic stimulus without correcting for reactivity timing delays: z-statistic between stimulus regressor and voxel time course. Two 3-minute blocks of hypercapnia were administered interleaved with room air. BOLD-weighted, spatial resolution=3.0x3.0x3.5 mm^3; TR/TE=2000/35 ms; duration=12 min 10s, 2D gradient echo EPI.
OEF (unitless)	TRUST MRI	Ratio of oxygen consumed to oxygen delivered. T2-relaxation-under-spin-tagging using. Four effective echo times: 0, 40, 80, and 160 ms. Image acquired 20 mm superior to confluence of sinuses. Duration=1 min 12 s.

Table 8. Imaging and angiographic methods.

4.4 Imaging studies

CTA from initial presentation two months post-infection revealed bilateral carotid fibromuscular dysplasia (FMD) and mild stenosis of the distal right internal carotid artery (ICA) and A1 segment of the anterior cerebral artery. Later CTA findings demonstrated stable FMD but progressive stenosis in the distal right ICA and proximal M1 and A1 segments.

DSA performed four months post-infection demonstrated bilateral ICA FMD. The distal right ICA and proximal M1 segment demonstrated diffuse stenosis with irregular beading of the vessels and delayed cortical filling, no filling of the right A1 segment, collateralization from the right posterior circulation, and increased caliber of lenticulostriate vessels. The findings represented Suzuki stage III moyamoya changes (Figure 34A-C).
MRI two months post-infection revealed an acute infarct in the right parietal lobe. MRI five months post-infection demonstrated multiple acute infarcts in the right frontal, parietal, and temporal lobes along with diffuse FLuid-Attenuated-Inversion-Recovery (FLAIR) hyperintensity within the right hemisphere (Figure 35A,C).

Figure 35 shows pre and post-surgical structural and hemodynamic imaging. Cerebrovascular reactivity (CVR)-weighted mapping indicated diffusely impaired right-sided reactivity with a relative reactivity 4.6-fold lower than the left MCA territory (Figure 35E). Pre-surgical CBF-weighted MR images demonstrated decreased right-sided CBF (41.3 ml/100g/min) compared to the contralateral hemisphere (46.6 ml/100g/min) (Figure 35G). Whole-brain oxygen extraction fraction (OEF) was observed to be 0.42, higher than what has been previously found for healthy controls (interquartile range=0.29-0.38)[187]. Intracranial VWI demonstrated thickening of the right MCA compared to the contralateral MCA (Figure 36).

4.5 Management

Due to the progressive nature of her symptoms and imaging findings as well as failure of medical therapy, surgical revascularization was pursued in the form of a direct STA-MCA

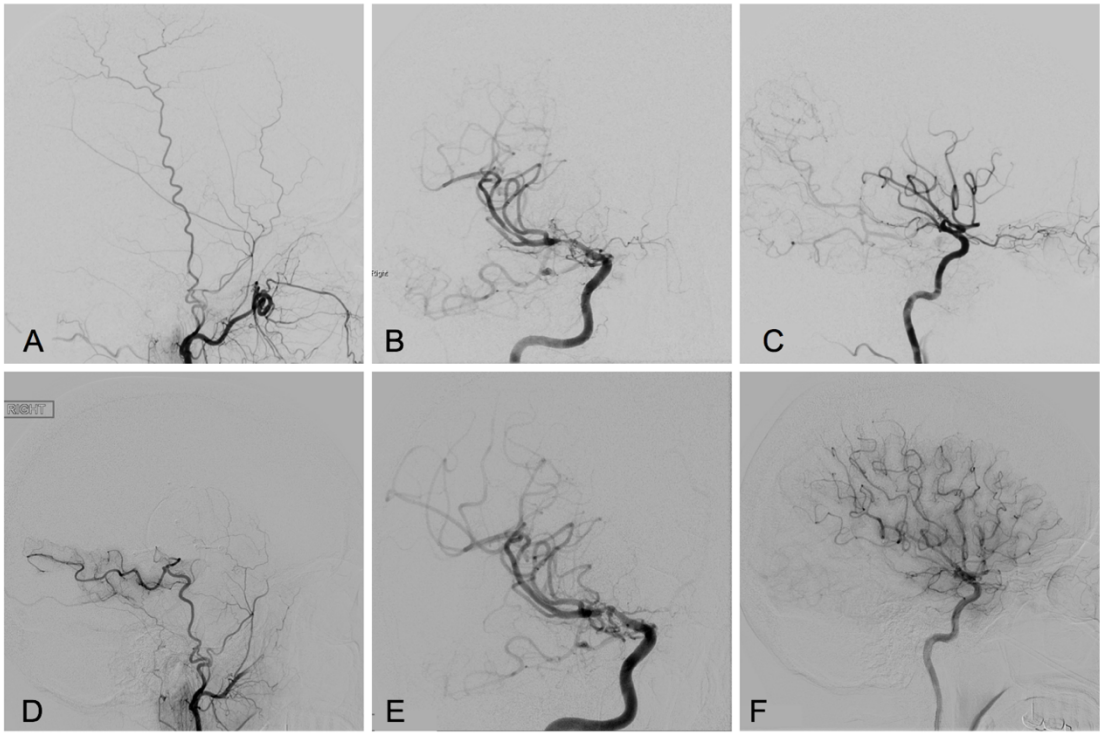

Figure 34. Pre- and post-operative DSA. Injectrion of intracarterial contast was performed on right ECA and ICA pre-operatively (A-C) and one year post-surgical revascularization (D-E). Patency of the STA graft into the posterior inferior MCA territory is seen (D). Note the degree of stenosis in the ICA and MCA (B) and improvement post-operatively (E). Improved filling of the MCA parenchyma is noted (F) compared to the paucity of filling pre-operatively (C).

bypass six months after initial clinical presentation. A direct bypass was chosen due to the robust size of the parietal STA branch (diameter=1.6 mm), rapid symptom progression, and age. A standard surgical preparation was undertaken with an initial distal-to-proximal dissection of the STA, vessel preparation, and underlying craniotomy. Once a suitable cortical MCA branch was prepared, an end-to-side anastomosis was performed with a fish-mouthed STA graft and interrupted 9-0 nylon sutures. Intra-operative indocyanine green video-angiography was performed demonstrating good patency of the anastomosis. The residual peri-vascular cuff was then sutured to the exposed pia with 9-0 nylon sutures to provide additional pial synangiosis. No intra-operative or post-operative complications were observed.

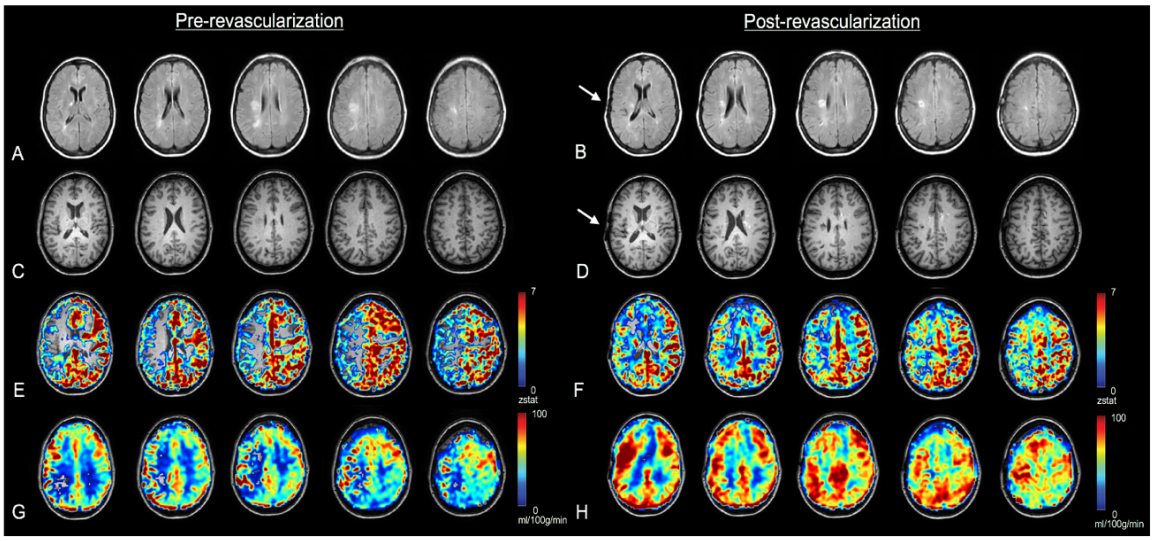

Figure 35. Anatomical and hemodynamic imaging. Imaging was performed before surgical revascularization and one year after surgical revascularization. Axial slices from T_2-weighted FLAIR (A,B) and axial slices from T_1-weighted (C,D) are shown pre- and post-revascularization. Structural MRI reveals multiple infarcts in the right hemisphere following infection. Structural MRI findings after surgical revascularization reveal the evolution of the same infarcts, but suggest no new infarctions Axial slices from CVR-weighted hemodynamic imaging show decreased right-sided reactivity pre-surgery (E), and improvement at follow-up (F). Axial slices from CBF-weighted imaging show decreased blood flow in the right MCA territory pre-surgery (G), and improvement following surgery (H). MRI after surgical revascularization reveal the evolution of the same infarcts, but suggest no new infarction. Arrows denote the site of surgical revascularization.

4.6 Follow-up

The patient tolerated surgery well and was maintained on aspirin and cilostazol. On last follow-up examination (one year post-operatively) the patient demonstrated a fully intact neurological examination with no residual symptoms. The patient resumed all pre-stroke activities with a modified Rankin Score=0.

DSA and anatomical and hemodynamic MRI were performed one year post-operatively. DSA revealed persistent stenosis in the distal ICA and proximal MCA, but improved quality of cortical filling. The STA graft demonstrated preserved patency and excellent filling into the posterior and inferior MCA cortical territories. Filling is seen from the anastomosis into the more superior MCA territories with less robustness. This is

consistent with improved competitive flow from the proximal MCA (Figure 34D-F). Anatomical MRI showed the evolution of white matter chronic infarcts, but no new infarcts (Figure 35B,D). Hemodynamic CBF-weighted imaging revealed an increase in CBF to 70.7 ml/100g/min in the MCA territory of the right hemisphere (Figure 35H). CVR analysis revealed an increase in the post-operative right hemisphere reactivity, with a relative reactivity 1.3-fold lower than the contralateral MCA territory, indicating more symmetric reactivity than present prior to surgery. (Figure 35F). Whole-brain OEF decreased post-surgery to 0.38. Finally, VWI revealed reduction in the thickness of the right MCA (maximum wall thickness=2.2 mm); however, wall thickness remained elevated compared to the contralateral MCA vessel wall (Figure 36B,D).

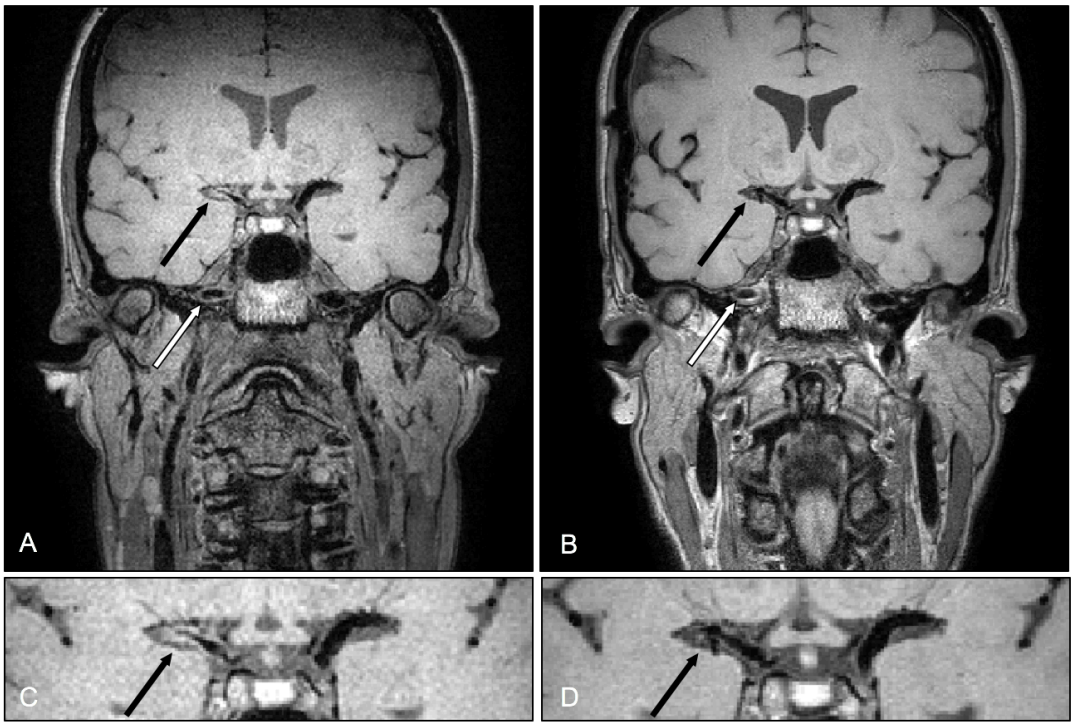

Figure 36. Vessel wall imaging. VWI performed five-months post-infection demonstrates severe concentric vessel wall thickening of the right distal cervical ICA (white arrow) and the right ICA terminus and proximal MCA (black arrow). (B) VWI performed one-year post-surgery reveals persistent cervical ICA wall thickening (arrow 1) on the right compared to the left. (C) Magnified coronal slice of the MCA demonstrates the intracranial wall thickening. Improvement is seen at 14 month follow-up (D).

4.7 Discussion

We present a case of unilateral moyamoya syndrome induced by HZO vasculopathy treated with direct surgical bypass. While varicella zoster vasculopathy is a well-described[185] cause of stroke, surgical treatment of HZO patients with moyamoya syndrome has not been reported. As atypical presentations of moyamoya syndrome are occurring more frequently, particularly in the United States, increased awareness is critical for appropriate treatment[126]. In this case, treatment of moyamoya syndrome with a surgical bypass resulted in an excellent clinical outcome and should be considered in future vasculitis-induced moyamoya syndrome cases.

In addition to conventional imaging, hemodynamic imaging provided additional information for monitoring the functional status of the brain. CBF-weighted imaging demonstrated increased right-sided blood flow post-revascularization. CVR-weighted imaging showed improvements in the right hemisphere following surgery. The increase in CVR is consistent with parenchyma operating further above reserve capacity (e.g., maximal arteriolar autoregulation). OEF analysis, which has been shown to correlate with disease severity[134, 187] showed a decrease following revascularization, indicating improvement in vascular function. Finally, VWI, which has in recent studies been shown to be discriminatory for determining etiology of vasculopathy,[188-190] was performed which aided in diagnosis of inflammatory vasculopathy likely due to HZO.

These findings should be considered in the context of several limitations. Because the patient experienced no neurological symptoms before infection with VZV, the exact temporal course of cerebrovascular disease is unknown; however, the time to presentation with infarcts is consistent with literature on vasculopathy post-infection.[184] Furthermore, the hemodynamic imaging utilized for evaluating the functional status of the parenchyma and for surgical planning is not standard protocol for infarction post-HZO, though it is feasible on clinical scanners. Finally, additional cases are needed in which revascularization is performed for patients with multiple strokes following acute onset of vasculitis in order to substantiate our findings.

4.8 Conclusions

We present a case of symptomatic moyamoya syndrome due to HZO-induced vasculopathy as well as the first reported description of the cerebral hemodynamic impact that revascularization surgery can provide in such a setting. This case report highlights the utility of combined evaluation of similar cases with standard imaging techniques and hemodynamic studies, as well as the possible outcome with surgical bypass revascularization in moyamoya syndrome resulting as long-term sequela from cerebral vasculitis and HZO.

CHAPTER 5

REGIONAL OEF QUANTIFICATION

5.1 Purpose

To extend the functionality of an existing MR method for global oxygen extraction fraction (OEF) determination toward hemispheric and regional measurements. T_2-relaxation-under-spin-tagging (TRUST), discussed in Chapter 1 and 2, is a validated way of determining global OEF. More regional measures of OEF are desired however in order to localize hemodynamic impairment, and evaluate predictive power for stroke in at-risk patient populations. Ultimately, knowledge of localized elevations in OEF may guide treatment, with more impaired regions being targeted for intervention. This chapter proposes a modified TRUST sequence, more amenable to measuring regional OEF.

5.2 Summary

Hemispherically elevated oxygen extraction fraction (OEF; the ratio of oxygen consumed to oxygen delivered) is a potential predicator of subsequent stroke based on ^{15}O positron emission tomography (PET) studies[65-68]. Currently, magnetic resonance imaging (MRI) approaches to assess OEF have limitations either due to limited spatial information, multiple gas challenges, and/or assumptions about complex biophysical systems. One method for assessing OEF is T_2-Relaxation-Under-Spin-Tagging (TRUST), but this method has limitations due to this measure being global[111-113]. In order to obtain regional measurements, added functionality to the existing TRUST sequence is required. The goal of this work therefore is to introduce modifications to the TRUST sequence to make it more conducive for hemispheric and regional OEF measurements. We hypothesize that by (1) movement of the T_2-preparation module to precede labeled blood inflow in the superior sagittal sinus (SSS), and (2) addition of hemispheric saturation pulses to null signal from the contralateral

hemisphere, measurements can be obtained in the SSS reflective of hemispheric venous oxygen saturation. A secondary aim is to replace the currently used venous labeling module (TILT; Transfer Insensitive Labeling Technique[191]) with a Signal TArgeting with multiple Radiofrequency (STAR) module[192], which we hypothesize will have a better labeling profile with greater flexibility for regional labeling in the presence of B_0 and B_1 heterogeneity. Future directions include optimization of the sequence, validation by comparison to whole-brain TRUST, and ultimately application to patients with lateralizing disease and globally elevated OEF.

5.3 Introduction

Clinical relevance of hemispherical OEF

Elevated hemispheric OEF is a well-known predictor of ipsilateral stroke in patients with carotid and middle cerebral artery (MCA) stenosis, as evidenced by multiple ^{15}O-PET studies[65-68]. These studies are discussed in greater detail in Chapter 1, and will be briefly reviewed. In the St. Louis Carotid Occlusion Study (STLCOS), published in 1988, it was found that in patients with unilateral carotid occlusion, that hemispherically elevated OEF as measured by ^{15}O-PET is an independent risk factor for subsequent stroke (Odds-ratio: 6.87; average time to follow-up = 31.5 months) on multi-variate analysis[68]. An additional study by Yamauchi et al., which included patients with symptomatic internal carotid artery (ICA) or middle cerebral artery (MCA) stenosis, reported a 5-year stroke rate of 71% in patients with elevated OEF, compared to 18% in patients with normal OEF[65]. Following the STLCOS, elevated OEF was used as an inclusion criterion in the Carotid Occlusion Surgery Study (COSS), which was performed to determine if surgical revascularization of patients with carotid artery disease and elevated OEF would reduce ipsilateral stroke at two years when compared to medical management. In patients with successful surgical outcomes, OEF did decreased following intervention to values within healthy control limits.

Despite these promising results, further use of elevated OEF to identify patients at high stroke-risk or to monitor treatment efficacy did not occur, largely due to the technical

complexity of performing ^{15}O-PET studies. As previously mentioned, these studies are limited by the necessity of an on-site cyclotron due to the short half-life of ^{15}O and also require the production of multiple radiolabeled tracers. In the United States, only ~10% of PET centers are capable of producing ^{15}O tracers[156]. Additionally, to obtain absolute instead of relative measurements, an arterial line is required in order to perform decay-correction which can be uncomfortable and burdensome to the patient. In addition to the technical challenges of performing ^{5}O-PET studies, the computational models required to determine absolute OEF values are varied and account for brain and infract volume in different ways, largely relying on manual region-of-interest determination which can be a source of error and is also time intensive[61, 62]. Finally, the use of the ionizing radiation has draw-backs for surveillance, safety and can be cost prohibitive, especially when non-ionizing, less invasive tools are available.

In multiple recent randomized clinical trials evaluating intervention in patients with cerebrovascular disease, baseline hemodynamic compensation, and hemodynamic improvement following intervention was not evaluated. In the recently-halted SAMMPRIS[22,] and VISSIT trials,[13, 14] which concluded aggressive medical management is superior to endovascular stenting in symptomatic intracranial stenosis, patients receiving aggressive medical management, still had a 12.2-15.1% one-year stroke rate, respectively. The mechanisms that confer high stroke risk to some but not others in this population is not known, yet is fundamental to stratifying high-risk patients for additional clinical trial evaluation or intervention.

MRI for regional OEF measures

The ability to use MRI to measure regional and hemispheric OEF, as is done in ^{15}O-PET studies, has proved challenging. Methods that report regional OEF can broadly be classified into three categories: BOLD based approaches, susceptibility based approaches, and approaches that directly measure T_2 in the venous system. These methods were mentioned in Chapter 1, and will be briefly reviewed here.

BOLD methods are based on the theoretical model of BOLD signal contrast first described by Yablonksiy and Haacke in 1994[115]. Gradient echo imaging of brain is used to obtain a voxel-wise T_2^*-weighted image, which is sensitive to field inhomogeneities induced by paramagnetic deoxyhemoglobin among other things. R_2^* is the spin-spin relaxation rate that takes into account both tissue relaxation (R_2), which is irreversible, and relaxation that is attributed to field inhomogeneities (R_2'), which is reversible. The time constants are the inverse of the relaxation rates and are measured in seconds. Equation 4 and 5 summarize the relationship between relaxation rates and time constants:

$$R_2^* = R_2 + R_2' \qquad [4]$$

and

$$\frac{1}{T_{2*}} = \frac{1}{T_2} + \frac{1}{T_2'} \qquad [5].$$

Using the theoretical model of BOLD signal, the T_2^*-weighted image can be used to determine physiologic parameters of deoxyhemoglobin concentration and OEF[115, 193] after assumptions are made about tissue T_2 values, tissue density, microvascular hematocrit, blood volume, and vessel orientation. In a more recently described method, termed Quantitative BOLD (qBOLD)[114], a gradient echo sampling of spin echo (GESSE) sequence is used which allows fitting of both R_2 and R_2'; both required inputs in a multi-compartment BOLD signal model and contribute to the R_2^*[194]. In brief, the GESSE sequence is a spin-echo sequence in which gradients are embedded around the single echo time, thus providing adequate data for fitting of voxel-wise R_2 and R_2'. Preliminary work implementing qBOLD in healthy controls has been performed and results for OEF are within range of literature reported values[114]. Using qBOLD, image acquisition does not require a complex protocol or multiple scans; however, the use of multiple assumptions about physiological parameters, in addition to the need for manual segmentation and thresholding to avoid partial volume effects, make the validation and application of this approach challenging especially in patients where typical physiological assumptions are incorrect.

Calibrated BOLD methods have also been used for voxel-wise oxygen metabolism measurements, and are based on measured susceptibility differences between baseline BOLD signal and vascular stimulis[116,117,195,196]. In calibrated BOLD experiments, CBF and BOLD data are acquired either during separate scans, using interleaved methods, in which ASL and BOLD data are acquired from separate excitations[197], or using a single-shot approach in which both ASL and BOLD data are acquired after a single excitation, allowing for higher temporal resolution. Scan times for calibrated BOLD protocols can be long, and require administration of gas stimuli. This method applies assumptions about extravascular blood-water relaxation properties described by the static dephasing regime[115], which relates susceptibility changes to changes in blood volume and deoxyhemoglobin concentration. At 3T, approximately 70% of the BOLD effect is extravascular[118]; therefore, not accounting for intravascular BOLD effect in this model is a limitation. Also, field-dependent lumped biophysical constants, based on the theoretical effect of vessel diameter, diffusion effects around the vessel and vessel geometry on susceptibility changes, is a limitation of this method. Finally, the relationship between cerebral blood volume and cerebral blood flow can be uncoupled to changes in energy metabolism, which is not accounted for in this method.

Susceptibility based methods measure the frequency shift that occurs in water surrounding deoxyhemoglobin. Quantitative Imaging of eXtraction of Oxygen and Tissue Consumption (QUIXOTIC) and Venous oxygenation mapping using Velocity-Selective Excitation and Arterial Nulling (VSEAN), use velocity selective labeling targeted at microvasculature flow, and measure changes in susceptibly attributed to labeled blood. Therefore, voxel-wise maps are generated using these approaches. Labeling of post-capillary blood depends on orientation of vessels, with vessels parallel to B_0 not experiencing frequency shifts, and are therefore not accounted for using this method. Additionally, the consideration of cerebrospinal fluid (CSF) and static tissue contribution to measured venular T_2 values is still not fully understood, and could potentially contribute to large source of error. Phase-based regional oxygen metabolism (PROM), which targets small veins using velocity selective modules, assumes a cylinder model to the vessels and require manual segmentation of veins, or restrictive masking, to determine usable voxels for analysis.

T_2-Relaxation-Under-Phase-Contrast (TRU-PC), is an extension on the TRUST method, which quantifies venous oxygenation in major veins using bipolar gradients to isolate venous blood signal from surrounding tissue[119]. This method has potential to provide more regional information, however is limited to large veins.

Regional OEF Measures in Cerebrovascular Disease

To date, only a few recent studies have demonstrated the feasibility of applying regional OEF measurements to patients with cerebrovascular disease. Liu et al. 2016[198], which evaluated hemispheric OEF in patients with varying degrees of MCA stenosis, found gradually increased OEF in patients with more significant stenosis. This paper used manual segmentation of phase data to isolate veins in each hemisphere that were capable to be fitted to the long-cylinder model[199]. Kudo et al. 2016[122] compared hemispheric OEF ratios using quantitative susceptibility mapping (QSM) to ^{15}O-PET measured OEF ratios in patients with unilateral carotid stenosis, and found strong correlation between the modalities, but significant differences in absolute value measurements (r=0.62). As discussed in Chapter 1, only a small number of veins were suitable for analysis. Results from both of these susceptibility techniques are promising, and confirm sensitivity to detect elevated OEF in cerebrovascular disease, however the assumption that a small number of analyzed veins is representative of underlying tissue compensation in brain parenchyma is not not necessarily true. Additionally, in both methods, veins that were in or around infarct volume were excluded due the potential presence of blood products and partial voluming considerations that can affect quality of susceptibility data.

Extension of TRUST for Regional Measurements

Evaluation of venous oxygenation (Y_v) in the superior sagittal sinus using TRUST (Figure 17), combined with a measurement of arterial oxygenation (Y_a), is a way to determine whole-brain OEF[111]. The use of TRUST for measuring whole-brain OEF has been validated by manipulation of blood gases and comparing TRUST measured T_2 values with *ex vivo* measurements[112].

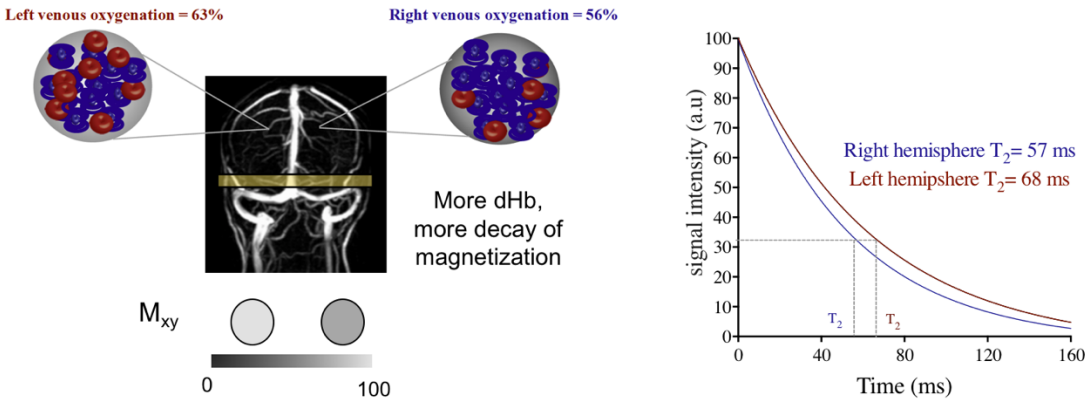

Figure 37. Hemispheric OEF and T_2. In the example shown, the right hemisphere has a venous oxygenation (Y_v) of 56%. Assuming an arterial oxygenation (Y_a) of 99%, the OEF would be elevated at 0.43, compared to the left hemisphere with a Y_v of 63%, and therefore a normal range OEF of 0.36. More paramagnetic deoxyhemoglobin in the right hemisphere results in more decay of transverse relaxation (M_{xy}), and shorter T_2 values. Therefore, shorter T_2 values correspond to decreased Y_v.

TRUST has also been evaluated at multiple centers, which found a tight range for age-corrected values, and no site-dependence of Y_v measures[113]. To review, global OEF can be determined by TRUST, which is based on the known relationship between T_2 and venous deoxyhemoglobin concentration. By applying a magnetic label to all supratentorial venous blood, allowing venous blood to flow into the superior sagittal sinus (SSS), and subsequently applying non-slice selective T_2-preparation pulses to confer T_2-weighting at multiple effective echo times (eTEs), venous blood T_2 can be determined, and therefore Y_v. Isolation of only venous blood is accomplished by interleaving control acquisitions, in which venous blood spins are not inverted, with labeled acquisitions. Subtraction of the labeled scan from the control scan, allows for isolation of only venous blood signal.

The obvious limitation of TRUST is that it is a whole-brain measurement, and spins from all brain regions that drain into the SSS contribute to the measured venous blood-water T_2. Therefore, the goal of this work is to implement a modified TRUST sequence with added functionality that will make it more conducive for hemispheric and regional measurements of OEF. In a case where OEF is hemispherically or regionally elevated, we anticipate that in our proposed pulse sequence will afford detection of this lateralization of disease. Figure 37

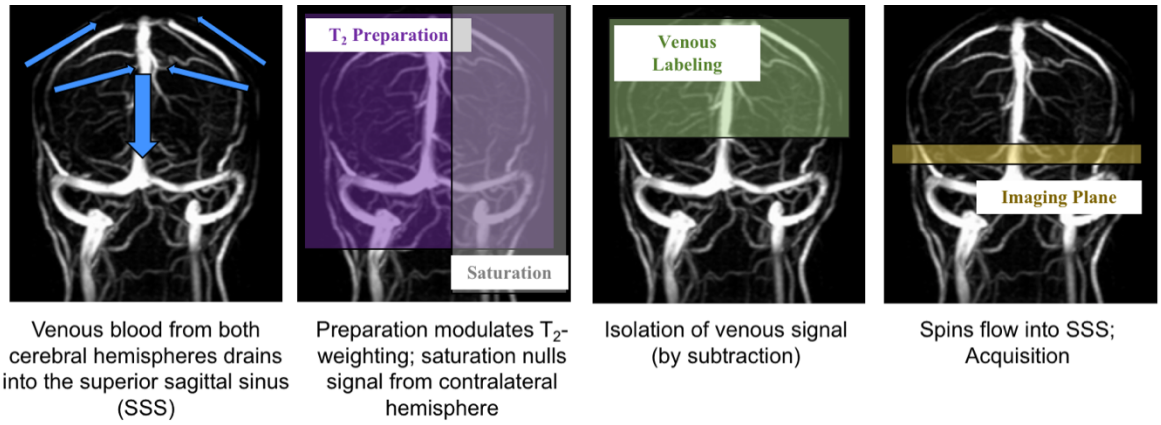

Figure 38. Modified TRUST schematic. T_2-preparation confers T_2-weighting at 4 effective echo times (0,40,80,160ms) and spins from areas outside the area of interest are then saturated. The labeling module allows isolation of venous blood in the superior sagittal sinus (SSS). Spins then flow into the SSS. Isolated venous blood signal can be plotted as a function of effective echo time to determine venous blood T_2.

shows an example of the effect of hemispherically elevated OEF on T_2. The presence of hemispherically elevated OEF results in more deoxyhemoglobin, which causes more dephasing of magnetization in the transverse plane and a shorter T_2 (M_{xy}).

We hypothesize that by movement the the T_2-preparation module to precede labeled blood inflow to the SSS, and addition of hemispheric saturation pulses (to eliminate signal from the contralateral hemisphere), that measurements can be obtained in the SSS reflective of hemispheric venous oxygenation saturation. A conceptual representation of this modified TRUST sequence is shown in Figure 38.

A secondary aim is replace the currently used venous labeling module (TILT; Transfer Insensitive Labeling Technique[191]) with a Signal TArgeting with multiple Radiofrequency (STAR) module[192]. We hypothesize that the adiabatic inversion with STAR will result in a better labeling profile compared to the TILT module, which uses hard pulses for spin inversion. An advantages to frequency modulated adiabatic inversion includes less sensitivity to field inhomogeneity[200].

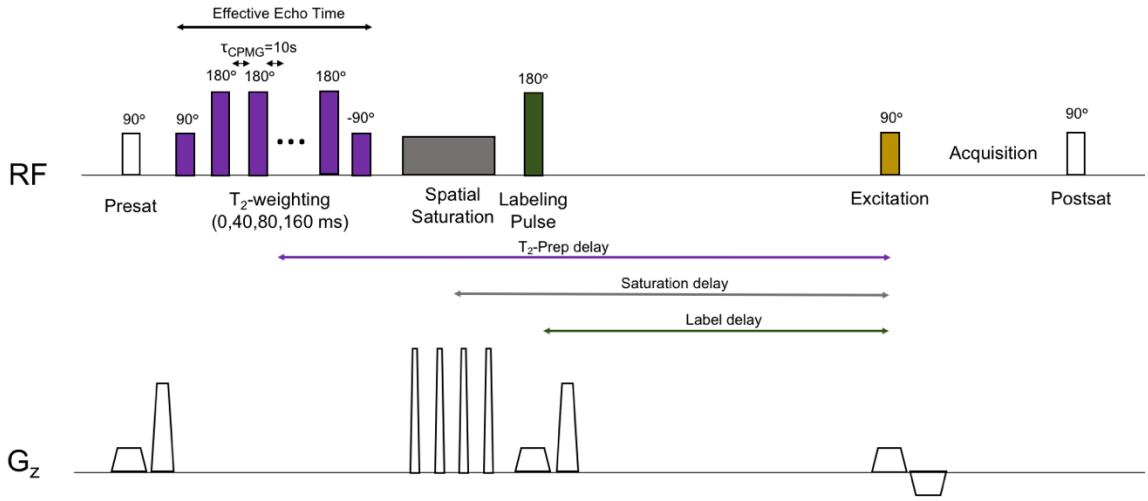

Figure 39. Modified TRUST pulse sequence. Added functionality includes a spatial saturation pulse, and movement of the T_2-preparation module to precede blood inflow to the superior sagittal sinus.

Progress on each goal of this work is detailed below. Immediate future directions of this work includes sequence optimization, with longer term goals of applying an optimized sequence to determine reproducibly when compared to whole-brain TRUST, in addition to determining sensitivity to lateralizing cerebrovascular disease. Figure 39 shows a schematic of the modified TRUST pulse-sequence diagram.

5.4 Preliminary results of implementation

All MR imaging and angiography was performed on a 3 Tesla scanner (Philips Healthcare, Best, The Netherlands) using body coil radiofrequency transmission and 32-channel SENSE-array reception. Voxel-size, placement of imaging slice, T_2-preparation module, and effective echo times (eTEs) used are identical to the previously described TRUST method detailed in Chapter 2[111,112].

Saturation pulses

Preliminary analysis of saturation slab profiles was performed in a phantom and *in vivo*. The purpose of these experiments was (1) to evaluate the saturation profile obtained using slabs

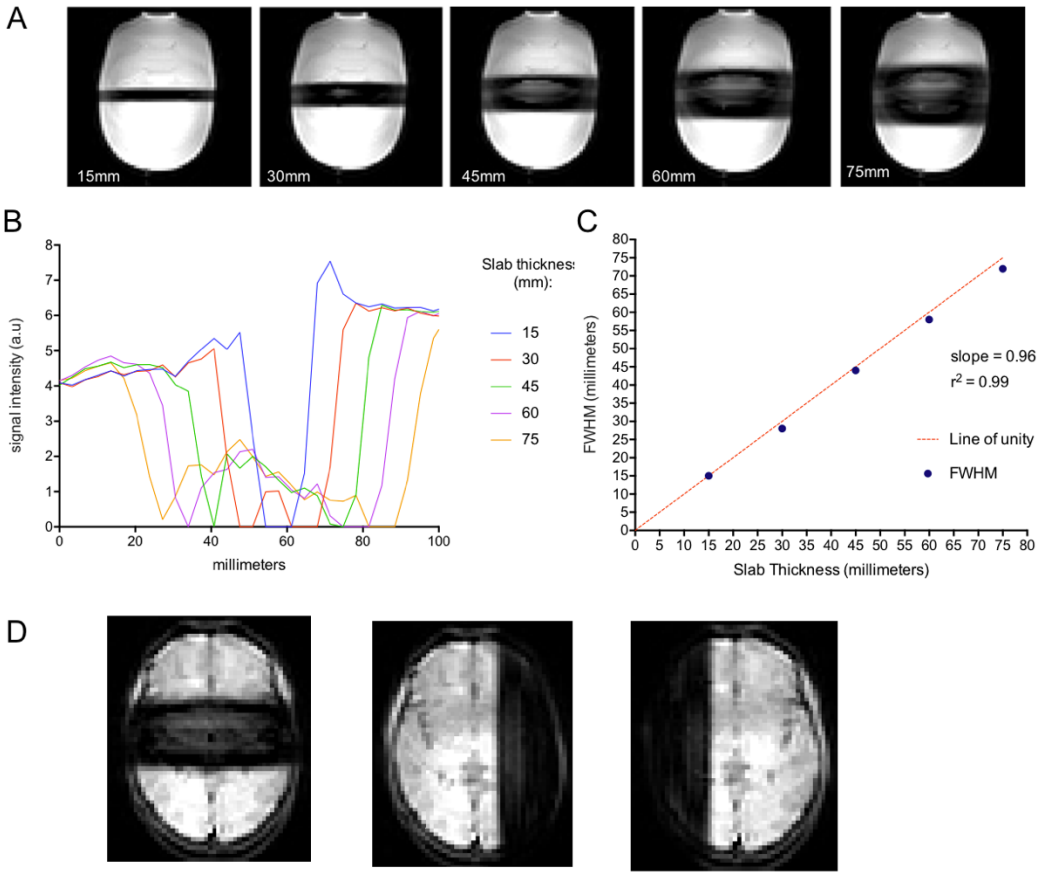

Figure 40. Saturation pulses. Data was acquired over a range of saturation band thicknesses. (A) shows images collected in a phantom, (B) shows the corresponding intensity profiles of each saturation band, and (C) shows the relationship between prescribed slab thickness and calculated full width half maximum values. *In vivo* data was collected using a 60mm saturation band applied to different brain regions (D).

of different thicknesses, (2) to test the ability to control saturation pulse placement in different brain regions, and (3) to confirm functionality of the saturation pulse to null tissue and blood signal. A WET (Water Suppression Enhanced through T_1 effects) module was therefore inserted prior to excitation to evaluate slab profiles. A WET module uses multiple radiofrequency (RF) pulses, each followed be a dephasing gradient to perform spin saturation over a range of species with different T_1 values. Data collected in a phantom over a range of saturation slab thicknesses is shown in Figure 40 and signal within the saturation slab is decreased. *In vivo* analysis of a 60mm thick saturation band in different brain regions is shown in Figure 40D.

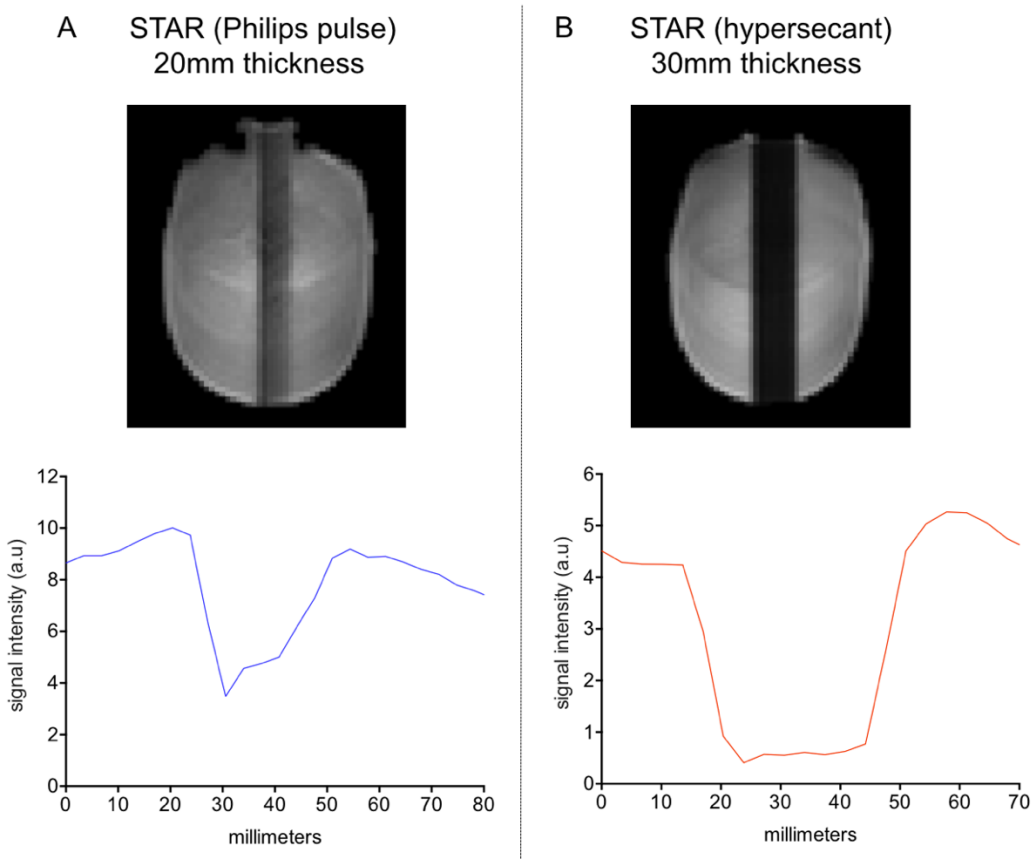

Figure 41. STAR labeling. The TILT modules was replaced with a STAR module. First an unmodified STAR module was applied to a phantom (A). Replacement of the standard adiabatic inversion pulse with a hypersecant pulse, resulted in better spin inversion (B).

Movement of T_2 Preparation Module

We moved the T_2-preparation pulse to immediately follow the label (or control) pulse. The time between labeling and T_2-preparation was set at 15 ms, and the T_2-preparation delay was set at 1007 ms, which is almost identical to the post-labeling delay used in TRUST (determined to be the length of time it took for labeled blood to flow into the superior sagittal sinus; 1022 ms). Results of placement of the T_2-preparation pulse immediately preceding acquisition did not result in signal decrease as a function of eTE. We therefore have moved the T_2-preparation to precede venous labeling. Consideration of the phase of the spins following labeling may be a reason why labeling following T_2-preparation will be a better approach moving forward.

Venous labeling modules

The TRUST methods employs a TILT labeling module which uses two successive block sinc-gauss 90° RF pulses to invert spins. The STAR labeling module, which uses adiabatic inversion, we hypothesize will result in more spin inversion compared to TILT. First we evaluated spin inversion of STAR labeling. Initial results are shown in Figure 41A. Replacement of the pre-programmed inversion pulse with a hypersecant pulse resulted in a better spin profile shown in Figure 41B.

Blood labeling

Additional experiments have been performed to evaluate feasibility of hemispheric labeling of venous blood using spatially selective labeling pulses. Partial labeling of venous blood-water was achieved by changing the direction of the labeling plane from transverse to coronal, and applying a spatial offset. *In vivo* evaluation of the modified TRUST sequence with partial labeling of venous blood-water is shown in Figure 42. As expected, evaluation of signal intensity from the subtracted (control-label) images, resulted in decreased signal intensity in the SSS.

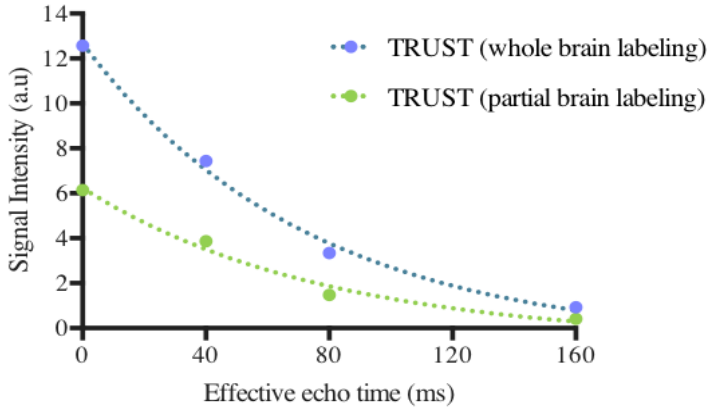

Figure 42. Partial venous labeling. A labeling module is applied to only part of the venous blood in TRUST. Signal intensity from subtracted (control-label) images is decreased across all effective echo times.

5.5 Future directions

Optimization of the modified TRUST sequence is required. Specifically, the timing between each module needs to be determined. Spin preparation prior to labeling should allow for modulation of magnetization in the M_{xy} plane, and labeling of spins will only invert spins along $M_{Z.}$ Assuming successful determination of timing delays, and confirmation of contralateral hemisphere signal dephasing with the saturation band, it should be possible to obtain SSS T_2 values which can be converted to venous oxygenation values, identical to what is done when performing the whole brain TRUST-protocol. Additionally, direct comparison of STAR and TILT pulses is a future direction, and so far has been limited by programmed features of the TILT labeling module, making manipulation of labeling plane orientation and offset difficult. Additional methods to isolate venous blood are also of interest. Specifically, leveraging a vascular crusher gradient, which nulls signal from flowing spins, could potentially be used instead of a venous labeling. Subtracting an image acquired without vascular crushing from an image acquired with vascular crushing could isolate signal attributed only to flowing spins. If successful, this would eliminate the need for a venous labeling module.

Overall, we have successfully evaluated additional modules that will enhance the functionality of the TRUST sequence and allow more regional measures. The addition of a saturation pulse that can be moved freely to null signal is important so that signal from outside the area of interest will not contribute to T_2 decay measured in the SSS. Movement of the T_2-preparation pulse to non-slice selectively confer T_2-weighting to spins in the tissue coupled with addition of the saturation pulse should allow regional isolation of spins. Additionally, use of the STAR labeling module, which can be freely moved around the imaging plane, may also be useful for isolating spins from a brain region. Optimization of timing between each module of the modified TRUST sequence is our next priority, and we anticipate that T_2-preparation followed by venous labeling will allow detection of signal decrease as a function of eTE when imaging in the SSS and afford a localized measure of OEF.

CHAPTER 6

CONCLUSIONS AND FUTURE DIRECTIONS

The work presented in this dissertation evaluates hemodynamic compensation mechanisms in cerebrovascular disease, and advances upon existing methods for regional measures of oxygen extraction fraction (OEF; ratio of oxygen consumed to oxygen delivered). Chapter 2 evaluated OEF in patients with moyamoya and sickle cell anemia, two patient populations at high-risk for stroke. The major finding was that global OEF, evaluated using the T_2-relaxation-under-spin-tagging (TRUST) sequence, was significantly elevated in these patients, and that OEF was inversely correlated with cerebral blood flow in patients with intracranial stenosis. Prior to this study, it was not known if a global measure of OEF would be sensitive to hemodynamic impairment in moyamoya. Future directions include longitudinal evaluation of OEF in patients with cerebrovascular disease to determine if hemodynamic impairment, as determined by elevated OEF, corresponds to clinical symptomatology of transient ischemic attack and stroke.

Chapter 3 evaluated traditional and novel metrics of cerebrovascular compliance in patients with moyamoya before and after surgical revascularization. The major finding was that changes in both cerebrovascular compliance, as evaluated by a standard rectangular regressor analysis, and cerebrovascular reactivity timing, as evaluated by a jittered regressor analysis, improved following successful surgical revascularization determined by gold-standard digital subtraction angiography. In addition to providing evidence in support of non-invasive imaging for this patient group, the finding that time-delays can be over 30 seconds longer in patients with cerebrovascular disease compared to healthy controls has potentially broad implications for researchers that evaluate BOLD reactivity with vascular stimulus. Use of a single regressor and/or protocols that use short (<30s) periods of vascular stimulus can result in erroneous cerebrovascular reactivity measures in patients with cerebrovascular disease. Mechanistically, delay in BOLD response could be due to dysfunction of smooth muscle cells lining arterioles, however this is currently not known. Looking ahead, evaluation of vascular compliance measures in moyamoya patients

undergoing different types of revascularization could provide evidence in support of an indirect, direct, or combined approach. Comparison of revascularization procedures can be difficult in a clinical trial setting due to sample-size limitations and limited centers with expertise to perform revascularization operations. However, a large multi-center trial in conjunction with coordinated efforts to standardize surgical approach of each type of revascularization could provide evidence in support of one type of revascularization.

Chapter 4 presented a case-report of a patient that developed of moyamoya collaterals following vasculitis of intracranial arteries. Due to continued stroke symptomology despite medical treatment, this patient underwent surgical revascularization. Non-invasive hemodynamic and metabolic imaging was performed in this patient before and one-year following surgical revascularization. Improvement in functional outcome was corroborated by improvements in hemodynamic measures of cerebral blood flow, OEF, and cerebrovascular reactivity. This case highlights a personalized use of non-invasive imaging that provided functional information about intervention outcome. While quantitative thresholds for normal versus abnormal are often used when evaluating diagnostic tests, radiological interpretation of imaging findings still largely relies on comparison to prior imaging, or comparison of abnormal tissue to normal appearing tissue. Therefore, despite the lack of definitive ranges for disease compared to normal for many functional MRI methods, the clinical use of functional imaging that can deliver personalized information on cerebrovascular health may prove important in the decision-making process, especially in cases where patients continue to experience stroke symptomatology despite undergoing standard treatment protocols.

Chapter 5 extended upon the TRUST sequence and adds components that will allow for more localized measurement of blood T_2. We have successfully implemented saturation pulses and a venous labeling module that are freely movable in the imaging volume. These additions allow for nulling or regionally selective labeling of blood-water spins, respectively. Optimization of the timing between the modules of the modified TRUST sequence is required. Following optimization, pilot studies in healthy participants will determine reproducibility of the measurement, and also will be compared with the whole-brain TRUST method. Ultimately, application to patients with lateralizing cerebrovascular disease will

determine the sensitivity of this modified TRUST sequence to regional OEF elevations. Multiple larger scale studies would be of interest to perform that leverage the new information provided by this body of work. For example, it would first be of interest to perform an observational clinical study and accrue recently symptomatic patients with underlying intracranial stenosis. Based on the work presented in Chapter 1, we would anticipate that OEF would be elevated in this population. Subsequent longitudinal observation of patients for TIA and/or stroke, combined with serial OEF measurements, could determine if globally elevated OEF was predictive of increased stroke risk after multi-variate analysis.

It would additionally be relevant to evaluate cerebrovascular hemodynamics using the methods described here in populations with symptomatic intracranial atherosclerosis, as recurrent stroke at 1-year exceeds 12%[13,201]. In addition to obtaitning global OEF measures in these patients, collection of perfusion data using arterial spin labeling (ASL) would be of interest, as decreased perfusion could be a predictor of subsequent stroke due to hypoperfusion. Although cerebral blood flow is reported in terms of the absolute units of ml blood/100g tissue/minute, calculated values can differ solely based on the model used for analysis. Additionally, suboptimal scan parameters can cause quantification error. Therefore, there is debate regarding what defines thresholds for normal, ischemic penumbra, and hypoperfusion as measured by ASL which has limited its clinical acceptance[202]. As such, in addition to evaluating OEF and stroke symptomatology longitudinally, baseline perfusion measures could also be evaluated for predictive power. In patients with intracranial atherosclerosis, special attention would need to be taken in order to account for strokes due to progressive hypoperfusion versus artery-to-artery embolus due to unstable plaque.

If globally elevated OEF is predictive of stroke, ultimately a study similar in design to the previously discussed Carotid Occlusion Surgery Study (COSS) trial could be performed to evaluate intervention in a subgroup of patients with elevated OEF and therefore high stroke risk. Additionally, further development and validation of the sequence presented in Chapter 5 of this dissertation would be ideal for implementation in patients with intracranial stenosis, which often presets with lateralizing pathology and symptomatology.

APPENDIX: TIME-DELAY PROCESSING

I will provide an overview of two methods that can be used to determine reactivity time-delay values from BOLD data and address the processing steps involved for both analysis procedures.

FSL time-delay analysis:

This analysis involves the processing of time-shifted regressors in FSL. Two shell-scripts are used for this analysis. The first script will pre-process the data for baseline drift and motion correction, and determine z-statistic values at each time-shifted regressor (script name: run_manustide). The time shifted regressors are in FSL three column format and are rectangular. The second script will merge all of the voxel-wise z-statistic values from each time-shifted regressor and determine the time at which the maximum z-statistic is obtained, and the maximum z-statistic value (script name: run_postproc). If different numbers of measurements are obtained, then modified timing files and scripts are required. Since 2014, we have been collecting BOLD data with 360 measurements (TR=2s), using a standard gas paradigm consisting of 90s room air, 180s carbogen, 180s room air, 180s carbogen, 90s room air.

run_manustide:

Create subject specific output directories for z-stat results

Create subject specific FSL design files (.fsf files)

Pre-process data using feat

Process data using feat and input time-progressed regressor files (progress by 3 seconds)

Delete out design files

Copy the z-statistic values from each regressor into the TIDE folder

run_postproc:

Merge all z-stat data (added 4^{th} dimension)

Find at which regressor the voxel-wise maximum z-stat is obtained (-Tmaxn option)

Convert the integer value to seconds

Determine the voxel-wise maximum z-stat (-Tmax option)

Remove all z-stat files

Rapidtide analysis:

Rapidtide analysis uses multiple python programs to perform rapid time-delay analysis on BOLD data. The program was created by Blaise Frederick and the github repository can be found here: https://github.com/bbfrederick/rapidtide.git. Unlike the FSL time-delay analysis, rapidtide uses data-derived hemodynamic response functions (HRF) and determines delays relative to this HRF. Rapidtide can be run through a python terminal and the syntax is similar to FSL. Due to a scan-specific HRF being used as a probe regressor, it is important to consider options that will define the probe regressor. Since the probe regressor is defined by the data, scans with different numbers of measurements do not need to be considered differently. The following steps outline rapidtide installation and processing.

Installation Instructions:

1) Download the ZIP file named rapidtide from https://github.com/bbfrederick/rapidtide.git.

2) Download anaconda navigator with Python 3.6 (https://www.continuum.io/downloads).

3) Open anaconda navigator. Click on "Environments" on left menu bar. Select the arrow to the right of "root". Choose "open terminal".

4) Browse to the rapidtide folder in the terminal window and type: python setup.py install.

5) Type: pip install pyqtgraph. This is an additional package that needs to be installed in order for rapidtide to work.

6) Type rapidtide2x into the command line and the options should load.

Processing Instructions:

1) Browse to the feat directory containing the filtered functional data in an anaconda terminal window.

2) Command line: rapidtide2x filtered_func_data.nii.gz output name --noglm --multiproc -N 0 --refinepasses=3 -r -10,140 -F 0.00,0.2 -f 2 --lagmaxthresh=40 --ampthresh=0.2 --nofitfilt –refineoffset

filtered_func_data: input data that is motion corrected, high pass filtered, baseline drift corrected.

--noglm: an option that is relevant for processing resting-state or task data where you want to remove physiological noise. For hypercarbia experiments, you do not want to do this and can therefore turn off to save time/disk space.

--multiproc; Enables multiprocessing versions of key subroutines.

-N 0; This disables this feature (which runs "NREPS null correlations").

--refinepasses=3

-r -10,140; Limits the fits to this range (in seconds). The probe regressor will be shifted ten seconds back and 140 seconds forward to find the time at which maximum correlation occurs.

-F 0.00,0.2; Filter data and data-derived regressors from LOWERFREQ to UPPERFREQ. The lower frequency should be set at zero since you have already high-pass filtered the data in the pre-processing. The recommended upper frequency is .2; the data will be low-pass filtered with a cutoff frequency of 0.2 Hz.

-f 2; Smoothing in mm.

--lagmaxthresh 40; when defining the probe regressor excludes voxels with delays >40seconds.

--ampthresh=0.2; excludes voxels with correlation coefficients <0.2 when determining the reference probe.

-nofitfilt; if the fitting fails, the output is the initial estimate of the time-delay.

-refineoffest; adjusts the mean delay time to make the histogram of delays be centered on zero lag. The use of this option has no effect on the lagtime maps, only on other outputs containing histogram data.

Method Comparison

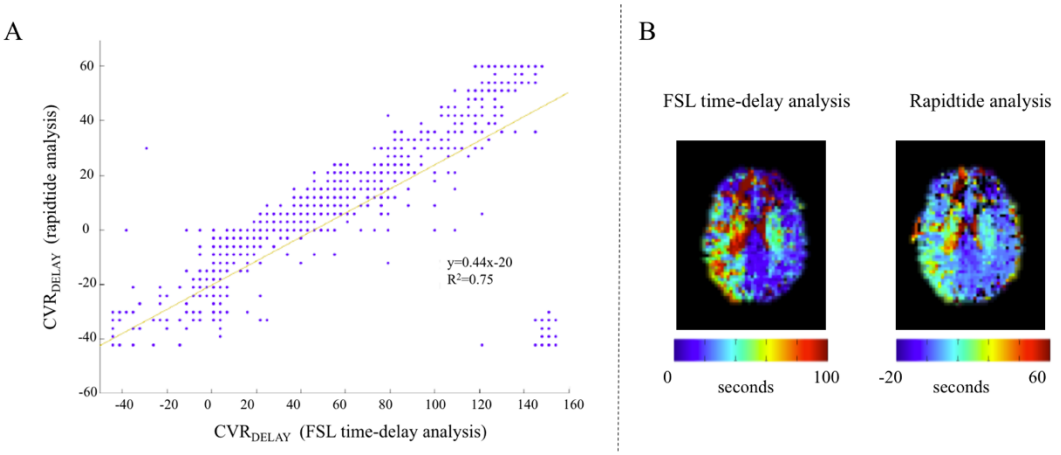

(A): Pearson correlation comparing FSL time-delay analysis with rapidtide analysis (R^2=0.75). Each dot represents voxel in native space (Participant ID: 005_01; slice 20). Strong correlation is observed between the methods.

(B): Time-delay analysis showing slice 20. Regional similarities are appreciated, with time-delay on the right hemisphere being longer compared to the left.

REFERENCES

1. Cdc, Nchs. Underlying cause of death 1999-2013 on cdc wonder online database, released 2015. Data are from the multiple cause of death files, 1999-2013, as compiled from data provided by the 57 vital statistics jurisdictions through the vital statistics cooperative.

2. D M, E.J B, A.S G, D.K A, M.J B, M C, et al. Executive summary: Heart disease and stroke statistics-2015 update : A report from the american heart association. 2015;131:434-441

3. Writing Group M, Mozaffarian D, Benjamin EJ, Go AS, Arnett DK, Blaha MJ, et al. Heart disease and stroke statistics-2016 update: A report from the american heart association. *Circulation*. 2016;133:e38-360

4. Mozaffarian D, Benjamin EJ, Go AS, Arnett DK, Blaha MJ, Cushman M, et al. Heart disease and stroke statistics--2015 update: A report from the american heart association. *Circulation*. 2015;131:e29-322

5. Kleindorfer D, Panagos P, Pancioli A, Khoury J, Kissela B, Woo D, et al. Incidence and short-term prognosis of transient ischemic attack in a population-based study. *Stroke*. 2005;36:720-723

6. Sacco RL, Ellenberg JH, Mohr JP, Tatemichi TK, Hier DB, Price TR, et al. Infarcts of undetermined cause: The nincds stroke data bank. *Ann Neurol*. 1989;25:382-390

7. Li L, Yiin GS, Geraghty OC, Schulz UG, Kuker W, Mehta Z, et al. Incidence, outcome, risk factors, and long-term prognosis of cryptogenic transient ischaemic attack and ischaemic stroke: A population-based study. *Lancet Neurol*. 2015;14:903-913

8. Ji R, Schwamm LH, Pervez MA, Singhal AB. Ischemic stroke and transient ischemic attack in young adults: Risk factors, diagnostic yield, neuroimaging, and thrombolysis. *JAMA Neurol*. 2013;70:51-57

9. Wolf ME, Grittner U, Bottcher T, Norrving B, Rolfs A, Hennerici MG, et al. Phenotypic asco characterisation of young patients with ischemic stroke in the prospective multicentre observational sifap1 study. *Cerebrovasc Dis*. 2015;40:129-135

10. Reith W, Berkefeld J, Dietrich P, Fiehler J, Jansen O. Diagnosis and treatment of intracranial stenoses. *Clin Neuroradiol*. 2015;25 Suppl 2:307-316

11. Hoak DA, Lutsep HL. Management of symptomatic intracranial stenosis. *Curr Cardiol Rep*. 2016;18:83

12. Banerjee C, Chimowitz MI. Stroke caused by atherosclerosis of the major intracranial arteries. *Circ Res*. 2017;120:502-513

13. Chimowitz MI, Lynn MJ, Derdeyn CP, Turan TN, Fiorella D, Lane BF, et al. Stenting versus aggressive medical therapy for intracranial arterial stenosis. *The New England journal of medicine*. 2011;365:993-1003

14. Zaidat OO, Fitzsimmons BF, Woodward BK, Wang Z, Killer-Oberpfalzer M, Wakhloo A, et al. Effect of a balloon-expandable intracranial stent vs medical therapy on risk of stroke in patients with symptomatic intracranial stenosis: The vissit randomized clinical trial. *JAMA*. 2015;313:1240-1248

15. Olin JW, Froehlich J, Gu X, Bacharach JM, Eagle K, Gray BH, et al. The united states registry for fibromuscular dysplasia: Results in the first 447 patients. *Circulation*. 2012;125:3182-3190

16. Hwang J, Kim SJ, Bang OY, Chung CS, Lee KH, Kim DK, et al. Ischemic stroke in takayasu's arteritis: Lesion patterns and possible mechanisms. *J Clin Neurol*. 2012;8:109-115

17. Hajj-Ali RA, Singhal AB, Benseler S, Molloy E, Calabrese LH. Primary angiitis of the cns. *Lancet Neurol*. 2011;10:561-572

18. Scott RM, Smith ER. Moyamoya disease and moyamoya syndrome. *The New England journal of medicine*. 2009;360:1226-1237

19. Kuroda S, Houkin K. Moyamoya disease: Current concepts and future perspectives. *Lancet Neurol*. 2008;7:1056-1066

20. Seol HJ, Wang KC, Kim SK, Hwang YS, Kim KJ, Cho BK. Headache in pediatric moyamoya disease: Review of 204 consecutive cases. *J Neurosurg*. 2005;103:439-442

21. Bersano A, Guey S, Bedini G, Nava S, Herve D, Vajkoczy P, et al. Research progresses in understanding the pathophysiology of moyamoya disease.

Cerebrovasc Dis. 2016;41:105-118

22. Yonekawa Y, Ogata N, Kaku Y, Taub E, Imhof HG. Moyamoya disease in europe, past and present status. *Clin Neurol Neurosurg*. 1997;99 Suppl 2:S58-60

23. Berlit P. Diagnosis and treatment of cerebral vasculitis. *Ther Adv Neurol Disord*. 2010;3:29-42

24. Group EIBS. Failure of extracranial-intracranial arterial bypass to reduce the risk of ischemic stroke. Results of an international randomized trial. *N Engl J Med*. 1985;313:1191-1200

25. Schubert GA, Biermann P, Weiss C, Seiz M, Vajkoczy P, Schmiedek P, et al. Risk profile in extracranial/intracranial bypass surgery--the role of antiplatelet agents, disease pathology, and surgical technique in 168 direct revascularization procedures. *World Neurosurg*. 2014;82:672-677

26. Low SW, Teo K, Lwin S, Yeo LL, Paliwal PR, Ahmad A, et al. Improvement in cerebral hemodynamic parameters and outcomes after superficial temporal artery-middle cerebral artery bypass in patients with severe stenoocclusive disease of the intracranial internal carotid or middle cerebral arteries. *J Neurosurg*. 2015;123:662-669

27. Kim T, Oh CW, Kwon OK, Hwang G, Kim JE, Kang HS, et al. Stroke prevention by direct revascularization for patients with adult-onset moyamoya disease presenting with ischemia. *J Neurosurg*. 2016;124:1788-1793

28. Guzman R, Lee M, Achrol A, Bell-Stephens T, Kelly M, Do HM, et al. Clinical outcome after 450 revascularization procedures for moyamoya disease. Clinical article. *J Neurosurg*. 2009;111:927-935

29. Bao XY, Duan L, Yang WZ, Li DS, Sun WJ, Zhang ZS, et al. Clinical features, surgical treatment, and long-term outcome in pediatric patients with moyamoya disease in china. *Cerebrovasc Dis*. 2015;39:75-81

30. Amin-Hanjani S, Singh A, Rifai H, Thulborn KR, Alaraj A, Aletich V, et al. Combined direct and indirect bypass for moyamoya: Quantitative assessment of direct bypass flow over time. *Neurosurgery*. 2013;73:962-967; discussion 967-968

31. Cho WS, Kim JE, Kim CH, Ban SP, Kang HS, Son YJ, et al. Long-term outcomes after combined revascularization surgery in adult moyamoya disease. *Stroke*.

2014;45:3025-3031

32. Czabanka M, Pena-Tapia P, Scharf J, Schubert GA, Munch E, Horn P, et al. Characterization of direct and indirect cerebral revascularization for the treatment of european patients with moyamoya disease. *Cerebrovasc Dis*. 2011;32:361-369

33. Brown MM, Wade JP, Marshall J. Fundamental importance of arterial oxygen content in the regulation of cerebral blood flow in man. *Brain*. 1985;108 (Pt 1):81-93

34. Gallagher D, Belmonte D, Deurenberg P, Wang Z, Krasnow N, Pi-Sunyer FX, et al. Organ-tissue mass measurement allows modeling of ree and metabolically active tissue mass. *Am J Physiol*. 1998;275:E249-258

35. Bernsmeier A, Gottstein U. [the metabolism of the brain with particular consideration of carbohydrates]. *Acta Neurochir (Wien)*. 1967;16:158-159

36. Hamel E. Perivascular nerves and the regulation of cerebrovascular tone. *J Appl Physiol (1985)*. 2006;100:1059-1064

37. Pierce EC, Jr., Lambertsen CJ, Deutsch S, Chase PE, Linde HW, Dripps RD, et al. Cerebral circulation and metabolism during thiopental anesthesia and hyper-ventilation in man. *J Clin Invest*. 1962;41:1664-1671

38. Kety SS, Schmidt CF. Measurement of cerebral blood flow and cerebral oxygen consumption in man. *Fed Proc*. 1946;5:264

39. Kety SS, Schmidt CF. The effects of altered arterial tensions of carbon dioxide and oxygen on cerebral blood flow and cerebral oxygen consumption of normal young men. *J Clin Invest*. 1948;27:484-492

40. Faraci FM, Heistad DD. Regulation of large cerebral arteries and cerebral microvascular pressure. *Circ Res*. 1990;66:8-17

41. Kulik T, Kusano Y, Aronhime S, Sandler AL, Winn HR. Regulation of cerebral vasculature in normal and ischemic brain. *Neuropharmacology*. 2008;55:281-288

42. Rapela CE, Green HD. Autoregulation of canine cerebral blood flow. *Circ Res*. 1964;15:SUPPL:205-212

43. Hall JE, Guyton AC. *Guyton and hall textbook of medical physiology*. Philadelphia,

PA: Saunders Elsevier; 2011.

44. Eichling JO, Raichle ME, Grubb RL, Jr., Larson KB, Ter-Pogossian MM. In vivo determination of cerebral blood volume with radioactive oxygen-15 in the monkey. *Circ Res*. 1975;37:707-714

45. van Zijl PC, Eleff SM, Ulatowski JA, Oja JM, Ulug AM, Traystman RJ, et al. Quantitative assessment of blood flow, blood volume and blood oxygenation effects in functional magnetic resonance imaging. *Nat Med*. 1998;4:159-167

46. Steiner LA, Andrews PJ. Monitoring the injured brain: Icp and cbf. *Br J Anaesth*. 2006;97:26-38

47. Cipolla MJ, Osol G. Vascular smooth muscle actin cytoskeleton in cerebral artery forced dilatation. *Stroke*. 1998;29:1223-1228

48. De Vis J. Introduction to cerebrovascular reserve & its measurements. *International Society for Magnetic Resonance in Medicine* 2017

49. Powers WJ. Cerebral hemodynamics in ischemic cerebrovascular disease. *Ann Neurol*. 1991;29:231-240

50. Vorstrup S, Lass P, Waldemar G, Brandi L, Schmidt JF, Johnsen A, et al. Increased cerebral blood flow in anemic patients on long-term hemodialytic treatment. *J Cereb Blood Flow Metab*. 1992;12:745-749

51. Prohovnik I, Hurlet-Jensen A, Adams R, De Vivo D, Pavlakis SG. Hemodynamic etiology of elevated flow velocity and stroke in sickle-cell disease. *J Cereb Blood Flow Metab*. 2009;29:803-810

52. Cipolla MJ. *The cerebral circulation*. San Rafael, CA: Morgan & Claypool Life Sciences.; 2009.

53. Reeves A, Swenson R. *Disorders of the nervous system.*: Dartmouth Medical School.; 2008.

54. Lambertsen CJ, Semple SJ, Smyth MG, Gelfand R. H and pco2 as chemical factors in respiratory and cerebral circulatory control. *J Appl Physiol*. 1961;16:473-484

55. Kontos HA, Raper AJ, Patterson JL. Analysis of vasoactivity of local ph, pco2 and bicarbonate on pial vessels. *Stroke*. 1977;8:358-360

56. Yoon S, Zuccarello M, Rapoport RM. Pco(2) and ph regulation of cerebral blood flow. *Front Physiol*. 2012;3:365

57. Juni JE, Waxman AD, Devous MD, Sr., Tikofsky RS, Ichise M, Van Heertum RL, et al. Procedure guideline for brain perfusion spect using (99m)tc radiopharmaceuticals 3.0. *J Nucl Med Technol*. 2009;37:191-195

58. Committee NIIHSGW, Wall M, McDermott MP, Kieburtz KD, Corbett JJ, Feldon SE, et al. Effect of acetazolamide on visual function in patients with idiopathic intracranial hypertension and mild visual loss: The idiopathic intracranial hypertension treatment trial. *JAMA*. 2014;311:1641-1651

59. Ter-Pogossian MM, Herscovitch P. Radioactive oxygen-15 in the study of cerebral blood flow, blood volume, and oxygen metabolism. *Semin Nucl Med*. 1985;15:377-394

60. Martin WR, Powers WJ, Raichle ME. Cerebral blood volume measured with inhaled c15o and positron emission tomography. *J Cereb Blood Flow Metab*. 1987;7:421-426

61. Mintun MA, Raichle ME, Martin WR, Herscovitch P. Brain oxygen utilization measured with o-15 radiotracers and positron emission tomography. *J Nucl Med*. 1984;25:177-187

62. Videen TO, Perlmutter JS, Herscovitch P, Raichle ME. Brain blood volume, flow, and oxygen utilization measured with 15o radiotracers and positron emission tomography: Revised metabolic computations. *J Cereb Blood Flow Metab*. 1987;7:513-516

63. Murphy KJ, Deveikisz JP, Brunberg JA, Jamadar DA, Frey KA. [o-15]h2o positron emission tomography determination of cerebral blood flow reserve after intravenous acetazolamide during balloon test occlusion of the internal carotid artery. *Interv Neuroradiol*. 1998;4:57-62

64. Derdeyn CP, Videen TO, Yundt KD, Fritsch SM, Carpenter DA, Grubb RL, et al. Variability of cerebral blood volume and oxygen extraction: Stages of cerebral haemodynamic impairment revisited. *Brain*. 2002;125:595-607

65. Yamauchi H, Fukuyama H, Nagahama Y, Nabatame H, Nakamura K, Yamamoto Y, et al. Evidence of misery perfusion and risk for recurrent stroke in major cerebral arterial occlusive diseases from pet. *J Neurol Neurosurg Psychiatry*.

1996;61:18-25

66. Derdeyn CP, Yundt KD, Videen TO, Carpenter DA, Grubb RL, Jr., Powers WJ. Increased oxygen extraction fraction is associated with prior ischemic events in patients with carotid occlusion. *Stroke*. 1998;29:754-758

67. Derdeyn CP, Grubb RL, Jr., Powers WJ. Cerebral hemodynamic impairment: Methods of measurement and association with stroke risk. *Neurology*. 1999;53:251-259

68. Grubb RL, Jr., Derdeyn CP, Fritsch SM, Carpenter DA, Yundt KD, Videen TO, et al. Importance of hemodynamic factors in the prognosis of symptomatic carotid occlusion. *JAMA*. 1998;280:1055-1060

69. Baron JC, Bousser MG, Rey A, Guillard A, Comar D, Castaigne P. Reversal of focal "misery-perfusion syndrome" by extra-intracranial arterial bypass in hemodynamic cerebral ischemia. A case study with 15o positron emission tomography. *Stroke*. 1981;12:454-459

70. Grubb RL, Jr., Ratcheson RA, Raichle ME, Kliefoth AB, Gado MH. Regional cerebral blood flow and oxygen utilization in superficial temporal-middle cerebral artery anastomosis patients: An exploratory definition of clinical problems. *J Neurosurg*. 1979;50:733-741

71. Powers WJ, Martin WR, Herscovitch P, Raichle ME, Grubb RL, Jr. Extracranial-intracranial bypass surgery: Hemodynamic and metabolic effects. *Neurology*. 1984;34:1168-1174

72. Carlson AP, Yonas H, Chang YF, Nemoto EM. Failure of cerebral hemodynamic selection in general or of specific positron emission tomography methodology?: Carotid occlusion surgery study (coss). *Stroke*. 2011;42:3637-3639

73. Powers WJ, Clarke WR, Grubb RL, Jr., Videen TO, Adams HP, Jr., Derdeyn CP, et al. Extracranial-intracranial bypass surgery for stroke prevention in hemodynamic cerebral ischemia: The carotid occlusion surgery study randomized trial. *JAMA*. 2011;306:1983-1992

74. Grubb RL, Jr., Raichle ME, Eichling JO, Ter-Pogossian MM. The effects of changes in paco2 on cerebral blood volume, blood flow, and vascular mean transit time. *Stroke*. 1974;5:630-639

75. Grubb RL, Jr., Raichle ME, Higgins CS, Eichling JO. Measurement of regional cerebral blood volume by emission tomography. *Ann Neurol*. 1978;4:322-328

76. Petersen ET, Mouridsen K, Golay X, all named co-authors of the Qt-rs. The quasar reproducibility study, part ii: Results from a multi-center arterial spin labeling test-retest study. *Neuroimage*. 2010;49:104-113

77. van Osch MJ, Teeuwisse WM, van Walderveen MA, Hendrikse J, Kies DA, van Buchem MA. Can arterial spin labeling detect white matter perfusion signal? *Magn Reson Med*. 2009;62:165-173

78. Qin Q, Grgac K, van Zijl PC. Determination of whole-brain oxygen extraction fractions by fast measurement of blood t(2) in the jugular vein. *Magn Reson Med*. 2011;65:471-479

79. Lu H, Xu F, Rodrigue KM, Kennedy KM, Cheng Y, Flicker B, et al. Alterations in cerebral metabolic rate and blood supply across the adult lifespan. *Cereb Cortex*. 2011;21:1426-1434

80. Donahue MJ, Hua J, Pekar JJ, van Zijl PC. Effect of inflow of fresh blood on vascular-space-occupancy (vaso) contrast. *Magn Reson Med*. 2009;61:473-480

81. Powers WJ, Grubb RL, Jr., Darriet D, Raichle ME. Cerebral blood flow and cerebral metabolic rate of oxygen requirements for cerebral function and viability in humans. *J Cereb Blood Flow Metab*. 1985;5:600-608

82. Spano VR, Mandell DM, Poublanc J, Sam K, Battisti-Charbonney A, Pucci O, et al. Co2 blood oxygen level-dependent mr mapping of cerebrovascular reserve in a clinical population: Safety, tolerability, and technical feasibility. *Radiology*. 2013;266:592-598

83. Hua J, Qin Q, Donahue MJ, Zhou J, Pekar JJ, van Zijl PC. Inflow-based vascular-space-occupancy (ivaso) mri. *Magn Reson Med*. 2011;66:40-56

84. Donahue MJ, Dethrage LM, Faraco CC, Jordan LC, Clemmons P, Singer R, et al. Routine clinical evaluation of cerebrovascular reserve capacity using carbogen in patients with intracranial stenosis. *Stroke; a journal of cerebral circulation*. 2014;45:2335-2341

85. Wu WC, Lin SC, Wang DJ, Chen KL, Li YD. Measurement of cerebral white matter perfusion using pseudocontinuous arterial spin labeling 3t magnetic

resonance imaging--an experimental and theoretical investigation of feasibility. *PLoS One*. 2013;8:e82679

86. Zhang K, Herzog H, Mauler J, Filss C, Okell TW, Kops ER, et al. Comparison of cerebral blood flow acquired by simultaneous [15o]water positron emission tomography and arterial spin labeling magnetic resonance imaging. *J Cereb Blood Flow Metab*. 2014;34:1373-1380

87. Alsop DC, Detre JA, Golay X, Gunther M, Hendrikse J, Hernandez-Garcia L, et al. Recommended implementation of arterial spin-labeled perfusion mri for clinical applications: A consensus of the ismrm perfusion study group and the european consortium for asl in dementia. *Magn Reson Med*. 2015;73:spcone

88. Dai W, Garcia D, de Bazelaire C, Alsop DC. Continuous flow-driven inversion for arterial spin labeling using pulsed radio frequency and gradient fields. *Magn Reson Med*. 2008;60:1488-1497

89. Lu H, Clingman C, Golay X, van Zijl PC. Determining the longitudinal relaxation time (t1) of blood at 3.0 tesla. *Magn Reson Med*. 2004;52:679-682

90. Zaharchuk G, Do HM, Marks MP, Rosenberg J, Moseley ME, Steinberg GK. Arterial spin-labeling mri can identify the presence and intensity of collateral perfusion in patients with moyamoya disease. *Stroke*. 2011;42:2485-2491

91. Zhang X, Petersen ET, Ghariq E, De Vis JB, Webb AG, Teeuwisse WM, et al. In vivo blood t(1) measurements at 1.5 t, 3 t, and 7 t. *Magn Reson Med*. 2013;70:1082-1086

92. Alsop DC, Detre JA. Reduced transit-time sensitivity in noninvasive magnetic resonance imaging of human cerebral blood flow. *J Cereb Blood Flow Metab*. 1996;16:1236-1249

93. Herscovitch P, Raichle ME. What is the correct value for the brain--blood partition coefficient for water? *J Cereb Blood Flow Metab*. 1985;5:65-69

94. Juttukonda MR, Jordan LC, Gindville MC, Davis LT, Watchmaker JM, Pruthi S, et al. Cerebral hemodynamics and pseudo-continuous arterial spin labeling considerations in adults with sickle cell anemia. *NMR Biomed*. 2017;30

95. Ogawa S, Lee TM, Kay AR, Tank DW. Brain magnetic resonance imaging with contrast dependent on blood oxygenation. *Proc Natl Acad Sci U S A*. 1990;87:9868-

9872

96. Chen BR, Kozberg MG, Bouchard MB, Shaik MA, Hillman EM. A critical role for the vascular endothelium in functional neurovascular coupling in the brain. *J Am Heart Assoc*. 2014;3:e000787

97. Scholvinck ML, Maier A, Ye FQ, Duyn JH, Leopold DA. Neural basis of global resting-state fmri activity. *Proc Natl Acad Sci U S A*. 2010;107:10238-10243

98. Donahue MJ, Faraco CC, Strother MK, Chappell Ma, Rane S, Dethrage LM, et al. Bolus arrival time and cerebral blood flow responses to hypercarbia. *Journal of cerebral blood flow and metabolism : official journal of the International Society of Cerebral Blood Flow and Metabolism*. 2014;34:1243-1252

99. Donahue MJ, Strother MK, Lindsey KP, Hocke LM, Tong Y, Frederick BD. Time delay processing of hypercapnic fmri allows quantitative parameterization of cerebrovascular reactivity and blood flow delays. *J Cereb Blood Flow Metab*. 2015

100. Tong Y, Bergethon PR, Frederick BD. An improved method for mapping cerebrovascular reserve using concurrent fmri and near-infrared spectroscopy with regressor interpolation at progressive time delays (riptide). *Neuroimage*. 2011;56:2047-2057

101. Donahue MJ, Strother MK, Lindsey KP, Hocke LM, Tong Y, Frederick BD. Time delay processing of hypercapnic fmri allows quantitative parameterization of cerebrovascular reactivity and blood flow delays. *J Cereb Blood Flow Metab*. 2016;36:1767-1779

102. Taylor CL, Selman WR, Ratcheson RA. Steal affecting the central nervous system. *Neurosurgery*. 2002;50:679-688; discussion 688-679

103. Arteaga DF, Strother MK, Faraco CC, Jordan LC, Ladner TR, Dethrage LM, et al. The vascular steal phenomenon is an incomplete contributor to negative cerebrovascular reactivity in patients with symptomatic intracranial stenosis. *Journal of cerebral blood flow and metabolism : official journal of the International Society of Cerebral Blood Flow and Metabolism*. 2014;34:1453-1462

104. Hara S, Tanaka Y, Ueda Y, Hayashi S, Inaji M, Ishiwata K, et al. Noninvasive evaluation of cbf and perfusion delay of moyamoya disease using arterial spin-labeling mri with multiple postlabeling delays: Comparison with 15o-gas pet and dsc-mri. *AJNR Am J Neuroradiol*. 2017;38:696-702

105. Tsujikawa T, Kimura H, Matsuda T, Fujiwara Y, Isozaki M, Kikuta K, et al. Arterial transit time mapping obtained by pulsed continuous 3d asl imaging with multiple post-label delay acquisitions: Comparative study with pet-cbf in patients with chronic occlusive cerebrovascular disease. *PLoS One*. 2016;11:e0156005

106. Wright GA, Hu BS, Macovski A. 1991 i.I. Rabi award. Estimating oxygen saturation of blood in vivo with mr imaging at 1.5 t. *J Magn Reson Imaging*. 1991;1:275-283

107. Thulborn KR, Waterton JC, Matthews PM, Radda GK. Oxygenation dependence of the transverse relaxation time of water protons in whole blood at high field. *Biochim Biophys Acta*. 1982;714:265-270

108. Golay X, Silvennoinen MJ, Zhou J, Clingman CS, Kauppinen RA, Pekar JJ, et al. Measurement of tissue oxygen extraction ratios from venous blood t(2): Increased precision and validation of principle. *Magn Reson Med*. 2001;46:282-291

109. Oja JM, Gillen JS, Kauppinen RA, Kraut M, van Zijl PC. Determination of oxygen extraction ratios by magnetic resonance imaging. *J Cereb Blood Flow Metab*. 1999;19:1289-1295

110. Mintun MA, Lundstrom BN, Snyder AZ, Vlassenko AG, Shulman GL, Raichle ME. Blood flow and oxygen delivery to human brain during functional activity: Theoretical modeling and experimental data. *Proc Natl Acad Sci U S A*. 2001;98:6859-6864

111. Lu H, Ge Y. Quantitative evaluation of oxygenation in venous vessels using t2-relaxation-under-spin-tagging mri. *Magn Reson Med*. 2008;60:357-363

112. Lu H, Xu F, Grgac K, Liu P, Qin Q, van Zijl P. Calibration and validation of trust mri for the estimation of cerebral blood oxygenation. *Magnetic resonance in medicine*. 2012;67:42-49

113. Liu P, Dimitrov I, Andrews T, Crane DE, Dariotis JK, Desmond J, et al. Multisite evaluations of a t2 -relaxation-under-spin-tagging (trust) mri technique to measure brain oxygenation. *Magn Reson Med*. 2016;75:680-687

114. He X, Yablonskiy DA. Quantitative bold: Mapping of human cerebral deoxygenated blood volume and oxygen extraction fraction: Default state. *Magn Reson Med*. 2007;57:115-126

115. Yablonskiy DA, Haacke EM. Theory of nmr signal behavior in magnetically inhomogeneous tissues: The static dephasing regime. *Magn Reson Med*. 1994;32:749-763

116. Bulte DP, Kelly M, Germuska M, Xie J, Chappell MA, Okell TW, et al. Quantitative measurement of cerebral physiology using respiratory-calibrated mri. *Neuroimage*. 2012;60:582-591

117. Germuska M, Bulte DP. Mri measurement of oxygen extraction fraction, mean vessel size and cerebral blood volume using serial hyperoxia and hypercapnia. *Neuroimage*. 2014;92:132-142

118. Donahue MJ, Hoogduin H, van Zijl PC, Jezzard P, Luijten PR, Hendrikse J. Blood oxygenation level-dependent (bold) total and extravascular signal changes and deltar2* in human visual cortex at 1.5, 3.0 and 7.0 t. *NMR Biomed*. 2011;24:25-34

119. Krishnamurthy LC, Mao D, King KS, Lu H. Correction and optimization of a t2-based approach to map blood oxygenation in small cerebral veins. *Magn Reson Med*. 2016;75:1100-1109

120. Bolar DS, Rosen BR, Sorensen AG, Adalsteinsson E. Quantitative imaging of extraction of oxygen and tissue consumption (quixotic) using venular-targeted velocity-selective spin labeling. *Magn Reson Med*. 2011;66:1550-1562

121. Guo J, Wong EC. Venous oxygenation mapping using velocity-selective excitation and arterial nulling. *Magn Reson Med*. 2012;68:1458-1471

122. Kudo K, Liu T, Murakami T, Goodwin J, Uwano I, Yamashita F, et al. Oxygen extraction fraction measurement using quantitative susceptibility mapping: Comparison with positron emission tomography. *J Cereb Blood Flow Metab*. 2016;36:1424-1433

123. Fåhraeus R, Lindqvist T. The viscosity of the blood in narrow capillary tubes. *Am J Physiol*. 1931;93:562–568

124. Zhao JM, Clingman CS, Narvainen MJ, Kauppinen RA, van Zijl PC. Oxygenation and hematocrit dependence of transverse relaxation rates of blood at 3t. *Magn Reson Med*. 2007;58:592-597

125. Fan AP, Blockley NP, Bolar DS, Gauthier CJ, Liu P, Ni WW, et al. Imaging of oxygenation in the brain. *Proc. Intl. Mag. Reson. Med. 24*. 2016

126. Hallemeier CL, Rich KM, Grubb RL, Jr., Chicoine MR, Moran CJ, Cross DT, 3rd, et al. Clinical features and outcome in north american adults with moyamoya phenomenon. *Stroke*. 2006;37:1490-1496

127. Arias EJ, Derdeyn CP, Dacey RG, Jr., Zipfel GJ. Advances and surgical considerations in the treatment of moyamoya disease. *Neurosurgery*. 2014;74 Suppl 1:S116-125

128. Liebeskind DS, Cotsonis GA, Saver JL, Lynn MJ, Turan TN, Cloft HJ, et al. Collaterals dramatically alter stroke risk in intracranial atherosclerosis. *Ann Neurol*. 2011;69:963-974

129. Strother MK, Anderson MD, Singer RJ, Du L, Moore RD, Shyr Y, et al. Cerebrovascular collaterals correlate with disease severity in adult north american patients with moyamoya disease. *AJNR Am J Neuroradiol*. 2014;35:1318-1324

130. Ostergaard L, Smith DF, Vestergaard-Poulsen P, Hansen SB, Gee AD, Gjedde A, et al. Absolute cerebral blood flow and blood volume measured by magnetic resonance imaging bolus tracking: Comparison with positron emission tomography values. *J Cereb Blood Flow Metab*. 1998;18:425-432

131. Donahue MJ, Sideso E, MacIntosh BJ, Kennedy J, Handa A, Jezzard P. Absolute arterial cerebral blood volume quantification using inflow vascular-space-occupancy with dynamic subtraction magnetic resonance imaging. *J Cereb Blood Flow Metab*. 2010;30:1329-1342

132. Leng X, Wong KS, Liebeskind DS. Evaluating intracranial atherosclerosis rather than intracranial stenosis. *Stroke*. 2014;45:645-651

133. Jordan LC, Gindville MC, Scott AO, Juttukonda MR, Strother MK, Kassim AA, et al. Non-invasive imaging of oxygen extraction fraction in adults with sickle cell anaemia. *Brain*. 2016

134. Iwama T, Akiyama Y, Morimoto M, Kojima A, Hayashida K. Comparison of positron emission tomography study results of cerebral hemodynamics in patients with bleeding- and ischemic-type moyamoya disease. *Neurosurg Focus*. 1998;5:e3

135. Zheng G, Wen J, Lu H, Lou Y, Pan Z, Liu W, et al. Elevated global cerebral blood flow, oxygen extraction fraction and unchanged metabolic rate of oxygen in young adults with end-stage renal disease: An mri study. *Eur Radiol*. 2015

136. Sheng M, Lu H, Liu P, Thomas BP, McAdams CJ. Cerebral perfusion differences in women currently with and recovered from anorexia nervosa. *Psychiatry Res*. 2015;232:175-183

137. Liu P, Huang H, Rollins N, Chalak LF, Jeon T, Halovanic C, et al. Quantitative assessment of global cerebral metabolic rate of oxygen (cmro2) in neonates using mri. *NMR Biomed*. 2014;27:332-340

138. Schubert GA, Czabanka M, Seiz M, Horn P, Vajkoczy P, Thome C. Perfusion characteristics of moyamoya disease: An anatomically and clinically oriented analysis and comparison. *Stroke*. 2014;45:101-106

139. Ogasawara K, Ogawa A, Yoshimoto T. Cerebrovascular reactivity to acetazolamide and outcome in patients with symptomatic internal carotid or middle cerebral artery occlusion: A xenon-133 single-photon emission computed tomography study. *Stroke*. 2002;33:1857-1862

140. Ikezaki K, Matsushima T, Kuwabara Y, Suzuki SO, Nomura T, Fukui M. Cerebral circulation and oxygen metabolism in childhood moyamoya disease: A perioperative positron emission tomography study. *J Neurosurg*. 1994;81:843-850

141. Yamauchi H, Okazawa H, Kishibe Y, Sugimoto K, Takahashi M. Oxygen extraction fraction and acetazolamide reactivity in symptomatic carotid artery disease. *J Neurol Neurosurg Psychiatry*. 2004;75:33-37

142. Donahue MJ, Ayad M, Moore R, Van Osch M, Singer R, Clemmons P, et al. Relationships between hypercarbic reactivity, cerebral blood flow, and arterial circulation times in patients with moyamoya disease. *Journal of Magnetic Resonance Imaging*. 2013;38:1129-1139

143. Wu B, Lou X, Wu X, Ma L. Intra- and interscanner reliability and reproducibility of 3d whole-brain pseudo-continuous arterial spin-labeling mr perfusion at 3t. *J Magn Reson Imaging*. 2014;39:402-409

144. Juttukonda MR. Quantitation of arterial spin labeling mri labeling efficiency in high cervical velocity conditions using phase contrast angiography. *2016 IEEE 13th International Symposium on Biomedical Imaging (ISBI)*. 2016:1350-1353

145. Mugikura S, Takahashi S, Higano S, Shirane R, Sakurai Y, Yamada S. Predominant involvement of ipsilateral anterior and posterior circulations in moyamoya disease. *Stroke*. 2002;33:1497-1500

146. Smith SM, Jenkinson M, Woolrich MW, Beckmann CF, Behrens TE, Johansen-Berg H, et al. Advances in functional and structural mr image analysis and implementation as fsl. *Neuroimage*. 2004;23 Suppl 1:S208-219

147. Jenkinson M, Smith S. A global optimisation method for robust affine registration of brain images. *Med Image Anal*. 2001;5:143-156

148. Leenders KL, Perani D, Lammertsma AA, Heather JD, Buckingham P, Healy MJ, et al. Cerebral blood flow, blood volume and oxygen utilization. Normal values and effect of age. *Brain*. 1990;113 (Pt 1):27-47

149. Herold S, Brozovic M, Gibbs J, Lammertsma AA, Leenders KL, Carr D, et al. Measurement of regional cerebral blood flow, blood volume and oxygen metabolism in patients with sickle cell disease using positron emission tomography. *Stroke*. 1986;17:692-698

150. Yun TJ, Paeng JC, Sohn CH, Kim JE, Kang HS, Yoon BW, et al. Monitoring cerebrovascular reactivity through the use of arterial spin labeling in patients with moyamoya disease. *Radiology*. 2016;278:205-213

151. Roach BA, Donahue MJ, Davis LT, Faraco CC, Arteaga D, Chen SC, et al. Interrogating the functional correlates of collateralization in patients with intracranial stenosis using multimodal hemodynamic imaging. *AJNR Am J Neuroradiol*. 2016;37:1132-1138

152. Ni WW, Christen T, Rosenberg J, Zun Z, Moseley ME, Zaharchuk G. Imaging of cerebrovascular reserve and oxygenation in moyamoya disease. *J Cereb Blood Flow Metab*. 2016

153. Heyn C, Poublanc J, Crawley A, Mandell D, Han JS, Tymianski M, et al. Quantification of cerebrovascular reactivity by blood oxygen level-dependent mr imaging and correlation with conventional angiography in patients with moyamoya disease. *AJNR Am J Neuroradiol*. 2010;31:862-867

154. Han JS, Mikulis DJ, Mardimae A, Kassner A, Poublanc J, Crawley AP, et al. Measurement of cerebrovascular reactivity in pediatric patients with cerebral vasculopathy using blood oxygen level-dependent mri. *Stroke*. 2011;42:1261-1269

155. Vaclavu L, Mutsaerts H, Ooij PV, Biemond BJ, Wood JC, Majoie CB, et al. Arterial spin labeling mri evaluation of cerebrovascular reserve with acetazolamide in patients with sickle cell disease. *ISMRM 24th Annual Meeting & Exhibition* 2016

156. Krishnamurthy LC, Liu P, Ge Y, Lu H. Vessel-specific quantification of blood oxygenation with t2-relaxation-under-phase-contrast mri. *Magn Reson Med*. 2014;71:978-989

157. Wise RG, Harris AD, Stone AJ, Murphy K. Measurement of oef and absolute cmro2: Mri-based methods using interleaved and combined hypercapnia and hyperoxia. *Neuroimage*. 2013;83:135-147

158. Agarwalla PK, Stapleton CJ, Phillips MT, Walcott BP, Venteicher AS, Ogilvy CS. Surgical outcomes following encephaloduroarteriosynangiosis in north american adults with moyamoya. *J Neurosurg*. 2014;121:1394-1400

159. Ziyeh S, Rick J, Reinhard M, Hetzel A, Mader I, Speck O. Blood oxygen level-dependent mri of cerebral co2 reactivity in severe carotid stenosis and occlusion. *Stroke*. 2005;36:751-756

160. Griffeth VE, Buxton RB. A theoretical framework for estimating cerebral oxygen metabolism changes using the calibrated-bold method: Modeling the effects of blood volume distribution, hematocrit, oxygen extraction fraction, and tissue signal properties on the bold signal. *Neuroimage*. 2011;58:198-212

161. Fisher JA, Sobczyk O, Crawley A, Poublanc J, Dufort P, Venkatraghavan L, et al. Assessing cerebrovascular reactivity by the pattern of response to progressive hypercapnia. *Hum Brain Mapp*. 2017

162. Liu P, Welch BG, Li Y, Gu H, King D, Yang Y, et al. Multiparametric imaging of brain hemodynamics and function using gas-inhalation mri. *Neuroimage*. 2017;146:715-723

163. Uchino H, Kuroda S, Hirata K, Shiga T, Houkin K, Tamaki N. Predictors and clinical features of postoperative hyperperfusion after surgical revascularization for moyamoya disease: A serial single photon emission ct/positron emission tomography study. *Stroke*. 2012;43:2610-2616

164. Vorstrup S, Brun B, Lassen NA. Evaluation of the cerebral vasodilatory capacity by the acetazolamide test before ec-ic bypass surgery in patients with occlusion of the internal carotid artery. *Stroke*. 1986;17:1291-1298

165. Stokely EM, Sveinsdottir E, Lassen NA, Rommer P. A single photon dynamic computer assisted tomograph (dcat) for imaging brain function in multiple cross sections. *J Comput Assist Tomogr*. 1980;4:230-240

166. Tancredi FB, Lajoie I, Hoge RD. Test-retest reliability of cerebral blood flow and blood oxygenation level-dependent responses to hypercapnia and hyperoxia using dual-echo pseudo-continuous arterial spin labeling and step changes in the fractional composition of inspired gases. *J Magn Reson Imaging*. 2015;42:1144-1157

167. Su P, Mao D, Liu P, Li Y, Pinho MC, Welch BG, et al. Multiparametric estimation of brain hemodynamics with mr fingerprinting asl. *Magn Reson Med*. 2016

168. Federau C, Christensen S, Zun Z, Park SW, Ni W, Moseley M, et al. Cerebral blood flow, transit time, and apparent diffusion coefficient in moyamoya disease before and after acetazolamide. *Neuroradiology*. 2017;59:5-12

169. Roach BA, Donahue MJ, Davis LT, Faraco CC, Arteaga D, Chen SC, et al. Interrogating the functional correlates of collateralization in patients with intracranial stenosis using multimodal hemodynamic imaging. *AJNR Am J Neuroradiol*. 2016

170. Faraco CC, Strother MK, Siero JC, Arteaga DF, Scott AO, Jordan LC, et al. The cumulative influence of hyperoxia and hypercapnia on blood oxygenation and r*(2). *J Cereb Blood Flow Metab*. 2015;35:2032-2042

171. Matsushima T, Fukui M, Kitamura K, Hasuo K, Kuwabara Y, Kurokawa T. Encephalo-duro-arterio-synangiosis in children with moyamoya disease. *Acta Neurochir (Wien)*. 1990;104:96-102

172. Allen LM, Hasso AN, Handwerker J, Farid H. Sequence-specific mr imaging findings that are useful in dating ischemic stroke. *Radiographics*. 2012;32:1285-1297; discussion 1297-1289

173. Han JS, Abou-Hamden A, Mandell DM, Poublanc J, Crawley AP, Fisher JA, et al. Impact of extracranial-intracranial bypass on cerebrovascular reactivity and clinical outcome in patients with symptomatic moyamoya vasculopathy. *Stroke*. 2011;42:3047-3054

174. Mandell DM, Han JS, Poublanc J, Crawley AP, Fierstra J, Tymianski M, et al. Quantitative measurement of cerebrovascular reactivity by blood oxygen level-dependent mr imaging in patients with intracranial stenosis: Preoperative cerebrovascular reactivity predicts the effect of extracranial-intracranial bypass surgery. *AJNR Am J Neuroradiol*. 2011;32:721-727

175. Fushimi Y, Okada T, Takagi Y, Funaki T, Takahashi JC, Miyamoto S, et al. Voxel based analysis of surgical revascularization for moyamoya disease: Pre- and postoperative spect studies. *PLoS One*. 2016;11:e0148925

176. Cogswell PM, Davis TL, Strother MK, Faraco CC, Scott AO, Jordan LC, et al. Impact of vessel wall lesions and vascular stenoses on cerebrovascular reactivity in patients with intracranial stenotic disease. *J Magn Reson Imaging*. 2017

177. Mukawa M, Nariai T, Inaji M, Tamada N, Maehara T, Matsushima Y, et al. First autopsy analysis of a neovascularized arterial network induced by indirect bypass surgery for moyamoya disease: Case report. *J Neurosurg*. 2016;124:1211-1214

178. Desai AA, Strother MK, Faraco CC, Morgan VL, Ladner TR, Dethrage LM, et al. The contribution of common surgically implanted hardware to functional mr imaging artifacts. *AJNR Am J Neuroradiol*. 2015;36:2068-2073

179. Donahue MJ, Lu H, Jones CK, Edden RA, Pekar JJ, van Zijl PC. Theoretical and experimental investigation of the vaso contrast mechanism. *Magn Reson Med*. 2006;56:1261-1273

180. Sugino T, Mikami T, Miyata K, Suzuki K, Houkin K, Mikuni N. Arterial spin-labeling magnetic resonance imaging after revascularization of moyamoya disease. *J Stroke Cerebrovasc Dis*. 2013;22:811-816

181. Cockburn DM, Douglas IS. Herpes zoster opthalmicus. *Clin Exp Optom*. 2000;83:59-64

182. Hilt DC, Buchholz D, Krumholz A, Weiss H, Wolinsky JS. Herpes zoster ophthalmicus and delayed contralateral hemiparesis caused by cerebral angiitis: Diagnosis and management approaches. *Ann Neurol*. 1983;14:543-553

183. Ueno M, Oka A, Koeda T, Okamoto R, Takeshita K. Unilateral occlusion of the middle cerebral artery after varicella-zoster virus infection. *Brain Dev*. 2002;24:106-108

184. Bourdette DN, Rosenberg NL, Yatsu FM. Herpes zoster ophthalmicus and delayed ipsilateral cerebral infarction. *Neurology*. 1983;33:1428-1432

185. Nagel MA, Jones D, Wyborny A. Varicella zoster virus vasculopathy: The expanding clinical spectrum and pathogenesis. *J Neuroimmunol*. 2017;308:112-117

186. Arias EJ, Derdeyn CP, Dacey RG, Zipfel GJ. Advances and surgical considerations in the treatment of moyamoya disease. *Neurosurgery*. 2014;74:S116-S125

187. Watchmaker JM, Juttukonda MR, Davis LT, Scott AO, Faraco CC, Gindville MC, et al. Hemodynamic mechanisms underlying elevated oxygen extraction fraction (oef) in moyamoya and sickle cell anemia patients. *J Cereb Blood Flow Metab*. 2016:271678X16682509

188. Swartz RH, Bhuta SS, Farb RI, Agid R, Willinsky RA, Terbrugge KG, et al. Intracranial arterial wall imaging using high-resolution 3-tesla contrast-enhanced mri. *Neurology*. 2009;72:627-634

189. Mossa-Basha M, de Havenon A, Becker KJ, Hallam DK, Levitt MR, Cohen WA, et al. Added value of vessel wall magnetic resonance imaging in the differentiation of moyamoya vasculopathies in a non-asian cohort. *Stroke*. 2016;47:1782-1788

190. Cheng-Ching E, Jones S, Hui FK, Man S, Gilden D, Bhimraj A, et al. High-resolution mri vessel wall imaging in varicella zoster virus vasculopathy. *J Neurol Sci*. 2015;351:168-173

191. Golay X, Stuber M, Pruessmann KP, Meier D, Boesiger P. Transfer insensitive labeling technique (tilt): Application to multislice functional perfusion imaging. *J Magn Reson Imaging*. 1999;9:454-461

192. Petersen ET, Lim T, Golay X. Model-free arterial spin labeling quantification approach for perfusion mri. *Magn Reson Med*. 2006;55:219-232

193. Donahue MJ, Blicher JU, Ostergaard L, Feinberg DA, MacIntosh BJ, Miller KL, et al. Cerebral blood flow, blood volume, and oxygen metabolism dynamics in human visual and motor cortex as measured by whole-brain multi-modal magnetic resonance imaging. *J Cereb Blood Flow Metab*. 2009;29:1856-1866

194. Yablonskiy DA. Quantitation of intrinsic magnetic susceptibility-related effects in a tissue matrix. Phantom study. *Magn Reson Med*. 1998;39:417-428

195. Davis TL, Kwong KK, Weisskoff RM, Rosen BR. Calibrated functional mri: Mapping the dynamics of oxidative metabolism. *Proc Natl Acad Sci U S A*. 1998;95:1834-1839

196. Buxton RB, Wong EC, Frank LR. Dynamics of blood flow and oxygenation changes during brain activation: The balloon model. *Magn Reson Med*.

1998;39:855-864

197. Bulte DP, Drescher K, Jezzard P. Comparison of hypercapnia-based calibration techniques for measurement of cerebral oxygen metabolism with mri. *Magn Reson Med*. 2009;61:391-398

198. Liu Z, Li Y. Cortical cerebral blood flow, oxygen extraction fraction, and metabolic rate in patients with middle cerebral artery stenosis or acute stroke. *AJNR Am J Neuroradiol*. 2016;37:607-614

199. Langham MC, Magland JF, Epstein CL, Floyd TF, Wehrli FW. Accuracy and precision of mr blood oximetry based on the long paramagnetic cylinder approximation of large vessels. *Magn Reson Med*. 2009;62:333-340

200. Garwood M, DelaBarre L. The return of the frequency sweep: Designing adiabatic pulses for contemporary nmr. *J Magn Reson*. 2001;153:155-177

201. Derdeyn CP, Chimowitz MI, Lynn MJ, Fiorella D, Turan TN, Janis LS, et al. Aggressive medical treatment with or without stenting in high-risk patients with intracranial artery stenosis (sammpris): The final results of a randomised trial. *Lancet*. 2014;383:333-341

202. Leigh R, Knutsson L, Zhou J, van Zijl PC. Imaging the physiological evolution of the ischemic penumbra in acute ischemic stroke. *J Cereb Blood Flow Metab*. 2017:271678X17700913